Université Catholique de Louvain
Faculty of Medicine

Contribution of multidetector computed tomography in the detection of collapse of the osteonecrotic femoral head

Charbel Mourad, MD

A dissertation for the degree of Doctor of Philosophy (PhD) in Medical Sciences

October 2021

Promotors:
Prof. Bruno Vande Berg
Prof. Valérie Gangjj

Members of the committee:
Prof. Frédéric Lecouvet (President)
Prof. Christine Galant
Prof. Xavier Banse
Prof. Catherine Behets Wydemans
Prof. Greet Kerckhofs

External members:
Prof. Jean-François Budzik
Prof. Pedro Gondim Teixeira

In dedication to the memory of my late uncle, Jean, who ignited an everlasting flame and instilled the love of learning into my soul

Table of Contents

1 Acknowledgements

First and foremost, I would like to express my extreme gratitude to my promotor, Prof. Bruno Vande Berg for the immense support and patience during this research project. I could not have imagined going through this journey without such an amazing mentor: insanely capable, yet completely humble. Your passion for education, kindness and commitment helped me overcome all the obstacles. Your insightful feedback pushed me to sharpen my thinking, your astute criticism brought my work to a higher level. I cannot thank you enough.

I am also grateful to my co-promotor, Prof. Valérie Gangji for her invaluable insights, to all the committee members: Profs. Frédéric Lecouvet, Christine Galant, Catherine Behets, Xavier Banse and Greet Kerckhofs, for their constructive feedback that helped me guide my research in a good direction, to the external members, Profs. Jean François Budzik and Pedro Gondim Teixeira for their valuable remarks and challenging questions.

My research would have been impossible without the support of the staff members of the radiology and pathology departments at Cliniques Universitaires Saint Luc. My sincere thanks to my colleagues Florent, Thomas, Vicky, Souad, and to our constant source of inspiration, Prof Jacques Malghem. Special thanks to Marin, whose skilled brush added valuable artistic savor to my writings.

I am profoundly grateful to Prof. Christine Galant, Dr. Pierrette Michel, Dr. Emilie Wacheul and Ms Patricia Destrument who gave me invaluable help in histology, to Prof. Greet kerckhofs for her insightful suggestions to exploit µCT data, to Kjell Laperre and Phil Salmon who provided me helpful contributions.

I would also like to thank Nicolas for his valuable expertise in statistical analysis, Anthony for his talent in programming, Christine and Perrine for their continuous assistance and patience that cannot be underestimated.

I would like to thank Anis with whom I am privileged to work, and all my colleagues at Lebanese Hospital-Geitaoui for their continuous support.

Special thanks to Fabiola, for your unwavering support and belief in me. I would also like to thank my friends Pamela, Sammy, and Grace: you have been very supportive and encouraging throughout this research process

I am extremely grateful to my parents, Jamil and Ado, to my sister Jeanne D'arc and to my brothers, Jean, Jamil, Youssef and Toufic, for their constant love, encouragement, moral support and blessings. You are always there for me!

2 List of publications

- **Fused micro-computed tomography (µCT) and histological images of bone specimens**. Mourad C, Laperre K, Halut M, Galant C, Van Cauter M, Vande Berg BC. Diagn Interv Imaging. 2018 Jul-Aug;99(7-8):501-505. Doi: 10.1016/j.diii.2018.01.011.
- **Topology of microfractures in osteonecrotic femoral heads at µCT and histology**. Mourad C, Galant C, Wacheul E, Kirchgesner T, Michoux N, Vande Berg B. Bone. 2020 Dec;141:115623. Doi:10.1016/j.bone.2020.115623.

Submitted papers:

- Collapse-related bone changes in osteonecrotic femoral heads at MDCT: comparison between femoral heads with limited and advanced collapse.
- Collapse-related bone changes at MDCT in ARCO 1-2 osteonecrotic femoral heads: correlation with clinical and MRI data.

3 Abbreviations

(in alphabetical order)

ARCO: Association Research Circulation Osseous
BME: Bone Marrow Edema
BMI: Body Mass Index
CR: Conventional Radiography
CRBC: Collapse-related bone changes
FH: Femoral Head
FHON: Femoral Head Osteonecrosis
JIC: Japanese Investigation Committee
MDCT: Multidetector Computed Tomography
MRI: Magnetic Resonance Imaging
MSK: Musculoskeletal
OA: Osteoarthritis
ON: Osteonecrosis
ONFH: Osteonecrotic Femoral Head
PD Fat Sat: Proton Density with fat suppression
THR: Total Hip Replacement
µCT: Microcomputed Tomography

4 Lexicon

- ***Osteonecrosis:*** a condition in which a circumscribed area of mineralized bone and bone marrow becomes necrotic as a result of the loss of its blood supply. In this manuscript, the term osteonecrosis will be used, and older terminology as “avascular necrosis, aseptic necrosis, ischemic necrosis” will be avoided.

- ***Infarct:*** traditionally refers to metaphyseal or diaphyseal necrotic lesions. Only epiphyseal lesions will be considered in this manuscript and the term infarct will not be used.

- ***Systemic osteonecrosis:*** This term is chosen to stress the fact that a systemic marrow disease is at the origin of bone marrow necrosis.

- ***Spontaneous osteonecrosis:*** a term introduced by Ahlbäck in 1968 (1) to indicate the occurrence of a spontaneous collapse of a weight-bearing epiphysis that was not associated with other necrotic bone lesions. Nowadays, it is accepted that spontaneous osteonecrosis is a complication of a subchondral insufficiency fracture and will not be addressed in this manuscript.

- ***Post-traumatic osteonecrosis*** refers to isolated necrotic lesions that result from vascular damage associated with high-energy trauma (fracture of femoral neck or dislocation). It will not be considered in this manuscript.

- ***Fracture:*** refers to the interruption of the cortical and/or trabecular bone, with or without displacement. In this monograph, we will emphasize on non-traumatic epiphyseal fractures of the femoral head.

- ***Bone marrow edema (BME):*** a generic term used by radiologists to indicate ill-delineated bone marrow lesion with increased signal intensity on water sensitive sequences and mild decreased signal intensity on T1 weighted images (2-4). The occurrence of BME in femoral head osteonecrosis and its significance will not be addressed in this manuscript.

- ***µCT***: refers to a high-resolution research tool used to scan small animals, minerals, and pieces of resected human specimen *ex vivo*. It can achieve isotropic voxel size <1μm. In our study, we used µCT to image femoral head specimens at 12 μm and 50 μm (Table 1).

- ***MDCT (multidetector computed tomography):*** refers to the newer generation of CT that is commonly used in clinical practice to image patients but could also be used in clinical research. In a part of our study, we used an optimized MDCT protocol to scan resected femoral head specimens *in vitro*, achieving a pixel size of ~200 μm. *In vivo*, the usual spatial resolution ranges from 0.5 to 0.625 mm in the z-axis and approximately 0.5 mm in the x- to y-axes (5) (Table 1).

Table 1: Spatial resolution of the different CT techniques used in this research project

Technique	Used in	Voxel size
µCT	Step 1-2	12 µm, isotropic
µCT	Step 3	50 µm, isotropic
In vitro MDCT	Step 3-4	~200 x 200 x 400 µm
In vivo MDCT	Step 5	500 x 500 x 625 µm

5 Abstract

The prognosis and management of femoral head osteonecrosis (FHON), usually assessed by MRI and radiographs, are largely determined by the presence of epiphyseal collapse. Multi-detector CT (MDCT) can also be used for preoperative planning because it can detect bone fracture. There is still much to know about the pathophysiology of collapse and associated bone changes. In this doctoral research project, we addressed the role of MDCT in the detection of collapse-related bone changes (CRBC): cortical and trabecular bone interruption, trabecular bone resorption, and sclerosis.

First, we developed a landmark-based method to match histological and µCT images of specimens with FHON.

Second, matched µCT and histological images were analyzed by a radiologist and histopathologist to detect microfractures using a grid overlay method. The topology of grid boxes with microfractures was assessed in different zones of the necrotic lesion and 2D connectivity parameters were computed. We demonstrated that cortical and trabecular microfractures largely predominated in the necrotic lesion. Trabecular microfractures formed elongated clusters and predominated in the superficial layer of the femoral head.

Third, matched MDCT and µCT images of 8 osteonecrotic femoral head (ONFH) specimens were analyzed using the grid overlay method by two radiologists. MDCT was found to have a moderate sensitivity but a high specificity to detect CRBC in comparison to µCT.

Fourth, MDCT reformats of 14 ONFH specimens were analyzed by two radiologists. The frequency of segments with cortical interruption and trabecular resorption, but not trabecular interruption, was higher in ONFH with advanced than with limited collapse. CRBC predominated in the necrotic lesion and were more frequent in the anterior, central, and superior quadrants of the femoral head.

Fifth, MDCT images of 77 patients with 132 ONFH were analyzed by two radiology residents to detect CRBC. We showed that 98-100% of collapsed and 26-40% of non-collapsed ONFH presented ≥1 CRBC at MDCT. In the group of non-collapsed (ARCO 1-2) ONFH, there was no significant difference in pain, functional impairment, size of the lesion, or frequency of marrow edema on MRI between ONFH with or without CRBC at MDCT.

In conclusion, CRBC at MDCT are frequently detected in non-collapsed ONFH. Further studies are needed to determine their prognostic significance.

6 Introduction

In the late 18th century, James Russell published an essay on bone necrosis which was one of the first detailed pathological descriptions of this condition (Figure 1) (6). At that time, a clear distinction between septic and aseptic necrosis was not made and the majority of the cases that were reported in the following years are thought to have been septic (6, 7).

It is until the early 20th century that Phemister and his associates wrote a series of articles on the etiology and pathogenesis of aseptic necrosis (8, 9). Since then, the number of reported cases started to rise due to increased awareness and diagnosis of this condition, but also to an actual increase in the incidence of osteonecrosis (ON) due in large part to the use of corticosteroids (7). In the second half of the 20th century, two French orthopedic surgeons, Ficat and Arlet noticed that patients' symptoms and prognosis improved after performing functional investigation of bone, which has led to "core decompression" as the cornerstone of treatment of femoral head osteonecrosis (10, 11). During the same period, the histopathology of osteonecrosis and the pathophysiology of bone collapse were thoroughly investigated by Catto (12, 13), Glimcher and Kenzora (14-17) using animal models and resected osteonecrotic femoral head (ONFH) specimens.

In the late eighties, noninvasive detection of pre-radiographic ONFH became feasible due to the advent of MRI (18, 19) that rapidly emerged as the gold standard for the detection and characterization of femoral head osteonecrosis (FHON), largely replacing bone scintigraphy and the functional investigation of bone, a more invasive technique. In the nineties, it appeared that some spontaneous epiphyseal lesions showing bone marrow edema (BME) that were considered initially to represent osteonecrosis, actually represented insufficiency fractures, a condition that had not been clearly defined yet (2, 20, 21).

The importance of FHON, the increased number of reported cases, and the many questions surrounding this condition that remained unanswered, have led to several conferences and symposia on this topic during the second half of the 20th century. The first international symposium on bone circulation was organized by Professors Ficat and Arlet and was held in Toulouse, France, in 1973. Several surgeons and researchers involved in the study of bone circulation took part. This symposium was followed by many others, until 1989, when many international researchers founded the *Association Internationale de Recherche sur la Circulation Osseuse* (Association Research Circulation Osseous, ARCO).

Following this European initiative, several staging systems were developed in North America (22, 23) and Asia (24, 25). In Japan, under the auspices of the Ministry of Health and Welfare, the Japanese Investigation Committee for Intractable Disease (JIC) established a section on avascular necrosis of the femoral head and developed a staging system that also included morphological information to enable to assess the risk for fracture in non-collapsed femoral head lesions (26).

Despite all the achievements and contribution of MRI in the early detection and in-depth knowledge of its natural history, osteonecrosis of the femoral head remains the leading cause of total hip replacement (THR) in the young adult population, and yet, there is still much to be unveiled in the realm of FH collapse.

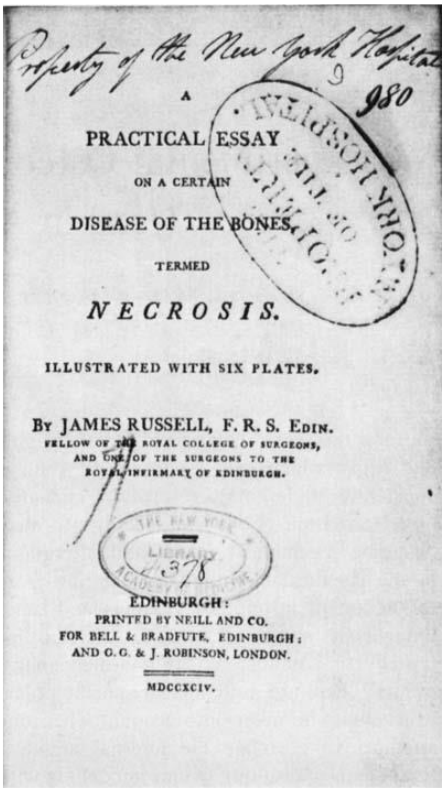

Figure 1: Original title page from Russel's article in 1794 (6)

6.1 Etiology of osteonecrosis

Non-traumatic FHON is frequently idiopathic but many factors were found to be associated with an increased risk to develop this pathology (Table 2) (27). Alcohol overconsumption and steroids are the two most common associated factors in FHON. A Japanese survey of non-traumatic FHON estimated that 34.7% were due to corticosteroid use, 21.8% to alcohol abuse, and 37.1% to idiopathic mechanisms (28).

For many decades, the association of osteonecrosis with genetic traits has been investigated. FHON may be a polygenic disease, and it is speculated that genetic factors might be involved in its occurrence (29). The earliest association was between sickle cell disorders and ON followed by determining the role of hyperlipidemias and various coagulation abnormalities in the predisposition to ON. More recently, other genetic traits have been linked to ON. For example, a decrease in vascular endothelial growth factor activity increases the risk of FHON in patients with steroid induced ON (27), whereas a decreased production of nitric oxide could affect angiogenesis, thrombus formation, and bone turnover (26). Other etiologic factors include cryofibrinogen and P-glycoprotein (29).

Table 2: Factors associated with osteonecrosis.

- Fracture and joint dislocation
- Systemic corticosteroid use
- Cushing's disease
- Alcohol overconsumption
- Sickle cell disease and other hemoglobinopathies
- Renal transplantation and osteodystrophy
- Radiation therapy
- Pancreatitis
- Gout
- Gaucher's disease
- Vasculitis
- Connective tissue diseases (e.g., systemic lupus erythematosus)
- Caisson disease
- Acquired immunodeficiency syndrome (AIDS)
- Severe acute respiratory syndrome (SARS)
- Cytotoxic agents (e.g., vinblastine, vincristine, cisplatin, cyclophosphamide, methotrexate, bleomycin, 5-fluorouracil…)

6.2 Prevalence and epidemiology of osteonecrosis

The exact prevalence of FHON is unknown, partly because many lesions remain clinically silent. In the United States, there are 10000 to 20000 new cases reported each year (30, 31). A Japanese survey estimated that 2500 to 3300 cases occur each year and the annual incidence rate is 1.91/100,000 (28, 30, 31). A Korean survey estimated the annual incidence to be around 29/100,000 (32) and a Chinese survey estimated the prevalence of FHON as about 0.725% (33).

FHON has been reported to account for about 50% of the total hip arthroplasties (THAs) performed in Asia and sub-Saharan Africa (34-36) and over 10% of those in the United States (37). It has been recognized that the prevalence of ON in populations in China, Korea, and Taiwan has been considerably higher than in other areas of the world. The reason for this is not entirely clear, but it may be related to several genetic factors which have recently been identified (38-41).

Idiopathic FHON is more common in men, with an overall male-to-female ratio ranging from 4 to 8:1. It most often develops between the fourth and sixth decades and, on average, it presents almost 10 years later in women than in men. The disorder is bilateral in 40% to 80% of cases. Presentation of symptoms may be asynchronous (42). Age at onset of epiphyseal ON, male-to-female ratio, and bilaterality may also be influenced by the associated causes.

FHON is more and more detected at a pre-clinical stage. One common scenario is the fortuitous discovery of ON in the contralateral side of patients referred to MRI for assessing a painful unilateral hip, leading to the concept of “silent hip”(43). Many studies used MRI to screen the patient population at risk for ON demonstrated the high prevalence of asymptomatic osteonecrosis in the FH but also in the entire body, illustrating the systemic nature of this disorder.

6.3 Pathophysiology of osteonecrosis

Decreased perfusion, vascular stasis, and impaired exchange within the femoral head seem to have a causative effect on the developing bone and marrow ON (44, 45). The *primum movens* seems to be ischemia of the bone marrow given the preserved characteristics of trabecular bone at the molecular scale within the necrotic territory (15, 46, 47). Several mechanisms can contribute to impaired perfusion:

a) mechanical interruption of arteries in cases of displaced femoral neck fracture or hip dislocation (48, 49).
b) Vascular occlusion including thrombotic or embolic occlusion of blood vessels (e.g., fat embolism, sickle cell crisis, caisson disease) (50, 51)
c) injury to the vessel wall (e.g., vasculitis, connective tissue diseases such as systemic lupus erythematosus, radiation, infection)
d) increased intraosseous pressure on the vessel wall (e.g., extravasated blood in marrow, inflammation caused by lipid accumulation in osteocytes, intraosseous hypertension from proliferating Gaucher cells in Gaucher's disease) (37)
e) Increased joint pressure associated with acute arthritis or hemorrhage, with subsequent collapse of peri-osseous intraarticular veins and engorgement of medullary vessels (joint tamponade) (48, 52-58). (Figure 2)

Other theories tried to explain the pathophysiology of ON including direct cellular toxicity, altered mesenchymal stem cell differentiation, increased marrow adiposity, or dysfunctional lipid metabolism (lipotoxicity) (37, 59-62). Although recent studies using Fat Fraction MRI have challenged the concept of increased marrow adiposity (44)

The term "systemic osteonecrosis" is chosen to stress the fact that a systemic marrow disease is at the origin of bone marrow necrosis. Despite all the advancements in knowledge of the pathophysiology of systemic osteonecrosis, there is still much to be learned.

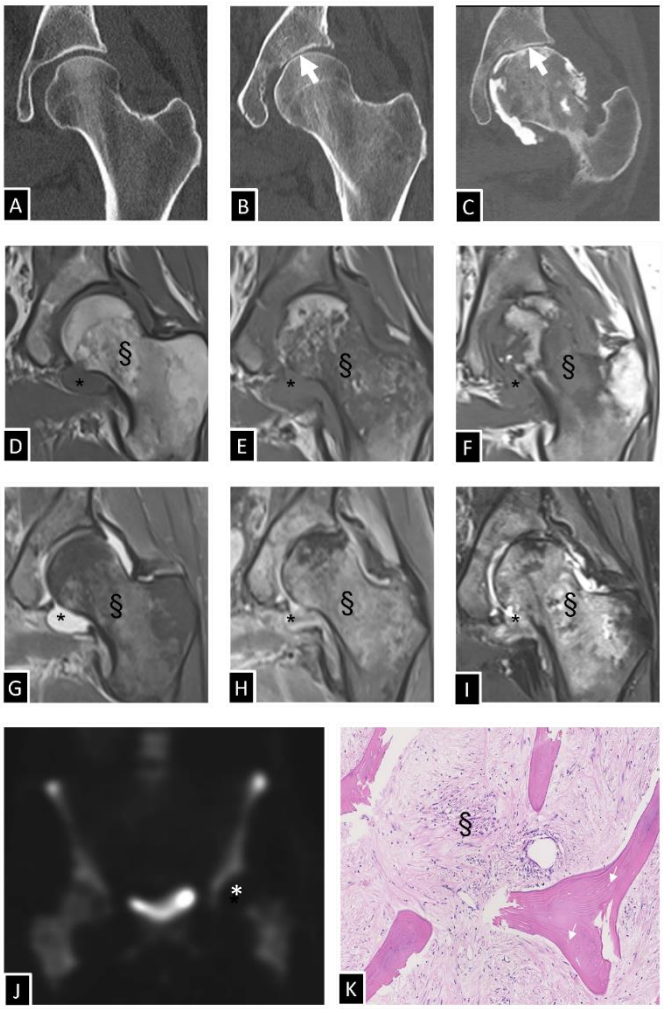

Figure 2: Osteonecrosis of the left femoral head related to septic arthritis in a 44 yo woman, detected on bone scan but was occult on MRI: (A) coronal MDCT reformat, (D) coronal T1 weighted image, and (G) coronal fat-suppressed T2 weighted image at initial presentation showing joint effusion/synovitis (asterisk) and bone marrow edema (BME) (§) of the femoral neck. There was no sign of osteonecrosis. Aspiration and culture yielded Methicillin sensitive Staphylococcus aureus. (J) bone scan 4 days later showed hypo fixation of the left femoral head (asterisk) indicative of osteonecrosis that was occult on MRI. (B) coronal MDCT reformat, (E) coronal T1 weighted image and (H) coronal fat-suppressed T2 weighted image 6 weeks later show joint space narrowing (arrow), joint effusion/synovitis (asterisk) and increase in bone marrow edema (BME) (§) of the proximal femur sparing the superolateral-epiphysis, a territory corresponding to osteonecrosis. (C) coronal reformat of CT-arthrogram, (F) coronal T1 weighted image and (I) coronal fat-suppressed T2 weighted image 4 months after the initial examination show joint space narrowing (arrow), joint effusion/synovitis (asterisk), erosions, and increase in bone marrow edema (BME) (§) of the proximal femur still sparing the superolateral-epiphysis, a territory corresponding to osteonecrosis. (K) Hematoxylin and eosin-stained histological section of the resected femoral head shows features of osteonecrosis: empty osteocyte lacunae (arrows) and reactive fibrovascular tissue involving the bone marrow (§).

6.4 Histopathology of osteonecrosis

At the microscopic level, *cell necrosis* may take several patterns, but coagulation necrosis is the most common pattern of necrosis in bones. It results in complete absence of osteocytes within the bone trabeculae, loss of adipocyte nuclei with lipid cysts formation, and death of hematopoietic cells (13, 15). The reactive interface of fibrovascular tissue that progressively appears and surrounds the ischemic lesion is the hallmark of the disease; it has a concave orientation towards the articular surface and surrounds the necrotic territory. Therefore, the osteonecrotic lesion demonstrates zonal anatomy (63) (Figure 15). The core of the lesion consists of necrotic trabeculae with absent nuclei and saponified or mummified bone marrow necrosis. The reactive interface consists of a layer of fibrovascular connective tissue with trabecular bone resorption or sclerosis surrounding the necrotic tissue. The lesion is surrounded by a viable bone and bone marrow showing reactive hyperemia. The remaining of the femoral head consists of normal bone and marrow located at distance from the ON lesion although recent studies have shown that changes can also occur at distance from the lesion, and that perfusion of the femoral head outside the necrotic lesion may be altered, a phenomenon that might be described as “regional ischemic penumbra” similar to what could be observed in ischemic stroke (44).

6.5 Diagnosis of osteonecrosis

The alert clinician may suspect the diagnosis when facing a patient with acute and spontaneous articular pain and risk factors for FHON. Clinical examination has little diagnostic value except for accurate localization of the involved area (knee pain due to FHON). Blood tests generally do not contribute to the diagnosis of the ON, but they are of importance in the recognition of an eventual underlying disease (e.g., anemia, hyperuricemia, alcohol abuse).

The diagnosis of FHON heavily relies on medical imaging with a predominant role of MRI. Radiographs are relatively insensitive for the detection of the very early stage of the disease. Osteonecrotic lesions become visible because of progressive sclerosis at their margins. In the early 1980s, single-slice computed tomography (CT) was used to asses FHON, however, it soon fell in favor of MRI (19). The new generation of multidetector computed tomography (MDCT) has not been widely investigated for the assessment of FHON. Bone scintigraphy can also be used for the detection of ON before it appears on the radiographs (19, 64-67). In the era of modern imaging, the role of core biopsy for the diagnosis of ON has become obsolete.

6.6 Diagnostic imaging features of osteonecrosis

6.6.1 Radiographs

On conventional radiographs, the diagnosis of FHON is based on the following signs (Figure 3):

(a) Abnormal bone structure of the femoral head with areas of bone sclerosis and cystic resorption. A well-delineated wedge-shaped subchondral lesion surrounded by a rim of sclerosis can be seen (24, 68).

(b) Trabecular bone fractures occasionally visible as a subchondral lucency (the crescent sign).

(c) Abnormal epiphyseal contour associated with bone changes.

(d) Normal joint space width in non-collapsed lesions and early stages of collapse.

The radiographic hallmark of early non-collapsed epiphyseal ON is the presence of a well-delineated area of sclerosis in the subchondral area of the femoral head with a preserved joint space width. The radiographic hallmark of collapsed epiphyseal osteonecrosis is the presence of a fracture that involves the subchondral bone plate and/or the trabecular bone. Subchondral bone plate fracture appears as an abrupt depression of the epiphyseal contour or as a global flattening of the articular surface (Figure 3). Trabecular bone fracture appears as a crescentic radiolucent line parallel to the subchondral bone plate (crescent sign or egg-shell fracture). These two lesion patterns exclusively develop in the necrotic area and may coexist, although in different areas, probably owing to joint biomechanics. Their visibility may also depend on joint positioning during radiograph as collapse is seen in compressed areas and subchondral cleft fracture becomes visible when distraction is applied to the articular surface.

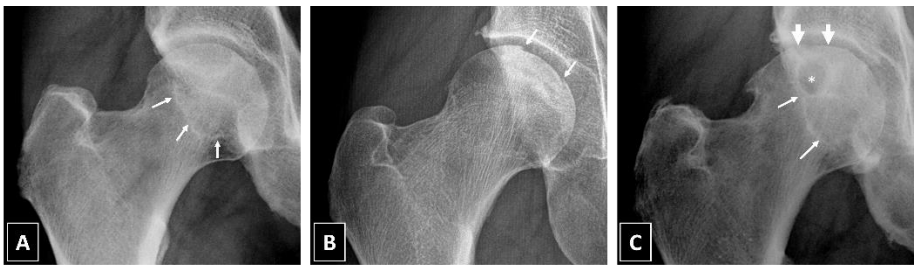

Figure 3: (A) Anteroposterior (AP) radiograph in a non-collapsed ONFH shows a well-delineated subchondral lesion surrounded by a rim of sclerosis (arrows). (B) AP radiograph in an early collapsed ONFH shows focal deformity of the subchondral bone plate (arrows). (C) AP radiograph in a collapsed ONFH shows a global flattening of the articular surface (arrowheads), a rim of sclerosis (arrows), and cystic resorption (asterisk).

Radiographs are insensitive to the detection of early FHON because dead bone remains normal on radiographs. In fact, the reactive interface that surrounds the necrotic territory cannot be detected on radiographs and MDCT until it becomes calcified. With the progression of the disease, radiographs accurately depict the abnormal epiphyseal shape and the altered bone structure (mixed bone sclerosis and resorption) of the involved epiphysis.

The sensitivity and specificity of conventional radiographs for the detection of collapsed ONFH are in the range of 76–89% and 77–97%, respectively, and depend on the reader's experience (69). For pre-collapse FHON, the sensitivity and specificity are in the range of 52–71% and 78–97%, respectively (69-71). Due to the projective nature of radiographic images, the sclerotic reactive margin may not be clearly recognized, and the specificity of radiographs can be limited.

6.6.2 Magnetic Resonance Imaging

The MR appearance of early non-collapsed FHON is (Figure 4):

(a) on T1-weighted images, an area of normal fatty signal intensity delineated by a rim of low signal intensity (18).
(b) on T2-weighted spin-echo images, the peripheral rim may show the double-line sign with an outer low and inner high signal intensity line, in 65% to 85% of ischemic lesions (18). This double-line pattern probably results from a chemical-shift misregistration artifact, related to the fact that there is fat on both sides of a water-like equivalent component (the interface) (20).

At the early stage, the signal of an ischemic yellow marrow lesion remains normal on T1- and T2-weighted spin-echo images but can be altered on fat-saturated images. Occasionally, the signal of necrotic marrow is heterogeneous with fat-like, fibrous-like, and fluid-like components at MR imaging (18) (Figure 4). MR imaging is very sensitive to the detection of early infarcts because it rapidly detects the marrow changes that surround the necrotic lesion, the so-called reactive interface, well before it calcifies. However, it has been shown that ON can be present at histology without overt MRI changes (72, 73). There are also cases where MRI is less sensitive than single-photon emission computed tomography (SPECT) in the very early phases of the disease (74) (Figure 2). Usually, the adjacent marrow shows normal signal intensity and the transition zone between the lesion and the adjacent marrow is narrow. Occasionally, the reactive interface can be blurred because of adjacent changes on its two sides.

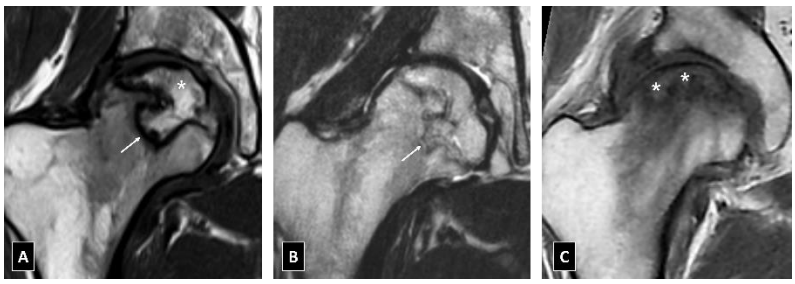

Figure 4: (A) Coronal T1-weighted and (B) coronal T2-weighted MR images show the necrotic lesion with fat-like signal intensity (asterisk in A), surrounded by a low T1 rim (arrow in A). On spin-echo T2-weighted images, the double line sign is frequently seen (arrow in B). (C) Coronal T1-weighted MRI shows the non-fatty signal intensity of the necrotic lesion (asterisks).

The MR appearance of the fractured ONFH is variable. Subchondral bone plate fracture appears as a frank and abrupt deformity of the epiphyseal contour. It is best seen on fat-saturated intermediate-weighted images than on T2-weighted images because of the better delineation of the cortical bone between the overlying cartilage and the underlying infiltrated marrow (Figure 5). Subchondral bone plate fracture also appears as global flattening of the epiphyseal contour. Subchondral trabecular fracture may appear as a high signal intensity line on fluid-sensitive sequences running parallel to the subchondral bone plate (Figure 5). Occasionally, the fracture also shows low signal intensity on T2-weighted images. The depression of femoral head contour usually occurs in the weight-bearing areas of the epiphysis (e.g., anterosuperior aspect of the femoral head) and a subchondral cleft fracture usually appears in the non–weight-bearing areas (e.g., anterior aspect of the femoral head). It must be emphasized that fracture detection at MRI can be difficult. Several authors suggested that the presence of marrow edema surrounding an apparently non-fractured fat-containing necrotic lesion could be a sign of early incipient fracture (75). In the late stages of the disease, with marked epiphyseal deformity (which can be more conspicuous on radiographs than on MR images), signal intensity changes within the lesion are prominent and complex (without residual fat), whereas surrounding marrow may appear normal.

MRI is very sensitive to detect early FHON (72, 76-79). In a recent meta-analysis, the sensitivity of MRI to detect FHON was 93% (80).

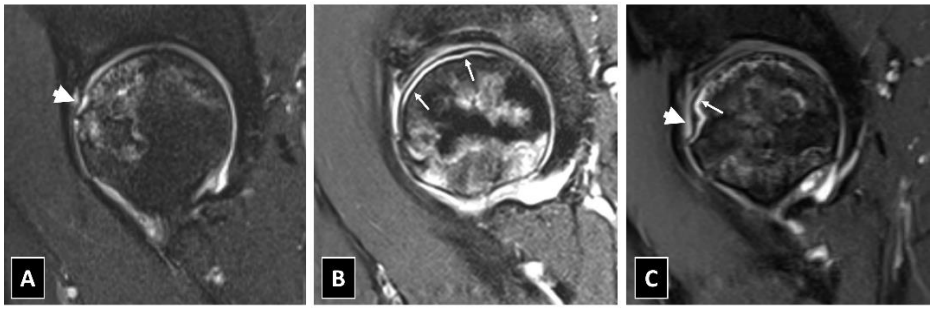

Figure 5:Sagittal PD Fat Sat MR images show cortical deformity (arrowhead in A and C) and subchondral dissection (arrows in B and C).

6.6.3 Computed Tomography (CT)

The CT appearance of FHON is related to bone changes that occur mainly at the interface. The following signs have been described (Figure 6):

a- The "asterisk sign" described on axial images using early generation CT, corresponding to a distortion of the central bony asterisk appearing as clumping and fusion of the peripheral asterisk rays (81).
b- A well-delineated sclerotic band surrounding a wedge-shaped subchondral area, concave towards the articular surface.
c- a lucent cystic region corresponding to areas of bone resorption at the reparative zone.

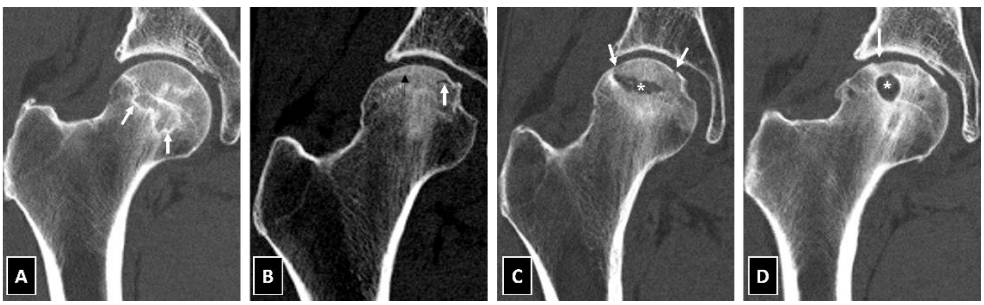

Figure 6: Coronal MDCT reformats show (A) a well-delineated sclerotic band (arrows) corresponding to the sclerotic interface; (B) subchondral trabecular lucency (white arrow) and thin sclerotic line corresponding to trabecular impaction (black arrow); (C) cortical interruption without deformity (arrows) and bone resorption (asterisk); (D) cortical interruption with deformity (arrows) and cystic bone resorption (asterisk)

Studies addressing the sensitivity of CT in detecting FHON date back to the late eighties and early nineties. The sensitivity of CT to detect early FHON is low, in the range of 55% (66). This is attributed to the fact that CT does not demonstrate the early vascular and marrow abnormalities that result in osteonecrosis (82). At MDCT, multiplanar reformats enabled the detection of more subtle alterations in trabecular patterns, joint spaces, femoral-head contours, and acetabula (83).

6.6.4 Other diagnostic modalities

In the 1960s, functional investigation of bone was the mainstay of early diagnosis of FHON by invasively measuring medullary pressure and performing intraosseous venography. Although this procedure was initially used for the study and diagnosis of osteonecrosis, Arlet and Ficat found that patients were often relieved of pain and felt that the clinical course in many cases was improved (10, 11). Thereafter, this procedure was frequently employed in the diagnosis and treatment of osteonecrosis and became known as "*core decompression*."

Before the era of MRI, many radioactive isotopes have been used to diagnose FHON in a pre-radiographic stage, the most commonly used isotope was the 99M technetium diphosphonate. Although these agents often did identify areas of necrosis not seen on plain films, they were neither sensitive nor specific (64, 65, 67, 84). Theoretically, the necrotic region of bone would not take up the isotope and would therefore appear "cold" on the scan. However, the viable areas of bone surrounding the region of necrosis could show increased uptake related to the repair process, frequently masking the lack of uptake in the center of the lesion. Of note, bone scan remains a useful tool to detect Pethes disease, which is beyond the scope of this manuscript.

Single-photon emission computed tomography (SPECT) can demonstrate the avascular focus early in the disease with a sensitivity ranging between 85% for SPECT (67) and 97% for the triple-head high-resolution SPECT(85). A photon-deficient region "cold spot" within the femoral head is highly specific for ON and is the earliest scintigraphic evidence of the disease, usually seen 7-10 days after the ischemic event after fracture or hip dislocation (48, 84, 86). In the following weeks to months, an increased uptake surrounds and eventually replaces the region of photopenia, and it represents the revascularization and repair process. The "doughnut sign" refers to the central region of photopenia with the surrounding zone of increased uptake (84, 87).

Arteriography was used to a limited extent, basically as an investigational tool, and not for clinical diagnosis. The role of other imaging techniques for the diagnosis of FHON has not been well established. These include positron emission tomography (PET) (88), gadolinium-enhanced MRI, and perfusion MRI.

6.7 Natural history of femoral head osteonecrosis

MRI has significantly contributed to increasing our understanding of the natural history of FHON, by enabling an early diagnosis before the onset of symptoms. It is sensitive, non-invasive, and can be repeated, therefore it enabled a follow-up of patients with early stages of FHON.

Follow-up MRI imaging of asymptomatic ONFH showed that the lesions can remain unchanged over time or may partially regress. Prospective studies based on the diagnosis of FHON by MRI reported that symptoms appear in 6 months to 3 years and progress to collapse in 1-7 years (89, 90). In the case of clinically silent lesions, longitudinal MRI studies showed a 15% to 20% risk of appearance of symptoms at 1-year follow-up, and a significant subset of osteonecrotic lesions may remain silent for many years (43, 91, 92). Untreated asymptomatic ONFH has a progression to symptomatic disease or collapse in about 60% during a maximal 20-year follow-up (47). Several authors suggested that the reparative process could be limited to the periphery of osteonecrosis over a long period in non-collapsed ONFH (43) and the complete disappearance of ischemic lesions in adults has been rarely reported (90). In cases of symptomatic ONFH, the collapse usually occurs within 2 years in 32 to 79% of patients (46) and the repair process will be replaced by a destructive vicious circle leading to further collapse (43).

6.8 Pathophysiology of bone collapse

The occurrence of femoral head collapse is a key event in the physio pathogenesis and natural history of the disease. Many factors contribute to fracture and collapse of the articular surface: the accumulation of microfractures, the inability of the non-viable tissue for bone repair, the sclerotic interface acting as a stress riser, together with the imbalance of bone turnover at the interface leading to bone resorption.

The collapse of the femoral epiphysis is the final endpoint that results from the following lesions:

- Fracture of the subchondral bone plate: due to its superficial location, the subchondral bone is subject to the highest stress loading. Due to the inability of

bone remodeling, the microfractures cannot heal and lead to depression of the articular surface. This fracture generally occurs at the margin of the necrotic lesion (14, 93-95)

- Fracture of the trabecular bone: the occurrence of isolated trabecular microfractures due to daily activity is a well-known phenomenon. Usually, these microfractures heal without consequences. In ONFH, the necrotic bone lacks the ability of callus formation, therefore these microfractures do not heal. Instead, they accumulate leading to "macro fractures" and subsequent collapse (96). It frequently runs parallel underneath the subchondral bone plate itself more deeply within the lesion, or at its margin. Usually, the fracture does not extend into the adjacent normal bone.
- Resorption of the trabecular bone: the imbalance of bone turnover at the interface leads to areas of bone resorption, eventually leading to "sinking" of the necrotic lesion and collapse of the articular surface (97).
- Trabecular bone sclerosis at the interface: contributing to an alteration of stress distribution within the femoral head and acting as a stress riser eventually leading to trabecular microfractures at the interface (95, 96, 98-100).

Overall, many observations lead to the hypothesis that the risk for collapse in FHON is under the influence of many parameters that either decrease bone resistance to stress or increase bone stress on the lesion. Patients' characteristics including body mass index (BMI), degree of physical activities, or steroid-associated bone metabolism alteration could favor fracture. Anatomical factors of the involved hip such as increased acetabular retroversion could also favor fracture development (100, 101). Quantitative determination of the extent and location of necrotic lesion on MR images also enable to estimate the fracture risk (91, 101, 102). Femoral heads in which the infarct is either small or involves a limited proportion of the weight-bearing area are less likely to collapse than those with large lesions. Signal changes in lesions could also indicate impending fractures because infarcts with fat-like signal intensity show a collapse-free survival much longer than those with heterogeneous signal (101).

The Japanese Investigation Committee (JIC) classification system includes an assessment of the location of the necrotic lesion according to the three pillars of the articular surface of the acetabulum (24, 25) and was found to have a prognostic value. The more lateral is the lesion, the higher is the risk of collapse (24-26).

6.9 Staging of osteonecrosis

There is general agreement that the presence of epiphyseal fracture represents a pivotal step in the natural history and the staging of ON lesions. A summary of the most commonly used staging systems and methods to quantify the necrotic lesion is provided in appendix 1. Except for JIC (103, 104), intra-observer reproducibility of these staging systems has been assessed in a limited number of patients and it is moderate to fair (105-108).

An effective classification system of ONFH should help to eliminate much of the current confusion about both the natural history and the treatment of ONFH. It should theoretically:

a- Be universal, used in the different parts of the world.
b- Parallel the natural course of the disease.
c- Be sensitive to the progression of the disease namely the detection of fracture.
d- Help establish a prognosis.
e- Determine the best method of management.
f- Enable to compare the effectiveness of different methods of treatment.
g- Be simple and reproducible.

In 2013, ARCO held an international consensus meeting to revise the classification system, but a consensus was not achieved. In October 2018, another attempt was undertaken to revise the 1994 classification system of FHON using a Delphi approach (109). This initiative resulted in the 2019 modified version of ARCO (Table 3) that will be used in this manuscript. It consists of four stages and does not incorporate the previous subclassification or quantitation parameters:

- ***Stage 1:*** Conventional radiographs (CR) are normal, but either magnetic resonance (MRI) or bone scan is positive.
- ***Stage 2:*** CR are abnormal (subtle signs of osteosclerosis, focal osteoporosis, or cystic change in the femoral head), but without any evidence of subchondral fracture, fracture in the necrotic portion, or flattening of the femoral head)
- ***Stage 3:*** fracture in the subchondral or necrotic zone as seen on CR or computed tomography (CT) scans. This stage is further divided into
    - stage 3A (early): femoral head depression ≤ 2 mm
    - stage 3B (late): femoral head depression > 2 mm
- ***Stage 4:*** osteoarthritis on CR: joint space narrowing, acetabular changes, and/or joint destruction.

Table 3: The 2019 revised ARCO staging of femoral head osteonecrosis (109)

ARCO stage	Image findings	Description	
1	CR normal MRI abnormal*	-No changes on CR -Band of low signal intensity around the necrotic area on MRI	
2	CR abnormal MRI abnormal	-Sclerosis, focal osteoporosis, or cystic changes on CR or CT -No evidence of subchondral fracture, fracture in the necrotic portion, or flattening of the FH.	
3 A (early)	Subchondral fracture on CR or CT	Subchondral fracture, fracture in the necrotic portion, and/or flattening of the FH are seen on CR or CT.	FH depression ≤ 2 mm
3 B (late)			FH depression >2 mm
4	CR osteoarthritis	Osteoarthritis of the hip joint with joint space narrowing acetabular changes and destruction are seen on CR.	

* *A cold spot is seen on bone scan. CR=Conventional Radiographs; FH=Femoral Head*

7 Detection of fracture in ONFH using CT: a review of the literature

CT is not commonly performed for the diagnosis and staging of FHON. Its role is mainly restricted to planning for surgical therapy or in patients with contra-indication to MRI (29, 109-117). Studies in the early 2000s showed that MRI had a low sensitivity to detect subchondral fracture when compared to CT in selected patient populations (118, 119). In these two studies, CT was assumed to represent the standard of reference to detect subchondral fracture, an assumption based on prior pilot studies performed by using limited image quality in comparison with the current state of the art (19, 83, 120, 121). Table 4 provides a summary of collapse-related bone changes seen on CT described in these publications.

Table 4: Summary of the publications that addressed collapse-related bone changes on CT in ONFH

Author [year] (reference)	**Study design Number of hips that had CT [number of hips that had CT+MRI]**	**Collapse-related bone changes that were addressed in the study**				**Frequency of CRBC in non-collapsed FH on MRI**
		Cortical interruption	**Trabecular interruption**	**Trabecular impaction**	**Trabecular resorption**	
Magid et al [1985] (83)	Retrospective 45 [45]	Yes	Yes	No	No	N/A
Mitchell et al [1986] (120)	Retrospective 21 [21]	Yes	Yes	No	No	2/13
Stevens et al [2003] (118)	Secondary analysis of prospective trial 45 [38]	Yes	Yes	No	No	5/24
Yeh et al [2009] (119)	Prospective 28 [28]	N/A	N/A	N/A	N/A	25 to 45%
Abumis et al [2013] (122)	Retrospective 57 [57]	Yes	Yes	Yes	No	N/A
Meier et al [2014] (123)	Retrospective 37 [37]	Yes	Yes	Yes	No	18/18
Shi et al [2021] (124)	Retrospective 85 [N/A]	N/A	N/A	N/A	Yes	N/A

N/A: could not be assessed according to the description of the study protocol. CRBC: collapse-related bone changes

A summary of the material, methods, and results found in the literature are provided in the following section with emphasis on collapse-related bone changes at MDCT and on the strengths and limitations of each of these studies.

1- **Stevens et al, 2003** (118): The authors analyzed MRI and CT examinations of 45 ONFH and demonstrated that the sensitivity/specificity of MRI to detect subchondral fracture were 38%/100%, whereas the sensitivity of CT was

94.5% (18/19). Collapse-related bone changes were detected at CT in 5/24 (21%) ARCO 2 hips. Among these 5 hips, four (80%) showed collapse on MRI/CR at 6 months follow-up.

- **Strengths:**
  - Secondary post hoc analysis of imaging data of prospective multicenter clinical trial.
  - Outcome: imaging follow-up after 6 months.
- **Limitations**:
  - Did not assess pain or functional impairment.
  - All hips were treated by core decompression. CT was not performed upon enrollment but at 6 months after treatment.
  - Reading performed by 1 MSK radiologist
- **Additional remarks**:
  - The definition of collapse on CT included subchondral trabecular interruption and cortical interruption. Trabecular impaction and bone resorption were not assessed.
  - The only sign of collapse on MRI was subchondral high T2 cleft.
  - It considered CT as the standard of reference to which MRI was compared.

2- **Yeh et al, 2009** (119): the authors prospectively analyzed MRI images of 28 non-collapsed ONFH according to radiographs and compared the results of MRI staging to a consensus reading on CT performed by two musculoskeletal radiologists. They found that the sensitivity/specificity of MRI to detect collapse were 61%/40% with a very low interobserver reproducibility. In addition, CT detected collapse-related bone changes in 25-45% of non-collapsed femoral heads on MRI and radiographs.

- **Strengths:**
  - Prospective study
  - CT and MRI were performed on the same day
  - Separate reading of MRI by general and MSK radiologists
- **Limitations**:
  - Selection bias: 28/28 hips had bone marrow edema (BME) on MRI.
  - The technical platform below state-of-the art: single row CT was used
  - Lesion definition of collapse on CT was not clear.
  - The process of consensus reading of CT images is not defined.
- **Additional remarks:**
  - signs of collapse on MRI included cortical interruption, high T2 cleft, and low T2 lines.

3- **Abumis et al, 2013** (122)**:** The authors retrospectively analyzed 57 ONFH with (n=30) and without (n=27) BME on MRI. They demonstrated that hips with BME showed more fractures on CT and MRI and had a less favorable prognosis. They also assessed the signal of collapse-related changes on MRI (65% low T2, 21% high T2, 14% mixed signal on T2) and the density of trabecular changes on CT (68% lucent, 20% sclerotic, 12% mixed lucent, and sclerotic).

- **Strengths:**
    - Assessed outcome and related it to BME.
- **Limitations**:
    - Retrospective study with many flaws in its design, unclear inclusion criteria, and missing clinical data
    - The process of consensus reading by 2 MSK radiologists is not defined.
- **Additional remarks:**
    - Included bone sclerosis corresponding to trabecular impaction among collapse-related bone changes.

4- **Meier et al, 2014** (123)**:** The authors analyzed 37 ONFH with BME on MRI using CT as a standard of reference to detect collapse. They demonstrated that 19/37 (51%) showed collapse on MRI and 37/37 (100%) on CT. Therefore, CT upgraded ARCO 2 hips with BME to ARCO 3 in 18/37 femoral heads. This study demonstrated that BME may be an indicator of early collapse on MRI

- **Strengths:**
    - All hips were untreated.
    - Histology was obtained in 14/37 (38%).
    - State-of-the-art equipment: 64-row MDCT, 3mm slice thickness of MRI images.
- **Limitations**:
    - Retrospective design subject to selection bias: all patients had pain and all hips had BME.
    - The process of consensus reading by 2 MSK radiologists is not defined.
- **Additional remarks:**
    - Signs of collapse on MRI were dome depression, high T2 cleft, and low T2 lines
    - signs of collapse on CT were cortical depression, subchondral radiolucent line, subchondral radiopaque line.

5- **Shi et al, 2021**(124): The authors analyzed 2-year follow-up CT images of 85 ARCO 2 (n=62) and ARCO 3A (n=23) ONFH with bone resorption on CT. They demonstrated that more rapid collapse occurred in femoral heads with a larger volume of bone resorption, those with resorption located anteriorly or involving the lateral pillar of the FH.

- **Strengths:**
    - included a large number of untreated non-collapsed hips, or hips with early collapse
    - 2-years follow-up using CT was available.
    - Two radiologists performed independent readings then achieved consensus agreement.
- **Limitations**:
    - this study lacks a clear definition of bone resorption
    - Other collapse-related bone changes were not assessed
    - Retrospective study subject to selection bias: all FH presented bone resorption.
- **Additional remarks:**
    - Used 2019-ARCO without further details on the use of MRI and CR
    - Population demographics are not usual in FHON: F>M, bilateral disease in 15/70 (21%).

These studies share some limitations in their methodology:

- The number of patients is small, with variable inclusion criteria.
- The definition of CRBC is variable both on MRI and on CT.
- The reading process and interobserver reproducibility were not always assessed.
- Lack of clinical correlation.

8 Aims of the thesis.

- To develop a co-registration method to obtain matched µCT and histology images of ONFH that were analyzed using the grid overlay method (step 1).
- To assess the topology and connectivity of cortical and trabecular microfractures at µCT with histological correlation using the grid overlay method. Grid boxes with trabecular microfractures formed elongated clusters and were concentrated near the femoral head surface (step 2).
- To assess the accuracy of MDCT imaging of resected ONFH specimens to detect bone changes in comparison with µCT. MDCT appeared to have high specificity but limited sensitivity for the detection of CRBC in comparison with µCT (step 3).
- To compare the frequency of grid boxes with CRBC at MDCT between ONFH with limited and advanced collapse. The frequency of cortical microfractures and bone resorption but not that of trabecular microfractures was higher in advanced than in limited collapse (step 4).
- To assess the frequency of CRBC at MDCT in 78 ARCO 1-2 and 54 ARCO 3-4 ONFH and to compare clinical and MRI data between ARCO 1-2 hips with or without collapse-related bone changes at MDCT. Collapse-related bone changes were detected on MDCT in all ARCO 3-4 FH and in 26-40% of ARCO 1-2 FH. There was no difference in clinical and MRI data between ARCO 1-2 hips with or without CRBC at MDCT (step 5).

9 STEP I: Technical note: Fused micro-computed tomography (µCT) and histological images of bone specimens

Collaborators: Christine Galant MD, Kjell Laperre, Marin Halut MD, Maité Van Cauter MD.

Publication reference: Fused micro-computed tomography (µCT) and histological images of bone specimens. Mourad C, Laperre K, Halut M, Galant C, Van Cauter M, Vande Berg BC. Diagn Interv Imaging. 2018 Jul-Aug;99(7-8):501-505. Doi: 10.1016/j.diii.2018.01.011.

9.1 Introduction

Radio-anatomical correlations have contributed to increase our understanding of medical images. In the setting of bone specimens, two methods have been developed to overcome the technical challenge due to the presence of a hard mineralized and a soft non-calcified component. The first method consists of decalcifying the bone specimen before tissue sectioning. It enables to evaluate all tissue components except the calcified one. The second method consists of embedding the specimen in resin and sawing it without decalcification; it enables the evaluation of the mineralized component at the expense of the non-calcified tissue.

Micro-CT (µCT) is a nondestructive imaging tool that displays the mineralized components of bone without the need for resin-embedment. After µCT data acquisition, the specimen can be decalcified and processed according to the usual histological techniques. Thanks to its high spatial resolution, µCT images can be retrospectively reformatted to match the histological sections. This concept has been applied to human dental implants and animal bone graft specimens (125-127). This report aims to describe a stepwise process to obtain fused images from µCT and histological images of bone specimens.

9.2 Materials and methods

The investigator's institutional review board approved the study, waiving the informed consent of the patient (BE403201526413). Four femoral head specimens from 3 men and one woman (median age of 55 years; range 30 to 67 years) who had total hip replacement for osteoarthritis (n=2) and osteonecrosis

(n=2) were sampled. µCT data acquisition and post-processing imaging were performed by a fellow in musculoskeletal radiology who was qualified to operate a µCT scanner (SkyScan 1173 microtomograph, Bruker Company, Kontich, Belgium).

The procedure was performed according to a rigorous stepwise process summarized in Figure 7. The entire specimens were scanned at a nominal resolution of 50 µm (130 kV; brass filter; Camera pixel binning of 2x2; scan orbit 360°; rotation step 0.25°; isotropic voxel volume: 125000 μm^3, duration: 50 minutes). Raw data reconstruction was carried out with a modified Feldkamp algorithm (128) using the SkyScan™ NRecon software accelerated by a Graphics Processing Unit (GPU)(129). Data were anonymized and stored on an external hard disk. The same radiologist used free software (Dataviewer, Bruker, Kontich, Belgium) with multiplanar capacity to view the images and detect focal bone lesions. The entire specimens were cut with a diamond band saw (EXAKT 312, Germany) to obtain 2x2x2 cm blocks containing the focal lesions.

A second µCT data acquisition at a nominal isotropic resolution of 12 µm was performed on these small blocks (90 kV; Al filter; no pixel binning; scan orbit 360°; rotation step 0.2°; isotropic voxel volume: 1728 μm^3; duration: 120 minutes). The blocks were sawed and the 2-mm sections that included the lesions were decalcified (formamide solution) and embedded in paraffin. Five microns thick sections were cut, mounted on glass slides, and stained with Hematoxylin and Eosin. Histological sections were digitized using Hamamatsu Nano Zoomer 2.0 rs. Digital Slide Scanner with a resolution equivalent to an (x40) optical magnification.

The digitized histological sections were loaded on one screen of a dual-screen workstation using a Nano Zoomer Digital Pathology viewer (Hamamatsu) under low-field magnification. The high-resolution µCT images of the corresponding block were viewed on the neighboring screen by using MPR reformatting (Dataviewer). µCT reformats were visually adjusted by scrolling and rotating the image from the isotropic 3D dataset, using a landmark-based manual registration to obtain one µCT image that would duplicate the histological slice in a near-perfect way. Fused µCT-histological images were generated using the 2D manual registration function on Dataviewer version 1.5.4.0, which uses an intensity-based registration method. The adjustment on Dataviewer was manually performed by using tools including zoom factor, image rotation, and image translation under direct visualization of the super-imposed registered images.

A short video display was performed from a series of fused images using MAGIX slideshow Maker 2, with a progressive transition from pure µCT to pure histology images. The registration and fusion process took around 30 to 90 minutes per video.

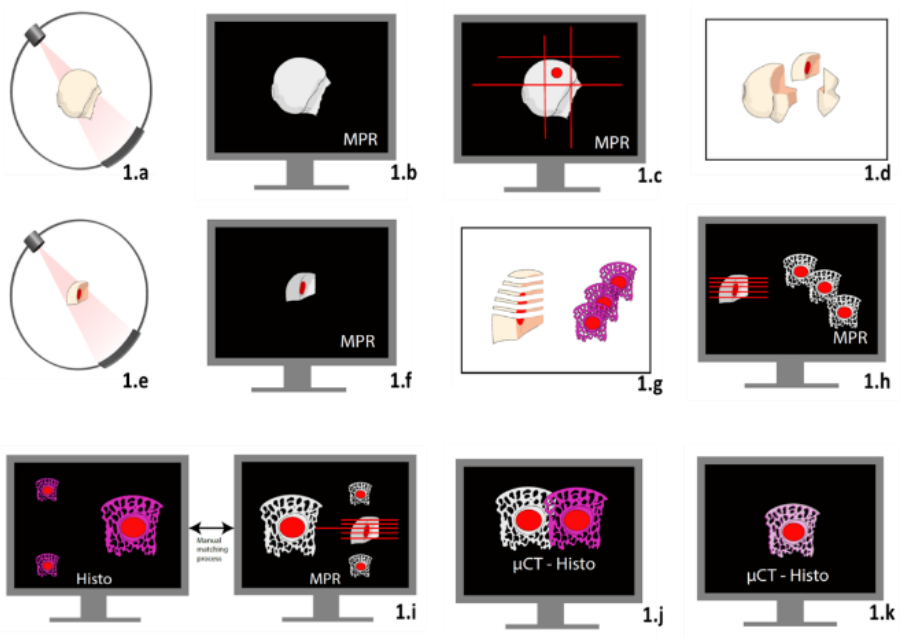

Figure 7: Schematic representation of the stepwise process to obtain fused images of µCT and histology (Illustration by Marin Halut, MD)
1.a- The entire specimen is scanned (50µm isotropic voxels) and data is stored. 1.b- µCT images are viewed on a workstation using multiplanar reformats and 3D rendering. 1.c- The lesion is identified on µCT images. Multiplanar reformatting is used to plan for sawing the specimen. 1.d- The specimen is sawed according to the planning in 1.c by using surface landmarks. Blocks of 2 cm are obtained. 1.e- The specimen blocks are scanned (12µm, isotropic voxels) and data is stored. 1.f- µCT images of the specimen blocks are viewed on a workstation using multiplanar reformatting and 3D rendering to locate the lesion. 1.g- The specimen blocks are sectioned, decalcified, and histological slices prepared. 1.h- µCT images of the specimen blocks are viewed on a workstation using multiplanar reformatting to locate the lesion. 1.i- A dual-screen workstation is used for manual registration of µCT images and digitized histological sections using a landmark based visual registration. 1.j- The digitized histological slices and the matched µCT images are processed and stored. 1.k- Fused µCT-histology images are obtained and displayed as images or in a video mode.

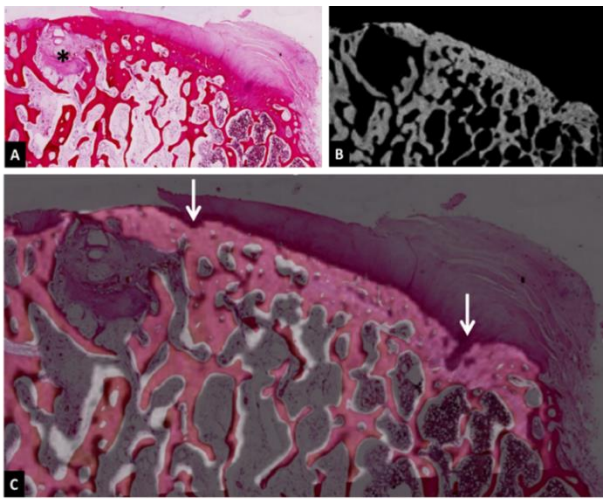

Figure 8: Histological section of a subchondral bone cyst (asterisk) in a specimen with osteoarthritis. (B) The corresponding µCT image was reformatted according to the histological image. (C) On the fused µCT-histological image, the small indentation of the subchondral bone plate (arrow) contains fibrocartilage tissue.

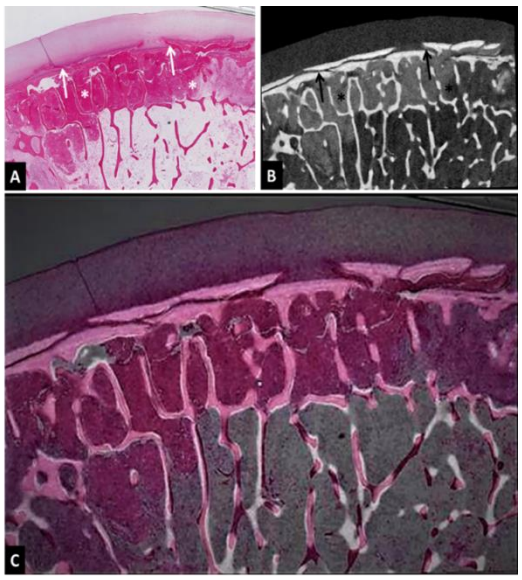

Figure 9: (A)Histological section, (B) corresponding µCT reformatted image, and (C) fused image of a specimen with osteonecrosis. The delamination fractures within the subchondral bone plate are detected at µCT imaging and are retrospectively visible at histology (arrows in A and B). The eosinophilic debris on the histological section show increased density on the µCT image (asterisks in A and B).

9.3 Results

Micro-CT reformats of the four lesions could be successfully fused with the corresponding histological images with a near-perfect match of the bone trabeculae. Fused µCT -histological images of a bone cyst in osteoarthritis (Figure 8) and subchondral bone plate fracture in osteonecrosis (Figure 9) were obtained. The accuracy of the registration was visually estimated by the same fellow during the procedure, based on rigid landmarks within the images (for example, the adequacy of alignment of the subchondral bone plate, fracture lines, the superposition of the wall of the subchondral cyst.). The videos displayed the fused images in a *yoyo mode* by using a progressive variation in transparency, shifting from the µCT to the histological image.
(https://www.sciencedirect.com/science/article/pii/S2211568418300329?via%3Dihub#sec0035).

9.4 Discussion

The current report demonstrates the feasibility of fusing histological sections of human femoral head specimens with the corresponding µCT images thanks to the spatial resolution of µCT imaging.

Without µCT, it was impossible to obtain both the bone and the histological images of exactly the same section, since the usual specimen preparation to get the histological image cannot be performed after resin embedding needed to obtain the bone image. The proposed technical approach opens several perspectives: µCT images obtained before sectioning enables confirmation of the artefactual origin of substance loss or anatomical distortion seen on the histological images due to sectioning and dehydration (125). They could also depict bone changes that might not be striking at microscopic analysis, like micro-fractures and calcium deposits within tissue. In addition, the isotropic acquisition of the entire volume of the specimen potentially enhances our understanding of the histological image by adding a 3D dimension to our analysis. It will also be possible to integrate within histological features some quantitative parameters (3D histomorphometry, texture analysis …) derived from the corresponding µCT data, similar to what has already been performed in diffuse bone disorders (130).

According to our experience, the most challenging step of the process was to obtain a high level of precision in merging µCT and histological images. In the current report, we used a manual landmark-based visual co-registration that still requires time-consuming interaction. Dedicated software can perform a fast and robust registration, but they still require some user interference (131-135).

Similarly, CT-guided automated sectioning of the specimen could be implemented similar to computer-aided surgery. Nevertheless, we deliberately used free software so that researchers around the world can perform image registration in an affordable way.

In addition to the limited number of cases, our study has a few other limitations. The procedure was applied only on bone samples and not on soft tissue components, the size of which is altered by dehydration and retraction during histological preparation (133, 136). Many steps remain human-dependent and are likely to interfere with the quality of the fused images and may affect reproducibility when compared to automatic registration. Therefore, the reproducibility of this method should also be assessed on a larger number of specimens. Finally, the fact that the entire procedure was performed by the same radiologist could have facilitated the fusion process of the µCT and histological images. However, once isotropic high-resolution µCT data of a bone specimen are obtained and stored, it is possible to retrospectively adapt the reformatted µCT images to any histological image thanks to the multiplanar capacity at post-processing.

In conclusion, we have presented a stepwise process integrating µCT images reformatted according to histological sections to obtain radio-anatomical correlations of bone specimens.

10 STEP II: topology of microfractures in osteonecrotic femoral heads at µCT and histology (in vitro study)

Collaborators: Christine Galant MD, Emilie Wacheul MD, Nicolas Michoux and Thomas Kirchgesner MD.
Publication reference: Topology of microfractures in osteonecrotic femoral heads at µCT and histology. Mourad C, Galant C, Wacheul E, Kirchgesner T, Michoux N, Vande Berg B. Bone. 2020 Dec;141:115623. Doi:10.1016/j.bone.2020.115623. Epub 2020 Aug 30. PMID: 32877712.

10.1 Highlights

- Cortical and trabecular bone microfractures are frequent in collapsed ONFH and are ubiquitous.
- Trabecular microfractures predominate in the superficial layer of the epiphysis and form elongated clusters (Figure 10).
- Microfractures in viable areas of ONFH and in OA femoral heads are scattered in the superficial subchondral areas of the femoral heads and do not form clusters.

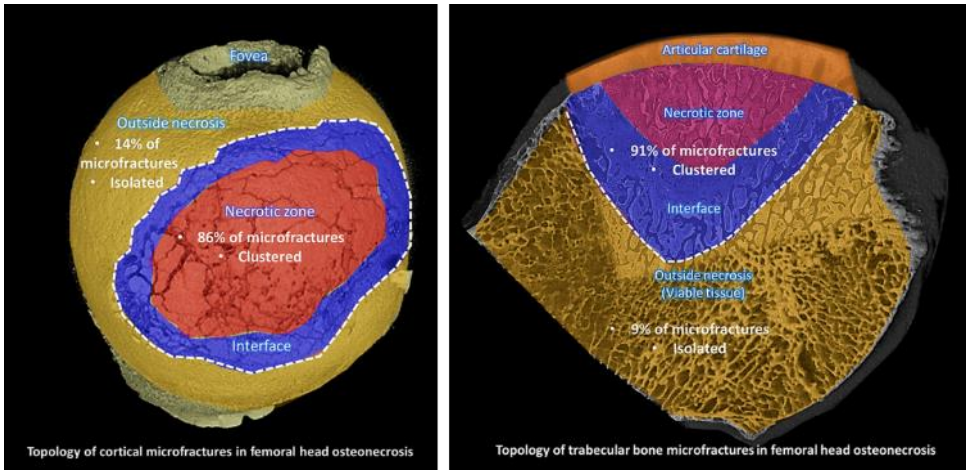

Figure 10: 3D µCT reformats show the distribution of microfractures within the different zones of the necrotic lesion

10.2 Introduction

Epiphyseal collapse refers to the spontaneous failure of the subchondral bone plate and underlying bone appearing in a non-traumatic setting frequently, but non exclusively, in osteonecrosis (137). Cartilage and bone fractures along with bone resorption have been described in epiphyseal collapse at imaging (118, 122, 138). In clinical practice, MRI is the modality of choice to diagnose FHON, however, early collapse can be missed on MRI but can be detected on MDCT as shown in one study (118). Staging of ONFH remains difficult with limited interobserver reproducibility indicating the need for a better understanding of epiphyseal collapse (105, 106, 108, 139) Therefore, the standard of reference for the staging of FHON is yet to be determined.

Microcomputed tomography (µCT) is a high-resolution imaging technique that enables the analysis of bone components and architecture in a non-destructive way contrary to the usual histomorphometry techniques that require fixation in methyl methacrylate resin. This bone processing alters the tissue and does not enable further histological staining. The use of µCT is non-destructive and enables further histological processing of the same specimen. µCT of resected ONFH demonstrated quantitative histomorphometric bone changes with little information on cortical and trabecular bone microfracture (47, 140-143). The current µCT and histological study aimed to assess the topology of bone and cartilage microfractures in resected human femoral heads with ON and contribute to a better understanding of the failure pattern of the FH.

10.3 Material and Methods

10.3.1 Patients' population

The institutional review board approved the study, with the informed consent of the patients being waived (BE403201526413). Between September 2015 and October 2017, a fellow in musculoskeletal radiology collected 11 consecutive FH specimens with ON (6 men; mean age:46.5 years; range: 30-67 years) and 5 women (68.6 years; 43-85 years) resected for total hip replacement. Meanwhile, he also collected five FH specimens with OA (2 men and 3 women, (72.2 years; 40-90 years) (Figure 11). Causes for ON included steroid (n=5), alcohol abuse (n=1) or was idiopathic (n=5). Preoperative diagnosis of ON was based on radiographs (n=9; mean delay between radiographs and surgery of 48 days; range: 1-132) and on MRI (n= 6; mean delay between MRI and surgery of 75 days; range:2-194). All ON femoral heads demonstrated collapse at pre-operative imaging including five ARCO 3-early, five ARCO 3-late, and one ARCO 4

osteonecrotic femoral heads (144). After resection, all FH specimens were fixed in a formalin buffered solution.

10.3.2 µCT imaging and histological preparation

The same radiologist sawed the 16 femoral heads (EXAKT 312 diamond band saw, Germany) according to preoperative imaging to obtain 28 blocks of 2 x 2 cm (1.75 blocks per specimen; min 1; max 3). The 28 blocks were scanned by using a µCT scanner (SkyScan 1173 microtomograph, Bruker Company, Kontich, Belgium) at a nominal resolution of 12 µm (90 kV; Al filter; no pixel binning; scan orbit 360°; rotation step 0.2°; voxel volume: 1.728 10^{-9} ml; duration: 120 minutes) (145). The blocks were decalcified with a formamide solution for 24 hours and embedded in paraffin. After µCT imaging, the radiologist obtained 47 sections for histological analysis (Figure 11). Thirty sections obtained from ON femoral heads contained ON lesions. Eight sections were obtained from ON femoral heads and nine sections from OA femoral heads did not contain ON lesions. Forty-seven (1 to 3 sections per specimen) 5-microns thick sections were cut, mounted on glass slides, stained with Hematoxylin and Eosin, and digitized (Hamamatsu Nano Zoomer 2.0 rs.) at a resolution equivalent to an x40 optical magnification. The histological sections were selected based on the µCT imaging of the whole femoral head and tailored to include the different regions of the osteonecrotic lesion (within the necrosis, at the interface, and outside necrosis), the different bone components (cartilage, cortical and trabecular bone) and to avoid artifacts related to surgery. The number of sections varied depending on the size of the osteonecrotic lesion. The 47 histological images were viewed on dedicated software (Nanozoomer Digital Pathology Viewer 2.6.8, Hamamatsu Photonics K.K., 2016) and a 2-mm scale bar was inserted in the images. For each histological section, the same radiologist obtained a µCT reformat that matched the digitized histological section by using landmark-based manual processing using a multiplanar reconstruction software (Dataviewer Bruker Dataviewer version 1.5.4.0, Bruker, Kontich, Belgium) as previously described in step 1 (145). A 2-mm scale bar was inserted in every image.

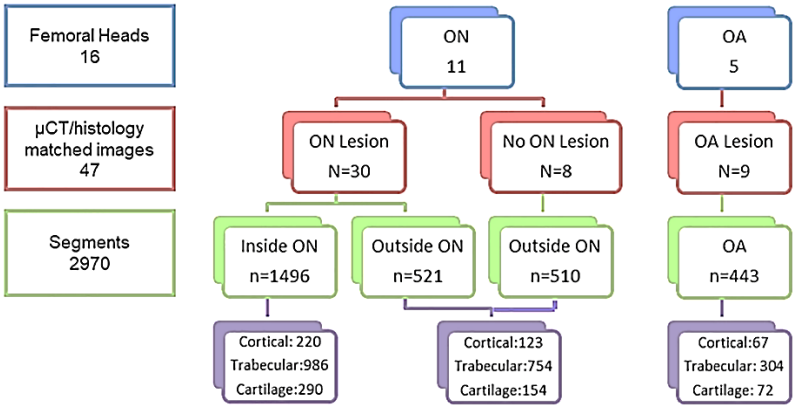

Figure 11: Flowchart of the study material indicating the number of resected femoral heads with osteonecrosis (ON) and osteoarthritis (OA), the number of matched µCT and histology images, the number of segments with or without necrotic lesion and the number of segments containing cortical bone, trabecular bone, and hyaline cartilage.

10.3.3 Image segmentation and labeling of segments

The 47 matched µCT and histology images were segmented using the grid overlay method, by applying a transparent grid on each image and were identically magnified so that the 2 x 2 mm scale on the images corresponded to one grid box (Figure 12-14) In the 38 matched µCT/histological images from the ONFH specimens, there were 2107 segments (mean +/-SD per specimen: 55.45 +/-12.57; range: 25-88) that contained cortical bone (n=343), trabecular bone (n=1740) and articular cartilage (n=444). In the nine matched µCT/histological images from the OA FH specimens, there were 395 segments (43.9+/-15.2 range: 26-76) that contained cortical (n=67) or trabecular bone (n=304) and articular cartilage (n=72). Grid boxes whose surface contained less than 25% of tissue were excluded. The µCT and histological images were translated and rotated so that each grid box contained the same areas of the µCT and histological images. (Figure 12-14).

A pathology resident analyzed the 47 histological sections using a microscope and labeled each grid box according to its dominant histological content and location with respect to the articular surface. Grid boxes containing hyaline cartilage or cortical bone were all superficial and classified in three histological patterns based on the microscopic appearance of the adjacent bone and marrow including necrotic tissue, reactive interface, or viable tissue as described below (12, 15, 63, 146-148). Grid boxes containing trabecular bone were classified according to location and the same histological patterns. Superficial grid boxes

were located within two millimeters below the cortical bone covered by hyaline cartilage and deep segments were located deeper. Three histological patterns were defined as follows: (63, 149). Necrotic tissue consisted of necrotic trabeculae with saponified or mummified bone marrow necrosis(12, 13, 146). Scattered empty osteocytes lacunae within trabeculae embedded in viable marrow were not considered to represent necrotic tissue (12, 15, 146, 150). The reactive interface consisted of a layer of fibrovascular connective tissue with trabecular bone resorption or sclerosis surrounding necrotic tissue (12). Viable tissue consisted of normal bone and marrow devoid of necrotic or fibrovascular tissue that was located at distance from the ON lesion (Figure 15). The osteonecrotic lesion corresponds to the necrotic tissue (the necrotic core) and reactive interface at its margin. Some grid boxes were assigned to different categories depending on the presence of cartilage, cortical and trabecular bone.

10.3.4 Lesion definition and image analysis

In December 2018 and January 2019, a musculoskeletal radiologist with 28 years of experience who was blinded to the histological findings analyzed the 47 µCT images to assess cartilage, cortical bone, and trabecular bone microfractures. During the same period, a bone pathologist with 25 years of experience who was blinded to the µCT images analyzed the 47 histological images to assess cartilage, cortical and trabecular bone microfractures. Readers were blinded to clinical information and pre-operative findings. For each matched image, the same list of grid boxes to be analyzed (identified by letters and numbers) was given to the readers. For each segment, readers documented the likelihood for the presence of cartilage or bone fracture by using a four-point Likert scale (0= not present, 1: probably not present, 2: probably present, 3: present).

Lesions were defined as follows: Fracture of the cortical bone of the subchondral bone plate was defined as a focal linear full-thickness interruption of the cortical bone with or without angulation/displacement of the edges of the fracture at histology and at µCT (Figures 12-14,16). The presence of smooth focal deformation of the subchondral bone plate without interruption was not considered to be a fracture. At histology, the presence of adjacent tissue alterations was used to differentiate non-displaced fractures from physiological interruptions of the subchondral bone plate that contained marrow and normal vessels. Fracture of the trabecular bone was defined by the presence of sharp or irregular interruption of at least two adjacent trabeculae with or without displacement (Figure 12-14, 16).

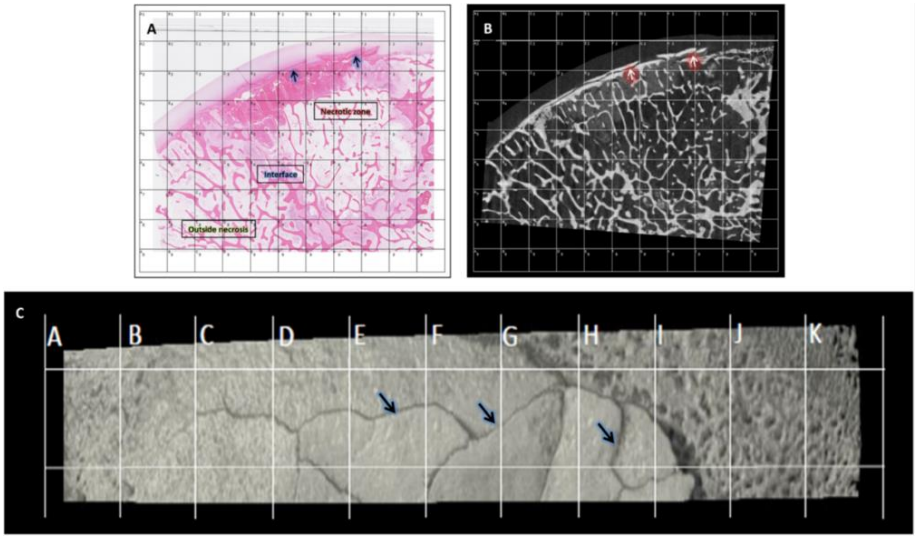

Figure 12: 30-year-old man with left hip steroid-induced osteonecrosis (ARCO stage 3-late). (A) Low magnification histological section (H&E stain) of the resected femoral head specimen with superimposed grid, and corresponding µCT (B). Multiple microfractures of the cortical bone of the subchondral bone plate are well depicted (arrows in A and B). (C) surface 3D µCT view shows cortical microfractures (arrows).

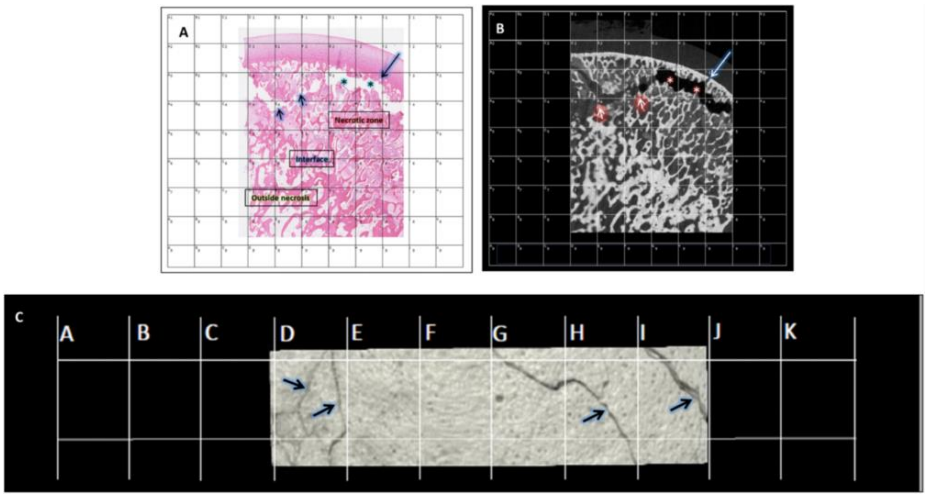

Figure 13: 43-year- old woman with left hip osteonecrosis (ARCO stage 3-early). (A) Low magnification histological section (H&E stain) of the resected femoral head specimen with superimposed grid, and corresponding µCT (B) showing microfractures of the trabecular bone in the superficial (asterisks) and deep layers (arrows) of the necrotic zone. (C) surface 3D µCT view shows associated cortical microfractures (arrows).

The presence of small bone fragments clustered in a limited area was also considered to represent fractures even in the absence of interrupted trabeculae. Smooth interruption of the trabeculae was considered a normal finding. Longitudinal vertical cracks along cement lines within the trabeculae were not considered. When a microfracture occurred at the intersection of two adjacent segments, only one segment was considered positive, by convention the one closest to the articular surface. The reason behind this is to avoid an artificial increase in the microfracture number by encoding the same fracture in two adjacent segments. Fracture of the articular cartilage was defined as a full-thickness linear interruption of the cartilage tissue at histology (138) and µCT (Figure 16). Cartilage changes due to degeneration were not taken into consideration. Folds, lines, tissue retraction, chatter, or crushing at the trajectory of surgical instruments were considered to represent artifacts. The two readers trained during a common session to reach an agreement upon lesion criteria by analyzing five pairs of µCT/histological images that were not included in the study material.

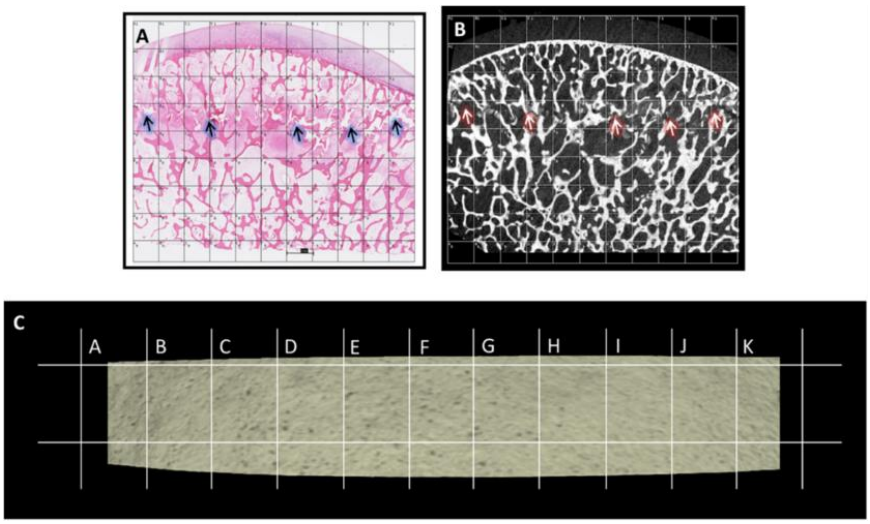

Figure 14: 37-year-old man with right hip steroid-induced osteonecrosis (ARCO stage 3-early). (A) Low magnification histological section (H&E stain) of the resected femoral head specimen with superimposed grid, and corresponding µCT (B), showing trabecular microfracture along the reactive interface (arrows). (C) surface 3D µCT view shows the lack of cortical bone microfracture.

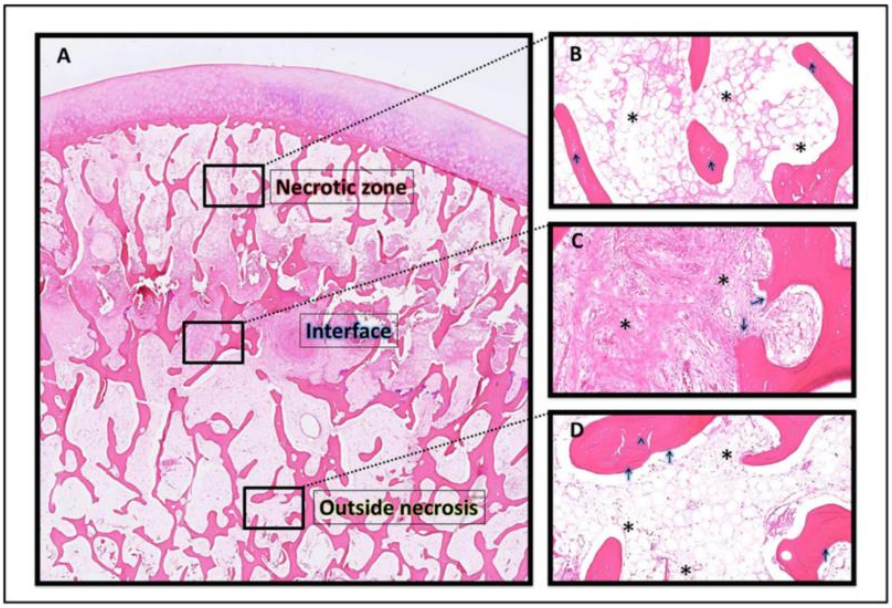

Figure 15:37-year-old man with right hip steroid-induced osteonecrosis (ARCO stage 3-early). (A) A low magnification histological section (H&E stain) of the resected femoral head specimen shows the zonal distribution of the osteonecrotic lesion. (B) High magnification view of the necrotic zone shows empty osteocyte lacunae (arrows), dead adipocytes with absent nuclei (asterisks). (C) High magnification view of the reactive interface shows resorbed edges of the trabeculae (arrows) and reactive bone marrow (asterisks) rich in fibrovascular tissue. (D) High magnification view of the viable bone outside osteonecrotic lesion shows apposition of viable bone (arrows) on dead trabeculae with empty osteocyte lacunae (arrowhead), and viable bone marrow with normal adipocytes (asterisks).

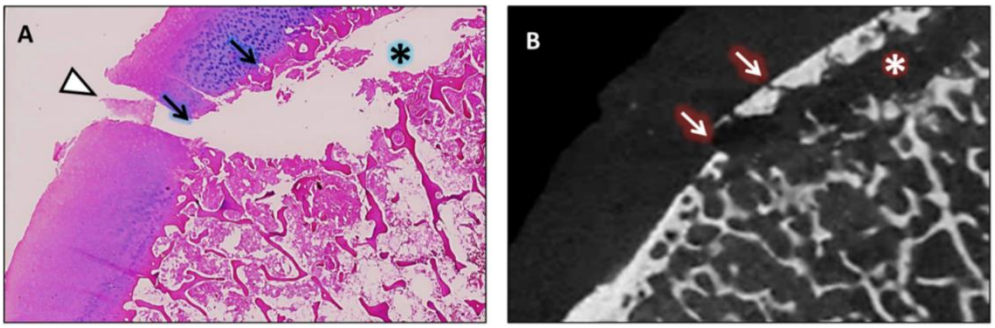

Figure 16: 73-year-old woman with idiopathic osteonecrosis. Low magnification histological section (H&E stain) (A) and corresponding reformatted µCT image (B) resected femoral head specimen with osteonecrosis. The fracture of the cartilage is visualized only on histology (arrowhead in A). Multiple cortical (arrows) and trabecular subchondral (asterisk) micro-fractures are well visible on both images.

10.3.5 Grid cell topology of segments with microfractures

For each 47 µCT and 47 histological images, a statistician created two matrices including all segments with cortical or trabecular bone. Grid boxes containing cartilage fractures at histology were not analyzed because of their limited numbers. Results of readings were encoded in the corresponding matrices. Pixels with "1" corresponded to grid boxes with microfracture and pixels with "0" corresponded to grid boxes without microfracture. The 94 µCT matrices including the 47 matrices for cortical bone microfractures and 47 matrices for trabecular bone microfractures matrices and the corresponding 94 histological matrices were analyzed using the function regionprops of Matlab (Matlab version R2017a, MathWorks) to calculate several parameters (Table 5). An 8-connected pixel two-dimensional connectivity model was used, defined as follows: pixels are connected if their edges or corners touch. Two adjoining pixels are part of the same object if they are both on and are connected along the horizontal, vertical, or diagonal direction (Figure 17). The parameter tends to 1 when the shape of the cluster tends to a circle and becomes superior to 1 if the cluster is elongated.

10.3.6 Statistical analysis

The frequency of grid boxes with cortical, trabecular, and cartilage microfracture at µCT and at histology was determined in the different zones of ON lesions and in OA lesions. The frequency of trabecular microfracture in the superficial layer of the ON lesions was compared with that in the deep layers of the lesions by using the Chi-squared test. The percentage of agreement on a square-by-square basis was calculated between µCT and histological readings for the detection of cortical, trabecular, and cartilage fracture in all the specimens. Kappa values were calculated and levels of agreement were interpreted using the mean value of the confidence interval according to the scale proposed by Altman (< 0,20 : *poor* ; 0,21-0,40 : *fair* ; 0,41-0,60 : *moderate*; 0,61-0,80 : *good* ; 0,81-1,00 : *very good*)(151). The connectivity parameters of segments with cortical and trabecular microfracture in ON lesions were compared with those observed in specimens outside ON lesions and with OA by using Chi-squared test.

Table 5: Definitions of the connectivity parameters calculated for the clustered grid boxes with microfractures.

Parameter	Abbreviation	Definition
Largest cluster of microfractures	LC	Corresponds to the largest number of connected pixels with microfractures in every matrix. Pixels are connected if their edges or corners touch. Two adjoining pixels are part of the same cluster if they are both on and are connected along the horizontal, vertical, or diagonal direction.
Number of clusters	$N^{cluster}$	The number of clusters of segments with microfractures regardless of their size.
Surface of the largest cluster	$Surface^{LC}$	Measures the actual number of segments with microfracture in the largest cluster of microfractures present in the matrix.
Sum of the connectivity in the largest cluster	$SumConnectivity^{LC}$	Measures, for each pixel with microfracture, the number of neighboring lesional pixels using an 8-connectivity model, then summing all numbers. As the parameter increases, the more *Blob*-like is the shape of the cluster, and/or the larger the cluster is.
Major axis of the largest cluster	$Major\ axis^{LC}$	Measures the length, in pixels, of the major axis of an ellipse with the same normalized second central moments as the largest cluster of microfractures.
Minor axis of the largest cluster	$Minor\ axis^{LC}$	Measures the length, in pixels, of the minor axis of an ellipse with the same normalized second central moments as the largest cluster of microfractures.
Ratio major axis/minor axis	$Ratio^{LC}$	Measures the ratio Major axis/Minor axis. The parameter tends to 1 when the shape of the cluster tends to a circle and becomes superior to 1 if the cluster is elongated.

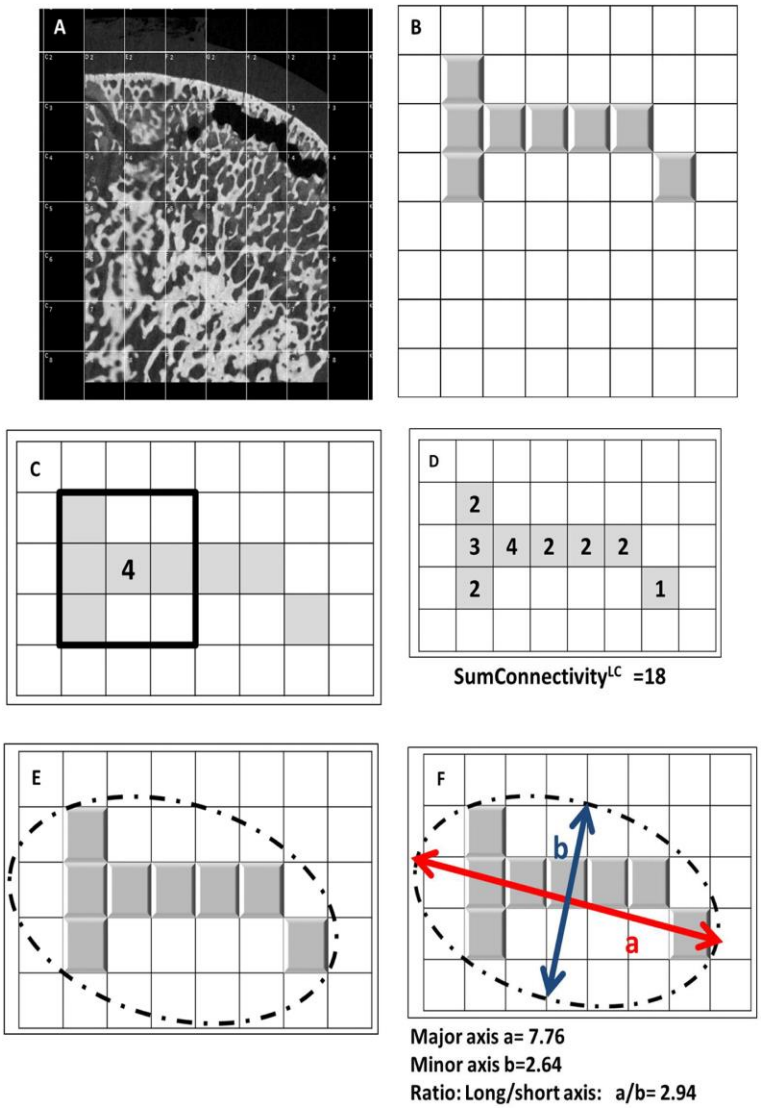

Figure 17: 43-year-old woman with left hip osteonecrosis (ARCO stage 3-early) (same as Fig. 13). (A) Reformatted 2D µCT image with a superimposed grid and (B) corresponding reading grid. Shaded gray grid boxes contain trabecular microfractures. (C) and (D): Example of calculation of the 8-connected pixel two-dimensional connectivity model for a cluster of microfractures. The pixel (arrow in C) is in contact with 4 adjacent lesional pixels by its edges or corners. (D) the "SumConnectivity^{LC}" index corresponds to the sum of the connectivity of all the lesional pixels. (E) And (F): calculation of the Long/Short axis ratio of the cluster. (E) The best fitting ellipse is drawn around the cluster. (F) The parameter "Ratio^{LC}" corresponds to the ratio of the long (a) and short (b) axis of the ellipse.

10.4 Results

10.4.1 Frequency of grid boxes with microfractures in ON and OA FH

In the 38 matched µCT and histological images obtained from ON femoral heads, 29% and 32% of the 343 grid boxes containing cortical bone demonstrated cortical bone microfractures at µCT and histology, respectively (Table 6). 15% (µCT) and 17% (histology) of the 1740 grid boxes containing trabecular bone demonstrated trabecular bone microfractures. 0% (µCT) and 4% (histology) of the 444 grid boxes containing cartilage demonstrated cartilage microfractures. In the 9 matched µCT and histological images obtained from OA femoral heads, a limited number of grid boxes contained microfractures (Table 6 and 7). Grid boxes with cortical and trabecular microfractures were significantly more frequent in ON than in OA specimens at µCT and histology ($p<10^{-3}$ for both techniques). There was no significant difference in the frequency of cartilage microfracture between ON and OA specimens at histology.

Table 6: Frequency of grid boxes with micro-fractures in 47 µCT reformats and corresponding histological sections from ON and OA FH. Grid boxes with bone microfractures are more frequent in ON than in OA FH.

	Frequency of grid boxes with micro-fractures in			
	ON femoral heads (n=11)		**OA femoral heads (n=5)**	
	Number of µCT reformats (n=38)	**Number of histology sections (n=38)**	**Number of µCT reformats (n=9)**	**Number of histology sections (n=9)**
Cortical bone	29% [99/343]	32% [109/343]	7.5% [5/67]	3% [2/67]
Trabecular bone	15% [265/1740]	17% [305/1740]	3% [9/304]	1% [3/304]
Cartilage	0% [0/444]	5% [23/444]	0% [0/72]	4% [3/72]

ON Osteonecrotic; OA osteoarthritic; Percentages represent the frequency of grid boxes with microfracture among all grid boxes with cortical bone, trabecular bone, or cartilage.

Table 7: Frequency of grid boxes with microfractures in superficial and deep zones of 9 µCT reformats and corresponding histological images from OA FH.

	Cortical bone (n=67)		**Trabecular bone (n=304)**		**Cartilage (n=72)**	
	Grid boxes with µ# at µCT (n=5)	**Grid boxes with µ# at histology (n=2)**	**Grid boxes with µ# at µCT (n=9)**	**Grid boxes with µ# at histology (n=3)**	**Grid boxes with µ# at µCT (n= 0)**	**Grid boxes with µ# at histology (n=3)**
Superficial zone	7.5% (5/67)	3% (2/67)	4% (3/71)	0% (0/71)	0% (0/72)	4% (3/72)
Deep zone	NA	NA	2.5% (6/233)	1.3% (3/233)	NA	NA

NA Not applicable; µ# microfracture; *Percentages correspond to the proportion of grid boxes with microfractures among all grid boxes containing cortical bone, trabecular bone, or cartilage within each zone.*

10.4.2 Distribution of grid boxes with microfractures in ONFH

In the 38 matched µCT and histology images obtained from ON specimens, 86% and 82% of grid boxes with cortical bone microfracture and 91% and 96% of grid boxes with trabecular microfractures were located in ON lesions at µCT and histology, respectively (Table 8). At histology, 83% of grid boxes with cartilage microfractures were found in ON lesions.

Table 8: Distribution of grid boxes with bone microfractures in necrotic and in non-necrotic zones in 38 µCT reformats and 38 corresponding histological sections from ONFH. grid boxes with microfractures predominate in ON lesions. Trabecular microfractures involve the superficial and deep layers of the lesions.

		Cortical bone (n=343)		**Trabecular bone (n=1740)**	
		Grid boxes with µ# at µCT (n= 99)	**Grid boxes with µ# at histology (n= 109)**	**Grid boxes with µ# at µCT (n=265)**	**Grid boxes with µ# at histology (n=305)**
In ON lesion	**Superficial zone**	86% (85/99)	82% (90/109)	37% (99/265)	29% (89/305)
	Deep zone	NA	NA	54% (143/265)	67% (205/305)
Out of ON lesion	**Superficial zone**	14% (14/99)	17% (19/109)	5% (14/265)	3% (9/305)
	Deep zone	NA	NA	3% (9/265)	1% (2/305)

NA not applicable; ON osteonecrotic; µ# microfracture. Percentages correspond to the proportion of grid boxes with microfractures among all segments with microfracture.

In the 30 matched µCT and histology images containing necrotic lesions, the frequency of grid boxes with cortical microfractures was significantly higher in the necrotic region than in the interface ($p<10^{-3}$ for µCT and histology) (Table 9) The frequency of grid boxes with trabecular microfractures was higher in the superficial than in the deep layer in the necrotic tissue ($p< 10^{-3}$ for both techniques) and in the interface ($p<10^{-4}$ at µCT and p=0.02 at histology) (Table 9)

10.4.3 Clustering of grid boxes with bone microfractures

Clusters of grid boxes with bone microfractures were found exclusively in ON lesions, with a mean number of grid boxes with cortical microfracture of 2.0 (µCT) and 2.83 (histology) and a mean number of grid boxes with trabecular microfracture of 7.4 and 8.5. (Table 10). The mean of the sum of the connectivity of the clustered grid boxes with trabecular microfracture was 23 at µCT and 29 at histology (Table 10). The mean of the long/short axis ratio of the clustered grid

boxes with trabecular microfracture was 2.4 at µCT and 2.2 at histology (Table 10).

Table 9: Frequency (in %) of grid boxes with microfractures in superficial and deep layers of the central necrotic tissue (necrotic core) and marginal reactive interface in 30 µCT reformats and 30 histological sections containing necrotic lesion from ON femoral heads. Microfractures are ubiquitous and predominate in superficial layers.

		Cortical bone (n=220)		**Trabecular bone (n=986)**		**Cartilage (n=290)**	
		Grid boxes with µ# at µCT (n= 85)	**Grid boxes with µ# at Histology (n= 90)**	**Grid boxes with µ# at µCT (n=242)**	**Grid boxes with µ# at histology (n=294)**	**Grid boxes with µ# at µCT (n= 0)**	**Grid boxes with µ# at histology (n= 19)**
Necrotic core	**Superficial zone**	43% (68/158)	46% (73/158)	55% (82/148)	51% (75/148)	0% (0/231)	5% (16/231)
	Deep zone	NA	NA	25% (112/442)	35% (156/442)	NA	NA
Interface	**Superficial zone**	27% (17/62)	27% (17/62)	32% (17/53)	26% (14/53)	0% (0/59)	5% (3/59)
	Deep zone	NA	NA	9% (31/343)	14% (49/343)	NA	NA

NA not applicable; ON osteonecrotic; µ# microfracture; Percentages correspond to the proportion of grid boxes with microfractures among all grid boxes containing cortical bone, trabecular bone, or cartilage within each zone

10.4.4 Correlations between µCT and histology

The percentage of agreement between µCT and histology was 82% for cortical bone microfracture (kappa=0.54) and 87% for trabecular bone microfracture (kappa=0.48) At µCT, the intraobserver agreement was good for the detection of cortical (kappa=0.725) and trabecular (kappa=0.75) microfractures. At histology, the intraobserver agreement was good for the detection of grid boxes with cortical bone microfractures (kappa=0.66) and moderate for that of grid boxes with trabecular bone microfracture (kappa=0.50).

Table 10: Connectivity parameters of the largest cluster^{LC} of segments with cortical and trabecular microfractures in osteonecrotic and osteoarthritic femoral heads at µCT and histology. Grid boxes with microfractures form clusters and concentrate in the necrotic lesion. Outside the lesion, grid boxes with microfractures are isolated and do not form clusters randomly distributed.

		Osteonecrotic femoral heads				***Osteoarthritic femoral heads***	
		Within ON lesion		**Outside ON lesion**			
		µCT	**Histology**	**µCT**	**Histology**	**µCT**	**Histology**
Cortical bone	**N^{cluster}**	1.24 [0.96;1.52]	1.24 [0.94;1.54]	0.75 [0.16;1.34]	1.25 [0.28;2.22]	0.63 [0.01;1.25]	0.00 [0.00;.38] *
	Surface^{LC}	2.00 [1.00;3.00]*	2.83 [2.01;3.64]	1.00 [0.11;1.89]	0.88 [0.18;1.57]	0.50 [0.00;1.00]*	0.00 [0.00;0.19]
	SumConnectivity^{LC}	2.00 [0.00;4.00]*	2.00 [2.00;6.00]*	0.00 [0.00;2.38]*	0.00 [0.00;2.00]*	0.00 [0.00;0.00]*	0.00 [0.00;0.00] *
	Major axis^{LC}	2.31 [1.15;3.85] *	3.29 [2.35;4.23]	1.25 [0.11;2.38]	1.10 [0.16;2.05]	0.58 [0.00;1.15] *	0.00 [0.00;0.22] *
	Minor axis^{LC}	1.15 [1.15;1.15] *	1.20 [0.96;1.45]	0.72 [0.22;1.22]	0.72 [0.22;1.22]	0.58 [0.00;1.15] *	0.00 [0.00;0.22] *
	Ratio^{LC}	2.28 [1.65;2.92]	2.35 [1.75;2.96]	1.08 [0.10;2.06]	0.96 [0.14;1.77]	0.50 [0.00;1.00] *	0.00 [0.00;0.19] *
Trabecular bone	**N^{cluster}**	1.0 [1.0;2.0] *	1.8 [1.5;2.1]	0.0 [0.0;1.4] *	1.1 [0.4;1.8]	1.0 [0.0;1.0] *	0.0 [0.0;0.9] *
	Surface^{LC}	7.4 [5.6;9.2]	8.5 [6.9;10]	0.0 [0.0;2.6] *	0.9 [0.3;1.4]	1.0 [0.0;1.0] *	0.0 [0.0;0.9] *
	SumConnectivity^{LC}	23 [16;30]	29 [22;36]	0.0 [0.0;3.5] *	0.0 [0.0;0.4] *	0.0 [0.0;0.0] *	0.0 [0.0;0.0] *
	Major axis^{LC}	5.3 [4.3;6.4]	5.5 [4.8;6.3]	0.0 [0.0;2.9] *	1.2 [0.0;1.5] *	1.2 [0.0;1.2] *	0.0 [0.0;1.0] *
	Minor axis^{LC}	2.2 [1.8;2.6]	2.6 [2.3;2.9]	0.0 [0.0;1.3] *	1.2 [0.0;1.2] *	1.2 [0.0;1.2] *	0.0 [0.0;0.0] *
	Ratio^{LC}	2.4 [1.9;2.8]	2.2 [1.9;2.4]	0.0 [0.0;2.2] *	1.0 [0.3;1.6]	1.0 [0.0;1.0] *	0.0 [0.0;0.9] *

*Mean value, *median value, with 95%CI in brackets*

10.5 Discussion

The current study paved the way for a quantitative assessment of microfracture topology in femoral heads at µCT and histology and yields three main results. First, grid boxes with bone-but not with cartilage-microfractures were found more frequently in ON than in OA femoral heads and, in the former case, largely predominated in the necrotic lesions. Second, in ONFH, grid boxes with trabecular microfractures were found in all zones of the necrotic lesions but their frequency was higher in the superficial subchondral layer than in the deep layer. Finally, grid boxes with bone microfractures formed elongated clusters only in necrotic lesions and predominated near the femoral head surface.

Several theories may explain the epiphyseal collapse in ON. According to the “abnormal healing” theory, microfractures within necrotic bone do not heal and

probably tend to accumulate and lead ultimately to overt fracture and subsequent collapse (14, 152). Our results support this theory by demonstrating that microfractures do occur in viable zones of ON femoral heads as in OA femoral heads, but at a much lower frequency than in necrotic lesions where they accumulate. In necrotic and in non-necrotic tissue, trabecular microfractures predominated in the superficial, subchondral layer of the trabecular bone where stresses are likely to predominate. According to the "abnormal stress" theory, trabecular microfracture could also occur in the peripheral areas of osteonecrotic lesions where bone changes -sclerosis or resorption - are likely to alter stress distribution, favoring microfracture development and propagation (98, 140). In agreement with that theory, 9% (μCT) and 14% (histology) of segments located at the interface also showed trabecular microfractures. An underestimation of these fractures is possible because bone resorption may cause a fracture to become invisible or because fractures could heal in viable tissue.

The current study showed that grid boxes with microfractures form elongated clusters in the necrotic areas but not in the viable areas outside necrosis or in OA specimens. This clustering phenomenon potentially reflects the predilection for microfracture to propagate, and that depends on numerous parameters including bulk material properties, microfracture geometry, and stress distribution, magnitude, and rate (153). Despite the higher frequency of grid boxes with microfractures in cortical than in trabecular bone, the mean number of grid boxes per cluster was much lower for cortical bone than for trabecular bone microfractures reflecting fracture propagation in a plane (cortical bone) rather than in a volume (trabecular bone).

Finally, we demonstrated that the frequency of grid boxes with cartilage microfractures was very low both in ON and in OA femoral heads. In addition, no clustering of grid boxes with cartilage microfractures was observed. These observations are in line with the fact that articular cartilage is relatively preserved until late in the ON disease course because of its resilient properties and its nutritional supply by the synovial fluid (148, 154). In the current study, we focused on cartilage microfractures, and we did not assess degenerative changes and abrasion of the articular cartilage in ON and OA specimens. In some instances, limited areas of osteonecrosis may occur in femoral heads with osteoarthritis and this was not the case in our OA specimens (147, 155).

In the current study, spatially matched μCT and histological images were used to detect microfractures and describe their topology. The μCT is a non-

destructive technique that evaluates the mineralized bone component without the use of methyl methacrylate resin, rendering further histological processing possible. The high spatial resolution of µCT is close to histology therefore a simultaneous evaluation with both techniques is possible. The diagnostic performance of each technique was not determined in the absence of a validated standard of reference for the detection of microfractures. Inter-technique agreement for the presence of microfractures was 82% for cortical and 87% for trabecular bone, indicating an acceptable diagnostic performance.

The current study has several limitations. First, because of the limited number of specimens, our results lack statistical power to compare the frequency of microfractures between the different ARCO stages or to correlate them with the ON etiology. In addition, no early-stage femoral head osteonecrosis was included in our study as THR is usually performed in collapsed lesions. Second, we defined bone microfracture as full-thickness transverse interruption of the cortical and trabecular bone. Microcracks occurring within bone lamellae were not considered in the current study. Third, the lack of visibility of cartilage microfracture at µCT could have been related to the inability to modify the window width and levels on PDF images format. Prior staining of the cartilage surface could also have increased the detection rate of cartilage microfracture at µCT (156, 157). Fourth, harvesting of the block specimens was performed according to the femoral head lesions by a radiology fellow who was aware of the imaging findings but did not read the images. Subsequently, the distribution of microfractures was determined with respect to the osteonecrotic lesions and not to the anatomic segments of the involved femoral heads. Fifth, interobserver reproducibility for analysis of the µCT and histological images was not obtained because of the absence of other experts. The radiology and pathology residents involved in the image preparation would not have been blinded readers given the limited number of specimens. Intraobserver reproducibility was determined and was good at µCT and moderate to good at histology.

In conclusion, cortical and trabecular bone microfractures are frequent in collapsed necrotic lesions and are ubiquitous. Trabecular microfractures predominate in the superficial layer of the epiphysis and form elongated clusters. Microfractures in viable areas of ON femoral heads and in OA femoral heads are scattered in the superficial subchondral areas of the femoral heads and do not form clusters.

11 STEP III: Performance of in vitro MDCT to detect bone changes in ONFH: correlation with µCT

Collaborators: Souad Acid MD, Anthony Awad and Nicolas Michoux

11.1 Highlights

- In vitro MDCT has a limited sensitivity but a high specificity to detect
    - Collapse-related cortical interruption
    - Interface-related sclerosis
    - Collapse-related trabecular interruption
    - Collapse-related trabecular resorption

11.2 Introduction

Conventional radiography (CR) and MRI are recommended for diagnosis and staging of FHON (110). More recently, MDCT has been used as a complementary imaging modality for the staging of FHON (109, 118, 119). Thanks to its high spatial and contrast resolution for bone imaging, MDCT demonstrates femoral head deformity associated with cortical bone fractures and trabecular lucencies associated with trabecular bone fractures. More in-depth analysis of MDCT is needed because it could also demonstrate subchondral fractures in non-collapsed ONFH at MRI (118). Micro-computed tomography (µCT) has an even higher spatial resolution than MDCT and enables the detection of trabecular and cortical microfractures in FHON in comparison with histology (140, 142, 145, 158). The current study aimed to assess the performance of MDCT of resected ONFH specimens for the detection of cortical and trabecular bone changes in comparison with µCT with an emphasis on microfractures.

11.3 Material and Methods

11.3.1 Patient population

The institutional review board approved the study, with the informed consent of the patients being waived (BE403201526413). Between September 2015 and October 2017, a junior musculoskeletal radiologist with one year of experience collected 8 ONFH specimens from 7 patients (five men (46.4 ±14.5 years [mean ± standard deviation]) and two women (aged 43 and 85 years)). Causes for ON included steroid (n=6), alcohol consumption (n=1) or was

idiopathic (n=1). ON diagnosis was based on radiographs (n=8) obtained at a mean ± SD delay of 49.8 ± 46.3 days before surgery and on MRI (n=4) obtained at 147 ±170.9 days before surgery. There were six ARCO 3-early, one ARCO 3-late, and one ARCO 4 lesions according to the 2019 updated version of ARCO classification (109). Femoral head specimens were fixed in a formalin buffered solution immediately after surgery and were investigated at µCT and MDCT imaging. Histological confirmation was obtained for all the specimens.

11.3.2 Data acquisition

The eight FH were scanned on a clinical 40-row multidetector CT scanner (Siemens Somatom Definition 40). A single tube spiral acquisition was performed using the following parameters: 120 kV, 200 effective mAs, 1-sec rotation speed, pitch factor: 0.35, number of detector rows: 40, collimation: 40 × 0.6 mm. The Siemens z-UHR scan mode was applied. After scanning in a helical mode with a 400 µm slice thickness, images were reconstructed at 200 µm slice-spacing with an image matrix of 512x512 using a normal cone-beam method and a U70u kernel achieving high structural resolution. Using ultra-high-resolution mode, this MDCT scanner can achieve xy-plane 10% modulation transfer function (MTF) of 24.8 lp/cm corresponding to about 201.6 µm in-plane resolution and z-plane 10% MTF of 21.0 lp/cm corresponding to about 238.1 µm z-plane resolution. The eight femoral heads were scanned using a µCT scanner (SkyScan 1173 microtomograph, Bruker Company, Kontich, Belgium) at a nominal resolution of 52 µm (130 kV; Brass filter; no pixel binning; scan orbit 360°; rotation step 0.25°; voxel volume: 1.25 10^{-7} ml; duration: 50 minutes)(145). Raw data reconstruction was carried out with a modified Feldkamp algorithm (128) using the SkyScanTM NRecon software accelerated by a Graphics Processing Unit (GPU) (129). Data were anonymized and stored in a DICOM on an external hard disk. Specimen blocks harvested from these 8 FH were further imaged at 12 µm spatial resolution and findings were correlated with histology (step II).

11.3.3 Image segmentation

The same radiologist viewed the µCT and MDCT data of each FH specimen on a commercially available image viewer with multiplanar capacity. All specimens were viewed as right femoral heads and reformats were obtained using the following landmarks: the fovea, the center of the femoral head using a best-fitting circle on the mid coronal image, two perpendicular lines passing through the center of the femoral head. For every femoral head, image contrast was manually adjusted to enable optimal bone visualization. Matched coronal

(n=90) and sagittal (n=89) µCT and MDCT reformats were obtained at a 4 mm interslice gap. The 180 coronal and 178 sagittal MDCT and µCT reformats were stored in a bitmap format with a 4-mm scale bar inserted in each image. Reformats were segmented by overlaying a transparent 12 x 12 grid and were identically magnified so that the 4 mm scale bar corresponded to one grid box. The center of the femoral head was positioned in the center of the grid, the horizontal and vertical axes were used for image orientation so that each grid box contained the same areas of the matched µCT and MDCT reformats (Figure 18,19). The anonymized images with the superposed grid were uploaded on an in-house developed software that enabled automated data generation on Excel sheets. Grid boxes containing the femoral neck or the fovea and those with surgery-related artifacts were excluded.

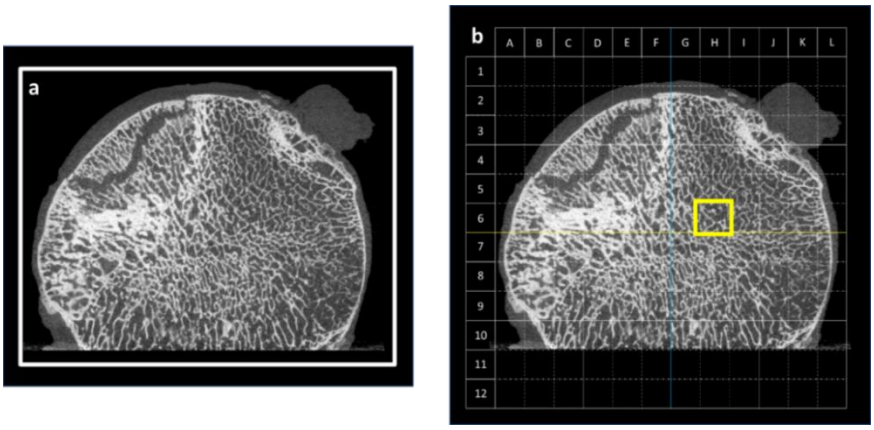

Figure 18: Coronal µCT reformat of an osteonecrotic femoral head without (a) and with (b) grid overlaying. Each grid box was analyzed for the presence or absence of defined bone changes including microfractures, sclerosis and resorption. The highlighted H6 grid box contains normal trabecular bone. The same process was performed for MDCT reformats (not shown).

11.3.4 Image analysis

Between January and March 2020, images were independently analyzed in by an MSK radiologist with 30 years of experience (R1) and an MSK radiologist with five years of experience (R2) who previously prepared the images. Both readers (R1 and R2) were familiar with in vitro µCT and MDCT imaging.

Bone changes at MDCT were defined as follows (Figure 19Figure 20): Interface-related trabecular bone sclerosis corresponded to thickened trabeculae with a band-like distribution and a concave orientation towards the articular surface. Grid boxes containing the necrotic lesion were those containing the

sclerotic interface and those situated between the interface and the epiphyseal surface. Cortical bone interruption corresponded to a focal interruption of the subchondral cortical bone plate with or without a focal deformity (Figure 19, 20). Trabecular bone interruption corresponded to an interruption of two or more contiguous trabeculae, having irregular, sharp, or angular margins with or without a gas-filled cleft or a dense linear band corresponding to trabecular crushing (Figure 19, 20). Trabecular bone resorption corresponded to a lucent zone devoid of mineralized content, with smooth or rounded margins that developed within the necrotic lesion (Figure 19, 20). Segments with trabecular resorption should contain at least 25% of the surface area to be counted as positive, to avoid overestimating the volume of resorption. Trabecular osteopenia located at distance from the necrotic lesion in the non-weight-bearing areas of the femoral head was not considered to represent trabecular bone resorption.

Each image was displayed in four copies to enable a separate analysis of the four bone changes in every grid box. The readers analyzed the image and clicked on the grid box that contained the bone change. Readings were automatically transferred in an excel sheet. In September 2020, a second reading of 34 coronal reformats and 24 sagittal reformats was performed separately by both readers to assess intra-observer reproducibility.

11.3.5 Consensus reading of µCT images

After completion of separate image analysis, grid boxes with identical findings between R1 and R2 at initial reading of µCT reformats were adjudicated as true positive or true negative for each bone change. Grid boxes with discrepant results for the presence or absence of bone changes at first reading were reassessed three months later to resolve discrepancies by consensus. Both readers were blinded to their initial findings.

11.3.6 Statistical analysis

For R1 and R2, the sensitivity and specificity of MDCT to detect bone changes in 4x4 mm grid boxes were compared to consensus reading at µCT in the sagittal and coronal planes separately. The area under the curve (AUC) of both readers was obtained by using ROC curve statistics (159). Interobserver agreement and intra-observer reproducibility were obtained using Cohen's Kappa and interpreted with a conservative approach using the lower confidence interval, according to the scale proposed by Altman (151). A p-value < 0.05 was regarded as statistically significant. Statistical analyses were performed using Medcalc statistical software (Version 20.009, https://www.medcalc.org/, Belgium).

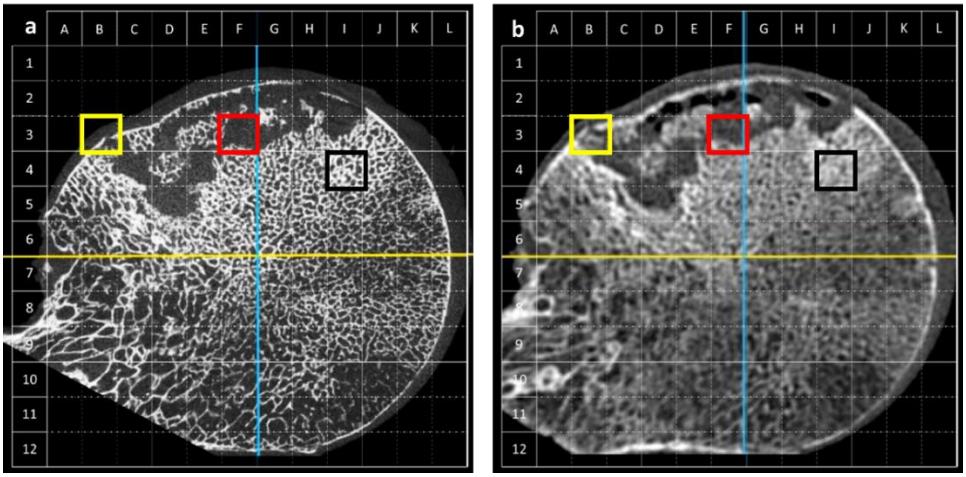

Figure 19: Corresponding (a) µCT and (b) MDCT coronal reformats of an osteonecrotic femoral head. A cortical bone microfracture is visible in both B3 grid boxes highlighted in yellow. Bone resorption is visible in both F3 highlighted in red. Bone sclerosis is visible in both I4 (highlighted in black).

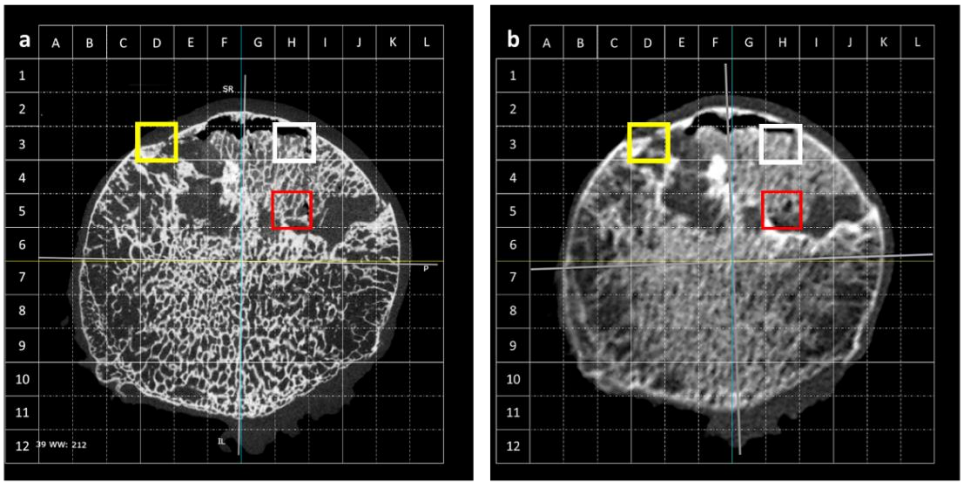

Figure 20:Corresponding (a) µCT and (b) MDCT sagittal reformats of an osteonecrotic femoral head. A cortical bone microfracture is visible in both D3 grid boxes highlighted in yellow. The trabecular microfracture seen at µCT (H5, highlighted in red) is not visible at MDCT (H5) whereas the trabecular microfracture in H3 (highlighted in white) is visible on both techniques.

11.4 Results

11.4.1 Diagnostic performance of MDCT in comparison with µCT for the detection of CRBC

There were 2491 grid boxes containing cortical bone and 11234 containing trabecular bone at µCT and MDCT. Findings at consensus µCT are given in Table 11 and 12. In comparison to µCT, the sensitivity/specificity of R1 on coronal MDCT reformats were 62.9%/92.4% for the detection of cortical bone interruption, 56.2%/97.0% for the detection of trabecular interruption, 48.6%/94.1% for the detection of trabecular impaction, and 39.1%/98.7% for the detection of trabecular resorption. The diagnostic performance of R1 on sagittal MDCT reformats and of R2 on coronal and sagittal MDCT reformats are given in Table 11 and 12.

Table 11: ROC curve analysis for R1 and R2 to detect bone changes at MDCT compared to consensus reading at µCT on matched MDCT and µCT grid boxes on coronal reformats.

	µCT	**MDCT**							
	consensus	**R1**				**R2**			
			Se	**Sp**	**AUC**		**Se**	**Sp**	**AUC**
Cortical microfracture	291/1228 (23.7%)	254/1228 (20.7%)	62.9%	92.4%	0.777	199/1228 (16.2%)	55%	95.8%	0.754
Trabecular microfracture	438/5623 (7.8%)	407/5623 (7.2%)	56.2%	97%	0.766	348/5623 (6.2%)	56.2%	98.1%	0.771
Trabecular Sclerosis	710/5623 (12.6%)	634/5623 (11.3%)	48.6%	94.1%	0.714	767/5623 (13.6%)	62.5%	93.4%	0.760
Trabecular Resorption	425/5623 (7.6%)	234/5623 (4.2%)	39.1%	98.7%	0.689	373/5623 (6.6%)	63.1%	98%	0.805

Table 12: ROC curve analysis for R1 and R2 to detect bone changes at MDCT compared to consensus reading at µCT on matched MDCT and µCT grid boxes on sagittal reformats.

	µCT	**MDCT**							
	consensus	**R1**				**R2**			
			Se	**Sp**	**AUC**		**Se**	**Sp**	**AUC**
Cortical microfracture	271/1263 (21.5%)	269/1263 (21.3%)	59.8%	89.4%	0.746	189/1263 (15%)	49.8%	94.7%	0.722
Trabecular microfracture	521/5611 (9.3%)	465/5611 (8.3%)	52.6%	96.4%	0.745	364/5611 (6.5%)	50.1%	98%	0.741
Trabecular Sclerosis	697/5611 (12.4%)	632/5611 (11.3%)	46.9%	93.8%	0.704	639/5611 (11.4%)	52.9%	94.5%	0.737
Trabecular Resorption	353/5611 (6.3%)	266/5611 (4.7%)	47.6%	98.1%	0.729	387/5611 (6.9%)	55.2%	96.4%	0.758

11.4.2 Inter- and intra-observer reproducibility for the detection of CRBC

There were 2135/1616 grid boxes with trabecular bone in the coronal and sagittal planes respectively and 562/400 grid boxes that contained cortical bone. Inter-observer agreement for reading of coronal MDCT reformats was at least good

for cortical (Kappa ≥0.64) and trabecular interruption (Kappa ≥0.67). It was at least moderate for trabecular sclerosis (Kappa ≥0.57) and resorption (Kappa ≥0.54). Further details are provided in Table 13.

Table 13:Inter- and intra- observer agreement to detect bone changes at MDCT. Numbers correspond to Cohen's Kappa with 95% confidence intervals given in brackets.

	Interobserver		**Intra-observer**			
	Coronal	**Sagittal**	**Coronal**		**Sagittal**	
			R1	**R2**	**R1**	**R2**
Cortical interruption	0.7005 [0.6474-0.7536]	0.6347 [0.5772-0.6922]	0.7073 [0.6346-0.78]	0.6738 [0.5824-0.7625]	0.8086 [0.7415-0.8757]	0.7884 [0.7156-0.8612]
Trabecular interruption	0.7091 [0.67-0.7482]	0.7593 [0.7252-0.7934]	0.6986 [0.644-0.7532]	0.7836 [0.7296-0.8376]	0.7483 [0.6983-0.7983]	0.8754 [0.8333-0.9175]
Trabecular Sclerosis	0.6051 [0.5715-0.6387]	0.5839 [0.4578-0.62]	0.7121 [0.6604-0.7638]	0.7653 [0.722-0.8086]	0.5534 [0.4755-0.6313]	0.5878 [0.5152-0.6604]
Trabecular Resorption	0.5989 [0.5483-0.6495]	0.6739 [0.6296-0.7182]	0.6707 [0.5625-0.7789]	0.7991 [0.741-0.8572]	0.4473 [0.2949-0.5997]	0.7769 [0.6821-0.8717]

11.5 Discussion

In the current study, we demonstrated that MDCT had high specificity but limited sensitivity to detect cortical and trabecular microfractures, sclerosis, and resorption in comparison with µCT.

First, the high specificity of MDCT to detect bone interruption is reminiscent of previous studies addressing the clinical value of MDCT to detect radiographically occult fractures (160-162). Most likely, the interruption or deformity of highly attenuating cortical or trabecular lines are very conspicuous at MDCT images that display bone with high contrast to noise ratio.

Second, the limited sensitivity of MDCT to detect cortical and trabecular microfractures could be inherent to its lower spatial resolution than that of µCT. Actually, in the current study, the spatial resolution of MDCT images was ~5 times lower than that of µCT. This limited sensitivity obtained by performing a segment-by-segment analysis should be further assessed in the whole ONFH on a head-by-head analysis. MDCT could have a higher sensitivity for fracture detection in whole femoral heads than in segments.

In the current study, the grid overlay method was based on the segmentation of sets of identical µCT and MDCT images and yielded a high number of matched µCT and MDCT grid boxes. Previous studies addressed histomorphological changes at µCT in ONFH (163-166). To the best of our knowledge, no previous studies addressed morphologic parameters including bone interruptions and bone resorption in FHON at µCT and MDCT.

Our study has several limitations. First, only eight resected ONFH specimens were included. Second, while performing analysis in a grid box, the reader could have been influenced by the findings in the adjacent grid boxes. This contrast effect bias could not be avoided. Third, our standard of reference was µCT and microscopic analysis of the whole specimen was not performed. In a previous paper, we demonstrated that µCT was accurate to detect microfractures in comparison with histology (158) (Step II). Neither did we obtain quantitative histomorphometric parameters at MDCT and µCT as in previous *in vitro* studies (163-166). Fourth, image processing and segmentation were manually performed with a possible mismatch between MDCT and µCT reformats; this could have been avoided by using automated software for image registration. Finally, the radiologist who performed image processing also read the images with a possible recall bias. To avoid this, reading was performed six months after image processing.

In conclusion, MDCT has a high specificity and limited sensitivity to detect cortical and trabecular bone changes in osteonecrotic femoral head specimens in 4 mm grid boxes in comparison with µCT.

12 STEP IV: Collapse-related bone changes in ONFH at MDCT: comparison between femoral heads with limited and advanced collapse

Collaborators: Souad Acid MD, Anthony Awad and Nicolas Michoux

12.1 Highlights

- Cortical and trabecular bone interruption and bone resorption are frequently observed at MDCT reformats of collapsed ONFH.
- The distribution of grid boxes with CRBC parallels that of those with necrotic lesion and involve more frequently the anterior, central, and superior quadrants of the FH.
- The frequency of grid boxes with cortical interruption and trabecular resorption is significantly higher in ONFH with advanced than with limited collapse.
- The frequency of grid boxes with trabecular interruption and interface-related trabecular sclerosis is not significantly different between ONFH with limited or advanced collapse.

12.2 Introduction

The occurrence of collapse in ONFH is a pivotal step towards OA and subsequent total hip replacement. The detection of collapse relies on conventional radiography and MRI (110). More recently, MDCT has been shown to be superior to MRI and radiographs in the detection of subchondral fractures (109, 118, 119). In fact, MDCT imaging yields high spatial and contrast resolution for bone imaging by obtaining a nearly isotropic volume of acquisition and demonstrates femoral head deformity corresponding to cortical bone fractures, and trabecular lucencies corresponding to trabecular bone fractures or resorption (118, 121). There is a need to better understand bone changes associated with progressive collapse. This study aimed to determine the frequency and topology of bone changes in a quantitative analysis performed on MDCT images of resected ONFH specimens using the grid overlay method and to compare their frequency between femoral heads with limited or advanced collapse.

12.3 Material and Methods

12.3.1 Patients' population

The institutional review board approved the study, with the informed consent of the patients being waived (BE403201526413). Between September 2015 and October 2017, a junior musculoskeletal radiologist with 4 years of experience collected 14 FH specimens with ON from 13 patients: 8 men (46.9 ±13.9 years [mean age ± standard deviation]) and 5 women (68.4 ±16.05 years) resected for THR. The cause of osteonecrosis was related to alcohol overconsumption (n=4), steroids (n=8), and was considered idiopathic in 2 patients. The FH specimens were immediately fixed in a formalin buffered solution.

12.3.2 Staging of ONFH and measurement of articular surface collapse

Staging of ONFH was performed by the junior radiologist on radiographs (n=11) obtained at a median time interval before surgery of 46 days [7-78 days, 95% CI] or on MRI examination (n=8) obtained at a median time interval before surgery of 61.5 days [11-132 days, 95% CI]. Staging was performed according to the 2019 updated version of the Association Research Osseous Circulation (ARCO) classification (109). The collapse of the articular surface was measured on anteroposterior and frog-leg lateral radiographs (n=11) or MR images (n=3) obtained 1, 11, and 28 days before surgery. The technique of the best fitting concentric circle was used to measure articular collapse, and the highest measurements were retained for final analysis (167). The median collapse was 1.5 mm [1.1-2.1 mm, 95% confidence interval]. There were 10 stage 3-A, 3 stage 3-B, and 1 stage 4 ONFH.

12.3.3 Data acquisition and grid overlying

Fourteen resected FH specimens were scanned on a clinical 40-row multidetector CT scanner (Siemens Somatom Definition 40). One radiologist with four years of experience viewed the MDCT images of each FH specimen on a commercially available image viewer with multiplanar capacity. Coronal reformats were obtained and segmented by overlaying a transparent 12 x 12 grid. The anonymized images with the overlayed grid were uploaded on an in-house developed software that enables image analysis, and the output is saved into a spreadsheet-compatible file suitable for further statistical analysis (Figure 21).

12.3.4 Image analysis and lesion definition

Between March and May 2020, images were independently analyzed by an MSK radiologist with 30 years of experience (R1), and an MSK radiologist with four years of experience (R2) who previously prepared the images. The reading process was performed in 4x4 mm grid boxes using the grid overlay method on in-house developed software.

Bone changes at MDCT were defined as follows: Interface-related trabecular bone sclerosis corresponded to thickened trabeculae with a band-like distribution and a concave orientation towards the articular surface. Grid boxes containing the necrotic lesion were those containing the sclerotic interface and those situated between the interface and the epiphyseal surface. Cortical bone interruption corresponded to a focal interruption of the subchondral cortical bone plate with or without a focal deformity (Figure 22). Trabecular bone interruption corresponded to an interruption of two or more contiguous trabeculae, having irregular, sharp, or angular margins with or without a gas-filled cleft or a dense linear band corresponding to trabecular crushing (Figure 22,23). Trabecular bone resorption corresponded to a lucent zone devoid of mineralized content, with smooth or rounded margins that developed within the necrotic lesion (Figure 22).

Limited FH collapse was defined by the presence of depression of the FH contours inferior to 1.5 mm. Advanced FH collapse was defined by the presence of a depression ≥ 1.5mm.

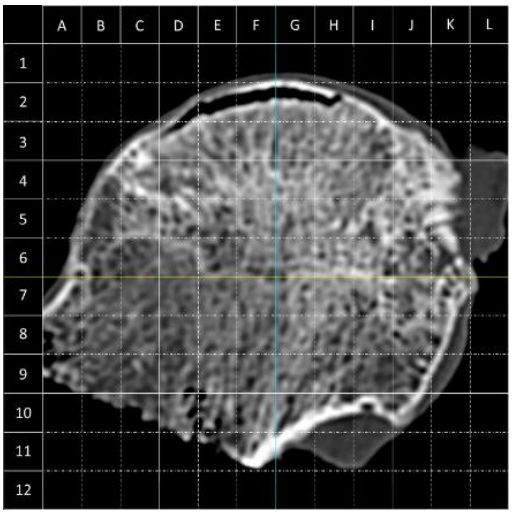

Figure 21: A 12x12 grid was overlayed on coronal MDCT reformats. Image analysis was performed in every 4x4 mm grid box. As an example, D2, D3, E2, F2, G2, and H2 contained collapse-related trabecular interruption

12.3.5 Statistical analysis

Data output was automatically generated on Excel sheets. The normality of the population was assessed using the Shapiro-Wilk test and the equality of variance using the F test. For R1 and R2, the frequency of grid boxes with bone changes was compared between FH with limited and advanced collapse using Chi-squared test. Interobserver agreement was computed using Cohen's Kappa. A *p*-value < 0.05 was regarded as statistically significant for all tests cited above. Statistical analyses were performed using Medcalc statistical software (Version 20.009, https://www.medcalc.org/, Belgium).

12.4 Results

12.4.1 Frequency of grid boxes with bone changes at MDCT

There were 2933 grid boxes containing cortical bone and 10596 grid boxes containing trabecular bone on the MDCT reformats obtained in 14 ONFH specimens. For R1, there were 3442/10596 (32.5%) grid boxes with necrotic lesion, 1111/10596 (10.5%) with interface-related trabecular sclerosis, 557/2933 (19%) with cortical bone interruption, 796/10596 (7.5%) with trabecular bone interruption, and 331/10596 (3.1%) with trabecular bone resorption. Results for R2 are provided in Table 14.

Table 14: Frequency of grid boxes with cortical and trabecular bone changes on coronal MDCT reformats

		R1	R2
Necrosis-related bone changes	**Necrotic lesion**	3442/10596 (32.5%)	3666/10596 (34.6%)
	Trabecular sclerosis	1111/10596 (10.5%)	1362/10596 (12.9%)
Collapse-related bone changes	**Cortical interruption**	557/2933 (19%)	413/2933 (14.1%)
	Trabecular interruption	796/10596 (7.5%)	665/10596 (6.3%)
	Trabecular resorption	331/10596 (3.1%)	595/10596 (5.6%)

R1 and R2 represent two readers. R1=senior radiologist, R2=junior radiologist

12.4.2 Topology of grid boxes with necrotic lesion and CRBC at MDCT

For R1, grid boxes with necrotic lesions, interface-related sclerosis, or with CRBC at MDCT were more frequent in the anterior than in the posterior two thirds ($p<0.01$), in the central than in the medial or lateral thirds ($p<0.02$), and in the superior third than in the two lower thirds ($p<0.01$) of the FH (Table 16). Grid boxes with trabecular interruption were more frequent in the superficial (448/2621; 17.1%) than in the deep layer (348/7975; 4.4%) ($p<0.01$). Grid boxes with trabecular resorption were more frequent in the deep (281/7975; 3.5%) than in the superficial layer (50/2621; 1.9%). Detailed results for R1 and R2 are provided in. For R1, grid boxes with cortical and trabecular bone changes were more frequent within than outside the necrotic lesion ($p<0.01$). Detailed results for R1 and R2 are provided in Table 15.

Table 15: Comparison of frequency of grid boxes with CRBC on coronal MDCT reformats within or outside the osteonecrotic lesions.*

	Collapse-related bone changes	Outside necrotic lesion	Within necrotic lesion	P value
R1	**Cortical bone interruption**	42/1507 (2.8%)	415/979 (42.4%)	p<0.001
	Trabecular bone interruption	18/6182 (0.3%)	648/2750 (23.6%)	p<0.001
	Trabecular bone resorption	20/6182 (0.3%)	246/2750 (8.9%)	p<0.001
R2	**Cortical bone interruption**	24/1507 (1.6%)	315/979 (32.2%)	p<0.001
	Trabecular bone interruption	3/6118 (0.05%)	544/2814 (19.3%)	p<0.001
	Trabecular bone resorption	3/6118 (0.05%)	519/2814 (18.4%)	p<0.001

**Frequency of grid boxes containing the necrotic lesion was calculated in 12 instead of 14 ONFH because the interface was only partially visible.*

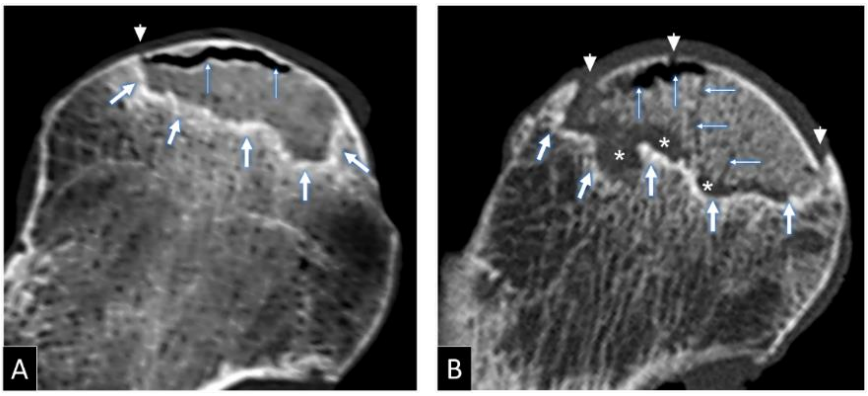

Figure 22: Coronal MDCT reformats of resected femoral head specimens of (A) a 59-yo woman and (B) an 85-yo woman, showing interface-related bone sclerosis (thick arrows) and collapse-related bone changes: cortical interruption (arrowheads), trabecular interruption (thin arrows) and bone resorption (asterisks in B).

Table 16: Frequency of grid boxes with collapse-related bone changes and with necrotic lesion in different thirds regions of the FH in the coronal plane on MDCT reformats.

		Antero-posterior direction				Medio-lateral direction				Cranio-caudal direction				Radial direction		
		Ant	**Mid**	**Post**	**P**	**Med**	**Cent**	**Lat**	**P**	**Sup**	**Mid**	**Inf**	**P**	**Superficial**	**Deep**	**P**
R1	**Necrotic Lesion***	782/2159 (36.2%)	1345/4354 (30.9%)	623/2419 (25.8%)	$P^1<0.001$ $P^2<0.001$ $P^3<0.001$	681/2427 (28.1%)	1582/4345 (36.4%)	487/2160 (22.5%)	$P^4<0.001$ $P^5<0.001$ $P^6<0.001$	1713/2273 (75.4%)	1030/4632 (22.2%)	7/2027 (0.3%)	$P^7<0.001$ $P^8<0.001$ $P^9<0.001$	823/2232 (36.9%)	1927/6700 (28.8%)	P<0.001
	Trabecular sclerosis	324/2562 (12.6%)	509/5134 (9.9%)	278/2900 (9.6%)	$P^1<0.001$ $P^2<0.001$ $P^3=0.664$	273/2867 (9.5%)	587/5125 (11.45%)	251/2604 (9.6%)	$P^4=0.007$ $P^5=0.090$ $P^6=0.013$	422/2671 (15.8%)	650/5447 (11.9%)	39/2478 (1.6%)	$P^7<0.001$ $P^8<0.001$ $P^9<0.001$	203/2621 (7.7%)	908/7975 (11.4%)	P<0.001
	Cortical interruption	213/830 (25.7%)	236/1199 (19.7%)	108/904 (11.9%)	$P^1=0.001$ $P^2<0.001$ $P^3<0.001$	131/1357 (6.7%)	252/846 (29.8%)	174/730 (23.8%)	$P^4<0.001$ $P^5<0.001$ $P^6=0.007$	486/1388 (35%)	71/941 (7.5%)	0/604 (0%)	$P^7<0.001$ $P^8<0.001$ $P^9<0.001$	NA	NA	
	Trabecular interruption	243/2562 (9.5%)	404/5134 (7.9%)	149/2900 (5.1%)	$P^1=0.02$ $P^2<0.001$ $P^3<0.001$	160/2867 (5.6%)	448/5125 (8.7%)	188/2604 (7.2%)	$P^4<0.001$ $P^5=0.016$ $P^6=0.023$	693/2671 (25.9%)	99/5447 (1.8%)	4/2478 (0.2%)	$P^7<0.001$ $P^8<0.001$ $P^9<0.001$	448/2621 (17.1%)	348/7975 (4.4%)	P<0.001
	Trabecular resorption	162/2562 (6.3%)	125/5134 (2.4%)	44/2900 (1.5%)	$P^1<0.001$ $P^2<0.001$ $P^3=0.007$	59/2867 (2.1%)	204/5125 (4%)	68/2604 (2.6%)	$P^4<0.001$ $P^5=0.221$ $P^6=0.002$	171/2671 (6.4%)	143/5447 (2.6%)	17/2478 (0.7%)	$P^7<0.001$ $P^8<0.001$ $P^9<0.001$	50/2621 (1.9%)	281/7975 (3.5%)	P<0.001
R2	**Necrotic Lesion***	884/2159 (40.9%)	1323/4354 (30.4%)	607/2419 (25.1%)	$P^1<0.001$ $P^2<0.001$ $P^3<0.001$	685/2427 (28.2%)	1585/4345 (36.5%)	544/2160 (25.2%)	$P^4<0.001$ $P^5=0.022$ $P^6<0.001$	1766/2273 (77.7%)	1036/4632 (22.4%)	12/2027 (0.6%)	$P^7<0.001$ $P^8<0.001$ $P^9<0.001$	897/2232 (40.2%)	1917/6700 (28.6%)	P<0.001
	Trabecular sclerosis	421/2562 (16.4%)	616/5134 (12%)	325/2900 (11.2%)	$P^1<0.001$ $P^2<0.001$ $P^3=0.284$	332/2867 (11.6%)	662/5125 (12.9%)	368/2604 (14.1%)	$P^4=0.091$ $P^5=.006$ $P^6=.014$	590/2671 (22.1%)	732/5447 (13.4%)	40/2478 (1.6%)	$P^x<0.001$ $P^y<0.001$ $P^z<0.001$	317/2621 (12.1%)	1045/7975 (13.1%)	P=0.185
	Cortical interruption	168/830 (20.2%)	179/1199 (14.9%)	66/904 (7.3%)	$P^1=0.002$ $P^2<0.001$ $P^3<0.001$	112/1357 (8.3%)	186/846 (22%)	115/730 (15.75%)	$P^4<0.001$ $P^5<0.001$ $P^6=0.002$	350/1388 (25.2%)	60/941 (6.4%)	3/604 (0.5%)	$P^7<0.001$ $P^8<0.001$ $P^9<0.001$	NA	NA	
	Trabecular interruption	228/2562 (8.9%)	306/5134 (6%)	131/2900 (4.5%)	$P^1<0.001$ $P^2<0.001$ $P^3=0.004$	108/2867 (3.8%)	432/5125 (8.4%)	125/2604 (4.8%)	$P^4<0.001$ $P^5=0.068$ $P^6<0.001$	582/2671 (21.8%)	83/5447 (1.5%)	0/2478 (0%)	$P^7<0.001$ $P^8<0.001$ $P^9<0.001$	389/2621 (14.8%)	276/7975 (3.5%)	P<0.001
	Trabecular resorption	243/2562 (9.5%)	248/5134 (4.8%)	104/2900 (3.6%)	$P^1<0.001$ $P^2<0.001$ $P^3=0.011$	116/2867 (4.1%)	334/5125 (6.5%)	145/2604 (5.6%)	$P^4<.001$ $P^5=0.01$ $P^6=0.12$	353/2671 (13.2%)	238/5447 (4.4%)	4/2478 (0.2%)	$P^7<0.001$ $P^8<0.001$ $P^9<0.001$	110/2621 (4.2%)	485/7975 (6.1%)	P<0.001

**Frequency of grid boxes containing the necrotic lesion was calculated in 12 instead of 14 ONFH because the interface was only partially visible. The denominators represent the total number of grid boxes in every region. (p^1) Anterior versus Middle; (p^2) Anterior versus Posterior; (p^3) Middle versus posterior. (p^4) = Medial versus Central; (p^5) = Medial versus Lateral; (p^6) = Central versus Lateral. (p^7) = Superior versus Middle; (p^8)= Superior versus Inferior; (p^9)= Middle versus inferior.*

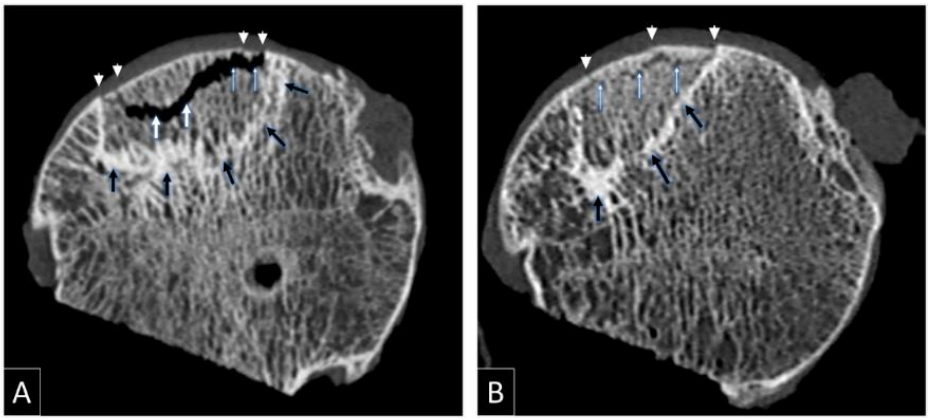

Figure 23: (A) and (B) Coronal MDCT reformats of a resected femoral head specimen in a 62 yo man, showing collapse-related trabecular interruption in the superficial (thin white arrows) and deep layers (thick white arrows) of the trabecular bone. Also, note cortical interruption (arrowheads) and interface-related bone sclerosis (black arrows)

12.4.3 Comparison of frequency of grid boxes with necrotic lesions and CRBC at MDCT between limited and advance collapse

For R1, there was no difference in the frequency of grid boxes with necrotic lesion between FH with collapse ≥1.5mm (32.76%) than <1.5 mm (32.13%) (p=0.50). There was no difference in the frequency of grid boxes with interface-related bone sclerosis between FH with collapse ≥1.5mm (10.22%) than <1.5 mm (10.82%) (p=0.32). Grid boxes with cortical interruption were more frequent in FH with collapse ≥1.5mm (20.49%) than in FH with collapse<1.5 mm (17.02%) (p=0.018). There was no difference in the frequency of grid boxes with trabecular interruption between FH with collapse ≥1.5mm (7.13%) than <1.5 mm (8%) (p=0.09). Grid boxes with trabecular resorption were more frequent in FH with collapse ≥1.5mm (3.88%) than <1.5 mm (2.15%) (p<0.01). Detailed results for R1 and R2 are provided in Table 17

Table 17: Comparison of frequency of grid boxes with necrotic lesions and CRBC at MDCT between ONFH with limited and advanced collapse.

	R1			R2		
Frequency of grid boxes containing	**Collapse <1.5 mm**	**Collapse ≥1.5 mm**	**P value**	**Collapse <1.5 mm**	**Collapse ≥1.5 mm**	**P value**
necrotic lesion	1481/4610 (32.13%)	1961/5986 (32.76%)	P=0.50	1460/4610 (31.67%)	2206/5986 (36.85%)	p<0.001
interface-related Trabecular sclerosis	499/4610 (10.82%)	612/5986 (10.22%)	P=0.32	577/4610 (12.51%)	785/5986 (13.11%)	P=0.36
cortical bone interruption	216/1269 (17.02%)	341/1664 (20.49%)	P=0.02	121/1269 (9.54%)	292/1664 (17.55%)	p<0.001
trabecular bone interruption	369/4610 (8%)	427/5986 (7.13%)	P=0.09	299/4610 (6.49%)	366/5986 (6.11%)	P=0.44
trabecular bone resorption	99/4610 (2.15%)	232/5986 (3.88%)	p<0.001	214/4610 (4.64%)	381/5986 (6.36%)	p<0.001

12.5 Discussion

In the current study, we assessed bone changes in ONFH specimens using MDCT and found that grid boxes with necrotic lesion and CRBC predominated in the anterior, central, and superior parts of ONFH specimens. We also found that grid boxes with cortical interruption and trabecular bone resorption were more frequent in femoral heads with advanced collapse than in those with limited collapse, with no difference in frequency of bone interruption according to the degree of collapse. These observations suggest that progression of collapse could be more associated with the development of cortical bone fracture and bone resorption than with trabecular bone interruption.

First, we demonstrated that CRBC at MDCT almost exclusively involved the necrotic lesions and subsequently their topology paralleled that of the necrotic lesion. Previous studies demonstrated that the necrotic lesion involved more frequently the anterior, central, and upper thirds of the femoral head most likely due to the vascular anatomy and stress distribution in the femoral head (13, 168). The observation that trabecular bone interruption predominated in the superficial layer of the necrotic lesion could be explained by the concentration of mechanical stress on the surface or by its association with cortical interruption (14, 16, 97, 140, 143). The predominance of trabecular bone resorption in the deep regions of the necrotic lesions is well in line with its association with the repair process that includes increased bone remodeling in vascularized regions surrounding and invading the lesion (15, 16).

Second, CRBC at MDCT were all observed at variable frequencies in the collapsed ONFH regardless of the degree of collapse and without any bone changes observed exclusively in limited or advanced collapse. The fact that cortical bone interruption was more frequent in ONFH with advanced than with limited is well in line with the concept that the collapse is associated with marked deformity of the subchondral bone plate that results from cortical bone interruption. Similarly, the observation that grid boxes with bone resorption were more frequent in ONFH with more advanced collapse suggests that bone resorption could develop during progressive failure of the femoral head and is not associated with early fracture (97, 124).

Third, the lack of difference in frequency of grid boxes with trabecular bone interruption according to the degree of collapse could contradict the general idea that links fracture with collapse. Fracture formation could differ from collapse. Actually, in rocks, crack formation differs from crack propagation and accumulation because the latter are influenced by changes that occur with early crack such as development of fluid-containing micro-fissures (169). In ONFH, stress distribution is altered by progressive collapse, and the development of trabecular fracture can be dissociated from that of cortical fracture (95). The hypothesis that progression of collapse is associated with bone resorption and cortical fracture but not with trabecular bone fracture deserves further analysis. Finally, we also observed that the frequency of grid boxes with interface–related bone sclerosis or with necrotic lesions did not differ according to the degree of collapse indicating that lesions with advanced collapse were not larger than those with limited collapse in our study population.

In the current study, we investigated ONFH specimens using MDCT. We acknowledge that the spatial resolution of in vitro MDCT imaging is higher than that performed in clinical practice. Further studies are needed to correlate in vivo with in vitro MDCT imaging. In addition, since the current guidelines recommend MRI and radiographs for staging despite the value of CT for the detection of fracture, the added value of MR-derived CT-like images in the detection of cortical and trabecular bone interruption should be further assessed (170, 171)

Our study has many limitations. First, we studied only a limited number of ONFH specimens with different patient clinical data and etiology. Second, histological confirmation of the findings was not performed. Since µCT can accurately detect cortical and trabecular microfractures in comparison with

histology (145, 158), we obtained μCT examinations in eight of our specimens. We demonstrated that MDCT examinations of ONFH specimens had high specificity in comparison with μCT for the detection of cortical and trabecular bone interruption. Third, femoral head collapse was measured on pre-operative radiographs or MRI obtained at variable time intervals before surgery. We cannot exclude that collapse might have increased meanwhile. In addition, the median value of collapse was selected as a cut-off value to separate femoral head with limited or advanced collapse. The 1.5 mm value was very close to the 2-mm value used in the revised 2019 ARCO classification to differentiate 3-A from 3-B stages. Fourth, although readers were blinded to the importance of epiphyseal collapse at preoperative imaging, they could not be blinded to the presence of altered bone contours when reading the MDCT reformats. Finally, we used a 4-by-4 mm grid overlay method as previously reported in neuroimaging (172). Higher-resolution segmentation could have been obtained by applying a finer grid, at the expense of increased reading time.

In conclusion, cortical and trabecular bone interruption and trabecular bone resorption are found in collapsed ONFH and their distribution parallels that of the necrotic lesions. Grid boxes with cortical bone interruption and trabecular bone resorption but not with trabecular bone interruption are more frequent in ONFH with advanced than with limited collapse.

13 STEP V: Collapse-related bone changes at MDCT in ARCO 1-2 ONFH: correlation with clinical and MRI data

Collaborators: Florent Libert MD, Valérie Gangji MD, Nicolas Michoux

13.1 Highlights

- 98-100% of collapsed and 26-40% of non-collapsed osteonecrotic femoral heads presented at least one CRBC at MDCT (cortical or trabecular bone interruption, trabecular bone impaction or resorption).
- There was no significant difference in age, sex, pain, functional impairment, size of the lesion, or frequency of BME on MRI between non-collapsed hips with or without CRBC at MDCT.
- The significance of CRBC at MDCT should be further assessed

13.2 Introduction

The occurrence of bone changes in ONFH is a pivotal step towards irreversible FH collapse and progression to hip osteoarthritis (92, 173, 174). Medical imaging plays an important role in the diagnosis and staging of osteonecrosis and current recommendations for staging rely on conventional radiography and MRI. MDCT is also recommended before surgical treatment because it can detect subchondral fractures (83, 109, 118-123). The current study aimed to determine the frequency of CRBC by using MDCT in a large series of non-collapsed ONFH and to compare clinical parameters and MRI data between ONFH with and without collapse-related bone changes at MDCT.

13.3 Material and Methods

13.3.1 Study population

We performed a secondary analysis of the imaging findings of the first 100 eligible adult patients of a phase III prospective, multicenter trial assessing the safety and efficacy of a therapy for early FHON. The study protocol (NCT01529008) was approved by the institutional review board of the participating centers. All participants provided fully informed written consent to participate in the clinical trial. A musculoskeletal radiologist with 26 years of experience (BVDB) prospectively analyzed the imaging files of the eligible patients obtained between December 2011 and September 2015 to exclude those

with (a) diagnosis other than osteonecrosis or (b) inadequate imaging data (Figure 24).

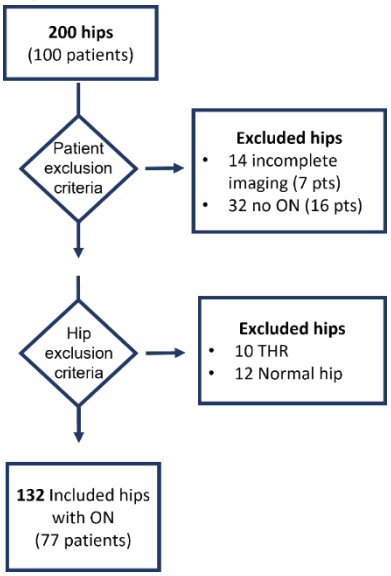

Figure 24: flowchart summarizing the population selection. ON: osteonecrosis; Pts: patients; THR: total hip replacement.

13.3.2 Image data acquisition

Imaging investigations were performed in five participating institutions of four European countries according to the same radiological manual. Conventional radiographs included an anteroposterior (AP) pelvic radiograph, AP and frog-leg lateral radiographs of each hip. MRI was performed on high field (1.5 T or 3T) MRI scanners using a multichannel surface coil. The following sequences were obtained: large field of view (400-500 mm) coronal T1-weighted (TR 400-700 ms, TE 8-20 ms, slice thickness ≤ 4 mm), and T2 weighted SE (TR ≥2500 ms, TE ≥80 ms, slice thickness ≤ 4 mm) images of both hips and high resolution (160-200 mm) sagittal T1-weighted (TR 400-700 ms, TE 8-20 ms, slice thickness ≤ 4 mm) and proton density-fat saturated sequences (TR ≥2500 ms, TE ≥30 ms, slice thickness ≤ 4 mm) of each hip. MDCT was performed on a multidetector scanner with <1mm slice thickness. Image reconstruction was carried out using filtered back projection on the available software to obtain images with sharp and soft kernels. Images were anonymized and stored in a DICOM format on a dedicated research server. Radiographs, MRI, and MDCT examinations were obtained at a median interval of 0 days (mean interval, 3.9 days ± 9.08 [standard deviation]). The pain and functional impairment was obtained using The visual analog Western Ontario and

McMaster Universities Osteoarthritis Index (WOMAC 3.0) scale was used at inclusion for pain and functional impairment evaluation (175). Alcohol consumption and steroid use were noted at inclusion.

13.3.3 Image analysis

In March-April 2016, two final-year residents (CM and FL) referred to as (R1) and (R2) independently analyzed the MDCT images using 1-2 mm multiplanar reformats to detect CRBC. They were blinded to the radiographic and MRI examinations. In July 2016, R1, R2 and BVDB, independently analyzed the radiographic and MRI examinations to stage ONFH. In January 2017, readers held three consensus meetings to reach a final agreement on staging. In March 2017, R1 and R2 analyzed a series of 69 randomly selected MDCT examinations to assess intra-observer reliability. Before the study, R1 and R2 underwent three training sessions with the senior musculoskeletal radiologist on 15 imaging files of patients who were not included in the current analysis.

13.3.4 Lesion definition

Diagnosis of osteonecrosis was based on MRI according to the presence of a wedge-shaped or geographic area with variable signal intensity and surrounded by a low signal intensity rim on T1-weighted images (24, 137).

Staging of osteonecrosis was based on conventional radiographs and MRI according to the 2019-revised Association Research Circulation Osseous (ARCO) classification (109). ARCO 1 is defined as osteonecrosis visible on MRI only. ARCO 2 is defined as osteonecrosis visible on MRI and radiographs, without signs of fracture. ARCO 3 corresponds to osteonecrosis with femoral head fracture and normal joint space. Fracture of the subchondral trabecular bone was defined as a subchondral line with fluid-like signal intensity on fluid-sensitive images or a subchondral lucent line on radiographs. Cortical bone fracture was defined as a loss of normal sphericity of the femoral head. Semi-quantitative measurements of collapse to differentiate 3-A from 3-B lesions were performed by R1 and R2 on radiographs using the method of the best fitting concentric circle (22, 167). ARCO 4 corresponds to collapsed ONFH with joint space narrowing on AP and lateral radiographs.

Semi-quantitative measurement of lesion size was performed prospectively by BVDB on MRI using a modification of the combined necrotic angle method of Kerboul (176). Measurements of the arc of the necrotic portion at the articular surface were performed on the midcoronal and the midsagittal T1 weighted images

and the sum of the two angles was calculated. Bone marrow edema was defined as an ill-delimited marrow area of decreased signal intensity on T1-weighted images and of high signal intensity on fat-saturated fluid-sensitive images.

At MDCT, four bone changes potentially associated with collapse were analyzed. Cortical bone interruption was defined as a focal interruption of the subchondral bone plate (Figure 25, 26). Trabecular bone interruption was defined as a linear lucent area in the subchondral bone of the lesion (Figure 25, 27). Trabecular bone impaction was defined as a thin linear sclerotic line within the necrotic lesion distinct from the reactive interface. (Figure 26). Trabecular bone resorption was defined as >1 mm large lucencies within the lesion (Figure 25-27). Thick or thin sclerotic area surrounding the lesion was considered to represent interface-associated bone changes and was not considered to be associated with collapse.

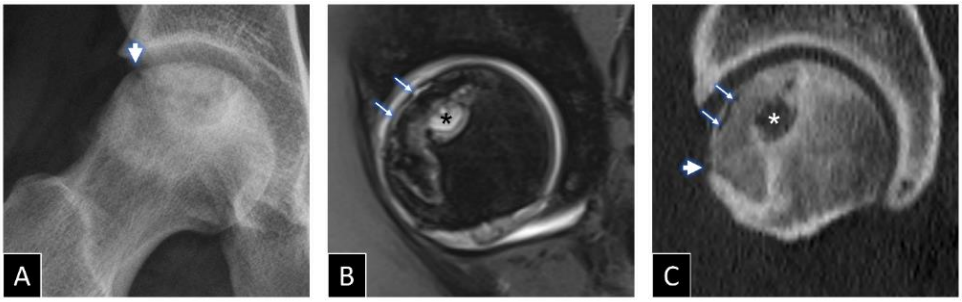

Figure 25: ARCO-3A FHON in a 23 yo woman. (A) Frogleg lateral radiograph shows ON associated structural bone changes of the femoral head with mild collapse of the subchondral bone plate (arrowhead). (B) Sagittal fat-suppressed proton density MRI image shows a subchondral high signal intensity line (arrows) and cyst-like changes (asterisk). (C) Corresponding sagittal MDCT reformat shows collapse-related cortical interruption (arrowhead), trabecular interruption (arrows), and bone resorption (asterisk).

13.3.5 Statistical analysis

For R1 and R2, the frequency of CRBC at MDCT was calculated for each ARCO stage and compared between different groups. Baseline demographic parameters (age, sex), WOMAC score, the mean combined necrotic angle, and the percentage of bone marrow edema were compared between ARCO 1-2 hips with and without collapse-related bone changes at MDCT. The Shapiro-Wilk test was used to assess for normal distribution and the F-test was used to assess for equality of variance. Comparison of proportions (frequency of collapse-related bone changes, sex, frequency of BME) was performed using Fisher Exact test, the

comparison of mean age was performed using Student t-test, and the comparison of medians (WOMAC scale, combined necrotic angle) using two-tailed Mann-Whitney U test. Inter-reader agreement (i.e., reproducibility) and intra-reader agreement (i.e., repeatability) were assessed using Cohen's Kappa. Strength of agreement was interpreted with a conservative approach using the lower bound of the 95%CI (Confidence Interval), according to the scale proposed by Altman: Kappa < 0.2: poor; 0.21 < Kappa < 0.40: fair; 0.41 < Kappa < 0.60: moderate; 0.61 < Kappa < 0.80: good; Kappa > 0.8: very good (151). A *p*-value < 0.05 was regarded as statistically significant for all tests cited above. Statistical analyses were performed using Medcalc statistical software (Version 20.009, https://www.medcalc.org/, Belgium).

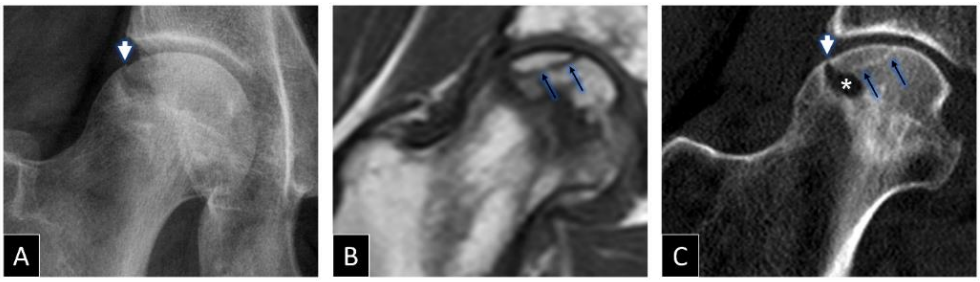

Figure 26: ARCO-3A FHON in a 35 yo man. (A) Anteroposterior radiograph shows ON associated structural bone changes of the femoral head with mild collapse of the subchondral bone plate (arrowhead). (B) Coronal T1-weighted MRI image shows a low T1 line (arrows) within the necrotic territory. (C) Corresponding coronal MDCT reformat shows collapse-related cortical interruption (arrowhead), trabecular impaction (arrows), and bone resorption (asterisk).

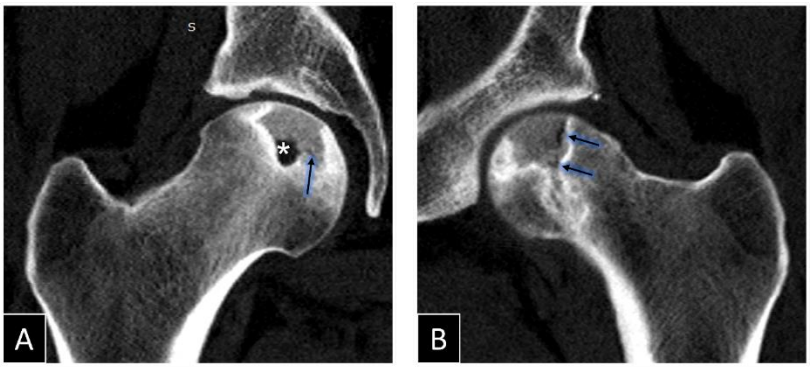

Figure 27: ARCO-2 FHON in a 36 yo man. (A) Coronal MDCT reformats of the right (A) and left (B) hips show collapse-related trabecular interruption (arrowhead) and bone resorption (asterisk).

13.4 Results

13.4.1 Study population

There were 100 eligible study participants (79 males (45.5 ±9.65 years [mean age ± standard deviation] and 21 female (47.2 ±11.54 years) (Table 18). Twenty-three patients were excluded because of other diagnoses (n=16), or inadequate imaging data (n=7), and 77 participants were included (mean age, 45.4 years ±9.53 [standard deviation], 61 male) (Figure 24). One hundred thirty-two ONFH were included after exclusion of hips with total hip arthroplasty (n=10) or normal MRI (n=12) (Figure 24). Clinical and imaging data are summarized in Table 18. There were 78 non-collapsed (39 ARCO 1 and 39 ARCO 2) and 54 collapsed ONFH (32 ARCO 3-A, 13 ARCO 3-B, and 9 ARCO-4). The interobserver variability of the 2019 updated ARCO staging was at least good (weighted Kappa >0.66).

Table 18:Patient clinical data and hip imaging findings according to ARCO 2019 staging

Characteristic	**ARCO 1** n=39	**ARCO 2** n=39	**ARCO 3-A** n=32	**ARCO 3-B** n=13	**ARCO 4** n=9
Male/Female	23/16	36/3	26/6	11/2	7/2
Age (y)	57.4±10.16	47.2±8.67	43.5±10.1	41.9±10.7	43.2±7.3
Etiology Steroids/alcohol/idiopathic	7/3/7	2/1/22	3/1/6	0/0/4	0/0/2
WOMAC (n=83)	43.4±25.6 (n=21)	27.9±21.4 (n=27)	43.7±21.4 (n=23)	49.7±22.3 (n=8)	35.7±29.7 (n=4)
WOMAC pain (n=83)	39.8±24.6 (n=21)	26.4±20.9 (n=27)	37.5±20.3 (n=23)	41.5±19.8 (n=8)	32.9±30.6 (n=4)
Combined necrotic angle	193° ± 94.7°	209.6° ± 84.6°	286.9° ± 62.9°	313.2° ± 96.5°	294.8° ± 63.3°
Bone marrow edema	1 (2.6%)	6 (15.4%)	27 (84.4%)	8 (61.5%)	6 (66.7%)

* Data are mean +/- standard deviation. ARCO = 2019 updated Association Research Circulation Osseous classification(109). WOMAC = Western Ontario and McMaster Universities Osteoarthritis Index
Western Ontario and McMaster Universities Osteoarthritis Index ranges from 0 to 100 mm, with higher scores indicating more severe symptoms. WOMAC includes five subscales: pain (5 items), stiffness (2 items), physical function (17 items) (175). Values indicate the average of the 24 items in millimeters. A hip was considered symptomatic if the average was ≥20 mm.

13.4.2 Frequency of collapse-related bone changes at MDCT in ARCO 1-2 and ARCO 3-4 femoral heads

For R1, the frequency of at least one CRBC at MDCT in ARCO 1-2 ONFH was 31/78 (40%) and was lower than that in ARCO 3-4 ONFH (54/54 (100%)) ($p<0.01$). Trabecular impaction was significantly more frequent in ARCO 1-2, ($p=0.04$) and less frequent in ARCO 3-4 ONFH ($p<0.01$) than trabecular interruption (Figure 28). The frequency of trabecular impaction or interruption was not different from that of bone resorption in ARCO 1-2 and ARCO 3-4 ONFH ($p>0.05$).

For R2, the frequency of at least one CRBC at MDCT in ARCO 1-2 was 20/78 (26%) and was lower than that in ARCO 3-4 (53/54 (98%)) ($p<0.01$) (Table 19). In ARCO 1-2 ONFH, there was no significant difference in frequency of trabecular impaction, interruption, and resorption ($p>0.05$). In ARCO 3-4 ONFH, The frequency of trabecular interruption was higher than that of bone resorption ($p=0.002$) and that of trabecular impaction ($p<0.01$). The frequency of trabecular impaction was not significantly different from that of bone resorption in ARCO 3-4 ONFH ($p=0.23$) (Figure 28).

Table 19:Frequency of CRBC at MDCT in ONFH according to ARCO staging

	CRBC at MDCT	Non-collapsed ONFH (n=78)		Collapsed ONFH (n=54)			
		ARCO 1 (n=39)	ARCO 2 (n=39)	ARCO 3-A (n=32)	ARCO 3-B (n=13)	ARCO 4 (n=9)	P value
R1	Cortical interruption	1 (2.5%)	2 (5.1%)	24 (75%)	12 (92.3%)	8 (88.9%)	p^1 <0.01 p^2 >0.99 p^3<0.01
	Trabecular interruption	2 (5.1%)	8 (20.5%)	26 (81.3%)	13 (100%)	6 (66.7%)	p^1 <0.01 p^2 =0.08 p^3<0.01
	Trabecular Impaction	7 (18%)	12 (30.8%)	20 (62.5%)	10 (76.9%)	4 (44.4%)	p^1 <0.01 p^2 =0.29 p^3<0.01
	Trabecular resorption	5 (12.8%)	11 (28.2%)	22 (68.8%)	10 (76.9%)	8 (88.9%)	p^1 <0.01 p^2 =0.16 p^3<0.01
	At least 1 CRBC	9 (23.1%)	22 (56.4%)	32 (100%)	13 (100%)	9 (100%)	p^1 <0.01 p^2 <0.01 p^3<0.01
	No CRBC	30 (76.9%)	17 (43.6%)	0 (0%)	0 (0%)	0 (0%)	p^1 <0.01 p^2 <0.01 p^3<0.01
R2	Cortical interruption	1 (2.5%)	7 (18%)	27 (84.4%)	13 (100%)	9 (100%)	p^1 <0.01 p^2 =0.06 p^3<0.01
	Trabecular interruption	1 (2.5%)	7 (18%)	28 (87.5%)	13 (100%)	9 (100%)	p^1 <0.01 p^2 =0.06 p^3<0.01
	Trabecular Impaction	2 (5.1%)	5 (12.8%)	17 (53.1%)	9 (69.2%)	4 (44.4%)	p^1 <0.01 p^2 =0.26 p^3<0.01
	Trabecular resorption	2 (5.1%)	7 (18%)	22 (68.8%)	8 (61.5%)	7 (77.8%)	p^1 <0.01 p^2 =0.08 p^3<0.01
	At least 1 CRBC	4 (10.3%)	16 (41%)	31 (96.9%)	13 (100%)	9 (100%)	p^1 <0.01 p^2 =0.03 p^3<0.01
	No CRBC	35 (89.7%)	23 (59%)	1 (3.1%)	0 (0%)	0 (0%)	p^1 <0.01 p^2 <0.01 p^3 <0.01

ARCO = 2019 updated Association Research Circulation Osseous classification(109). CRBC= collapse-related bone changes. **p value : p^1= non-collapsed v/s collapsed; p^2= ARCO 1 v/s ARCO 2; p^3= ARCO 2 v/s ARCO 3-A.*

13.4.3 Comparison of clinical and MRI data between ARCO 1-2 ONFH with or without collapse-related bone changes at MDCT

In ARCO 1-2 hips with at least one CRBC at MDCT, clinical data, mean combined necrotic angle values, and frequency of BME at MRI of hips were not significantly different from those without CRBC ($p>0.05$) (Table 20).

Table 20:Comparison of clinical and baseline imaging findings in ARCO 1-2 ONFH with or without CRBC at MDCT

Clinical and imaging findings	R1			R2		
	MDCT (-)	MDCT (+)	P value	MDCT (-)	MDCT (+)	P value
Male/Female	32/15	27/4	0.057	41/17	18/2	0.08
Age (Mean ± SD)	48.1 ± 9.52	46.2 ± 9.21	0.38	47.9 ± 9.29	45.65 ± 9.72	0.35
WOMAC (Median [95%CI])	24 [17.5-37.9]	38.2 [25.4-54.4]	0.18	33.4 [20.4-42.9]	27 [13.5-50.9]	0.56
WOMAC Pain (Median [95%CI])	22.6 [14.4-27.8]	34.6 [24.6-51]	0.07	27.8 [22-41]	24.6 [6-43.2]	0.69
Baseline combined necrotic angle (Median [95%CI])	196 [147-230]	149 [110-222]	0.53	192.5 [145-216]	151 [108-277]	0.86
Frequency of BME at baseline MRI	3/47 (6.4%)	4/31 (13.6%)	0.32	4/58 (6.9%)	3/20 (15%)	0.27

BME: bone marrow edema; ONFH: osteonecrosis of the femoral head; MDCT: multidetector computed tomography; WOMAC = Western Ontario and McMaster Universities Osteoarthritis Index; MDCT (-): no collapse-related bone changes at MDCT; MDCT (+): at least one collapse-related bone change at MDCT

13.4.4 Inter-observer reproducibility

The interobserver reproducibility on MDCT was at least good to detect cortical interruption (Kappa> 0.74) and trabecular interruption (Kappa> 0.77), at least moderate to detect bone resorption (kappa >0.59) and at least fair to detect trabecular impaction (kappa > 0.27). The intraobserver repeatability is given in Table 21.

Table 21: inter-and intra-observer variability for R1 and R2 to detect CRBC at MDCT.

	Interobserver	Intraobserver	
		R1	R2
Cortical interruption	0.8423 [0.7483-0.9363]	0.7705 [0.6094-0.9316]	0.786 [0.6357-0.9363]
Trabecular interruption	0.8608 [0.773-0.9486]	0.7285 [0.5631-0.8939]	0.8231 [0.6877-0.9585]
Trabecular impaction	0.436 [0.2727-0.5993]	0.4921 [0.2546-0.7296]	0.7421 [0.561-0.9232]
Trabecular resorption	0.7141 [0.5914-0.8351]	0.6809 [0.498-0.8638]	0.6933 [0.5175-0.8691]

Numbers represent weighted Cohen's kappa values with their 95% confidence interval in brackets

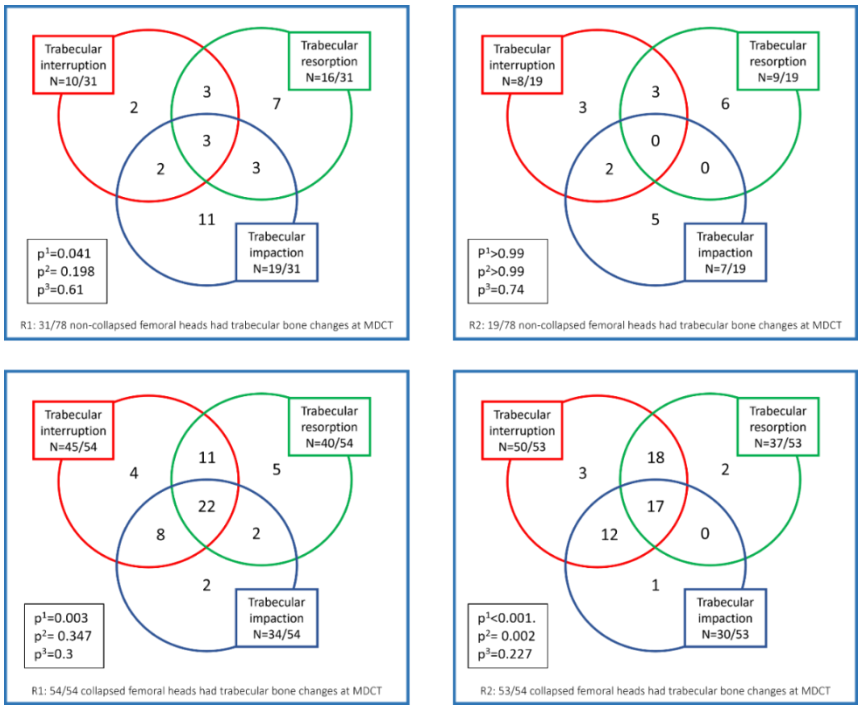

Figure 28: Venn diagrams showing the combinations of CRBC detected on MDCT for R1 and R2 in non-collapsed and collapsed femoral heads with osteonecrosis. For both readers, the frequency of a combination of ≥2 CRBC were significantly higher in collapsed than in non-collapsed femoral heads (p<0.01). p1: trabecular interruption v/s impaction; p2: trabecular interruption v/s resorption; p3: trabecular impaction v/s resorption.

13.5 Discussion

The detection of collapse in ONFH is an important parameter to guide treatment planning and the contribution of CT scan has barely been assessed (25, 92, 109, 118, 119, 173, 174, 177). In the current study, we showed that at least one CRBC was detected at multidetector computed tomography (MDCT) in 98-100% of collapsed ONFH (ARCO 3-4). We also found that at least one collapse-related bone change was detected at MDCT in 26-40% of non-collapsed ONFH (ARCO 1-2), *i.e.*, in ONFH that showed no signs of collapse on MRI and CR. Finally, patient's demographics, pain, functional impairment, lesion size, or the frequency of bone marrow edema at baseline MRI in ARCO 1-2 hips with at least one CRBC at MDCT were not significantly different from those without bone changes.

First, the fact that at least one collapse-related bone change at MDCT was detected in 98-100% of ARCO 3-4 ONFH supports the hypothesis that cortical and

trabecular interruption, as well as trabecular impaction and resorption, are related to FH collapse. In the current study, we used the umbrella term "collapse-related bone changes since there is no unanimous agreement on the definition of fracture in ONFH at MDCT (109). Cortical interruption, trabecular interruption, and trabecular impaction are widely accepted as MDCT signs of fracture (20, 83, 120, 121, 178-181). It is questionable that bone resorption also represents a fracture and the distinction between a fracture-associated lucent line and a resorption-associated lucent zone may be challenging. Whatever its origin, trabecular bone resorption is frequently observed in advanced osteonecrosis (14, 16, 143), and it is conceivable that it is associated with collapse (124).

Second, MDCT detected at least one CRBC in 26-40% of untreated ARCO 1-2 ONFH in which no collapse was seen on radiographic and MRI examinations. Yeh et al and Meier et al observed bone fractures at MDCT in 25-45% and 100% of selected ARCO 1-2 ONFH with BME on MRI (119, 123). In the current study, BME was present in only 9% of the ARCO 1-2 ONFH and collapse-related bone changes at MDCT were also present in ONFH without BME on MRI. In another study, Stevens et al detected bone fractures at MDCT in 21% of ARCO 1-2 ONFH without collapse at MRI and CR obtained six months after core decompression (118). To date, this is the largest study to have analyzed radiographs, MRI, and MDCT obtained within a short period, to investigate hips that had not been selected according to the presence of BME or been treated by core decompression.

The clinical significance of the CRBC at MDCT in ARCO 1-2 remains unclear. Actually, there was no statistically significant difference in age, sex, pain, functional limitation, size of the necrotic lesion, or the presence of BME at MRI between ARCO 1-2 ONFH with or without collapse-related bone changes at initial MDCT. Previous studies did not assess clinical and MRI findings according to the MDCT findings.

One may hypothesize that the presence of CRBC at MDCT in ARCO 1-2 is associated with early disease progression, but no study addressed this hypothesis. Stevens et al noted that 4 out of 5 ARCO 1-2 ONFH with fracture at MDCT obtained 6 months after core decompression progressed to collapse at MRI and CR 6 months later. In a retrospective study with 2-year follow-up MDCT, Shi et al demonstrated that femoral heads with extensive bone resorption showed more collapse than those with limited bone resorption(124). The prognostic significance of CRBC at MDCT in ARCO 1-2 ONFH remains to be determined by further studies.

Our study has several limitations. First, it is a secondary post hoc monocenter analysis of the initial imaging investigations of individuals who had at least one symptomatic ONFH, willing to be enrolled in a prospective clinical trial; therefore, our population is subject to selection bias. Second, MDCT image analysis was performed by two radiology residents. However, three training sessions were performed before the start of the study. Third, the distinction between trabecular interruption and bone resorption, or between trabecular impaction and peripheral sclerosis could be challenging at MDCT. A threshold value > 1 mm for the width of the lucent zone was used to differentiate bone resorption from trabecular interruption as previously reported (143). We defined trabecular impaction as a faint thin sclerotic line within the necrotic lesion compared to thick peripheral sclerosis. Fourth, bone changes at MDCT were not correlated with any standard of reference. A previous in-vitro study of resected collapsed femoral head specimens demonstrated that μCT enabled to detect accurately cortical and trabecular microfractures in comparison with histology (145, 158). Fifth, ONFH staging has generally a low interobserver reproducibility (103, 106, 108, 139). However, in the current study, we used the recommended 2019 updated version of ARCO with a subsequent good interobserver reproducibility.

In conclusion, at least one CRBC at MDCT occurs in 98-100% of ARCO 3-4 and 26-40% of ARCO 1-2 osteonecrotic femoral heads. Clinical data, lesion size, and frequency of bone marrow edema at baseline MRI in ARCO 1-2 hips with CRBC at MDCT were not significantly different from those without bone changes at MDCT. The association between CRBC at MDCT and collapse at follow-up remains to be determined.

14 Summary of results and future perspectives

The early detection of epiphyseal collapse in ONFH is essential for adequate staging and management in clinical practice by determining the prognosis and the best treatment for the patient. According to the American College of Radiology appropriateness criteria for osteonecrosis, radiographs and MRI are strongly recommended for the assessment of suspected ONFH (110). CT may be appropriate in patients with normal or non-contributive radiographs and is usually appropriate before surgical treatment planning or in patients with contra-indication to MRI (110). The current bench-to-bedside research project contributed to adding more insights into collapse-related bone changes detected on multidetector computed tomography in ONFH.

1) At histology and µCT, 82-86% of cortical microfractures and 91-96% of trabecular microfractures are located in the necrotic lesion.
2) At µCT and histology, trabecular microfractures form elongated clusters and predominate in the superficial layer of the femoral head. At µCT and MDCT, trabecular bone resorption is more profoundly located, in the vicinity of the sclerotic interface.
3) At MDCT of femoral head specimens, cortical interruption, trabecular interruption, and bone resorption predominate in the anterior, superior, and central quadrants of the femoral head, a distribution that parallels the topology of the necrotic lesion.
4) At MDCT of femoral head specimens, cortical interruption, and bone resorption, but not trabecular sclerosis and interruption, are more frequent in femoral heads with more advanced collapse.
5) At MDCT of patients with ARCO 3-4 ONFH, at least one CRBC (cortical interruption, trabecular interruption, trabecular impaction, or bone resorption) is detected in all collapsed ONFH.
6) At MDCT of patients with ARCO 1-2 ONFH, at least one CRBC is detected in 26-40% of non-collapsed ONFH. There is no difference in age, gender, pain, functional impairment, the extent of necrotic lesion, or the presence of BME on MRI between ARCO 1-2 hips with or without CRBC at MDCT.

However, the pathophysiology of collapse remains poorly understood and many research projects deserve further assessment.

1) ***There is a need for a better understanding of collapse-related bone changes at imaging***

It is well established that deformity of the femoral head and subchondral cleft are signs of collapse on MRI and MDCT. Further studies could be performed, using image co-registration to correlate findings on MRI with those at MDCT.

- What is the signal intensity of the subchondral cleft on MRI? Is it always fluid-like?
- What is the corresponding MDCT finding of low T2 lines at MRI? Do they represent trabecular impaction or gas-containing clefts?
- The contribution of MR-derived CT-like images in the detection of cortical and trabecular bone interruption should be further assessed.
- What CRBC at MDCT are associated with BME on MRI?

2) The prognostic significance of collapse-related bone and marrow changes deserves to be addressed by further studies

It is well established that BME surrounding the osteonecrotic lesion may be associated with early progression to collapse. The data in the literature about the prognosis of non-collapsed FH with CRBC on CT is scarce. In the study of Stevens et al (118), 4/5 (80%) of femoral heads with a subchondral fracture on MDCT progressed to collapse on MRI and radiographs at 6 months follow-up. In the study of Shi et al(182), ARCO 2 FH with more resorption had a faster progression to collapse at 2-year CT follow-up. Further studies are needed to address the following issues:

- These preliminary observations on the prognostic value of subchondral fracture and bone resorption should be addressed by larger studies.
- What about trabecular impaction? or FH with a combination of more than one CRBC?
- What is the prognostic significance of marrow and soft tissue changes on MRI without overt collapse, like low T2 lines, BME, or joint effusion?
- Does the size of the fracture or the volume of resorption correlate with a worse outcome? What about the location of CRBC within the FH?

3) The temporal relation between fracture and resorption is yet to be determined

Previous anatomopathological studies and an in vitro µCT study consider bone resorption as a "trigger point" for fracture occurrence and subsequent articular collapse (14, 16, 143). In our study, we demonstrated that the frequency of segments with bone resorption increased with more advanced collapse whereas that of trabecular fracture was not significantly more frequent in more collapsed FH. This finding is not in line with the theory that considers bone resorption as a

precursor of fracture. In addition, in the series of 14 ONFH on which we performed radio-anatomical correlations, one patient had two MDCT examinations prior to his operation, showing trabecular interruption that progressed to an area of bone resorption at 4 months follow up (appendix 3, Figure 30Figure 31). Couldn't it be that trabecular interruption occurring at the interface might also induce bone resorption due to altered bone remodeling? This might challenge the concept of accepting bone resorption in non-collapsed stages of ONFH, namely ARCO 2.

4) Texture analysis and Artificial Intelligence

One might speculate that Artificial Intelligence and texture analysis might have a role to determine different "progression" profiles that include changes on MDCT among other prognostic parameters. An alternative approach would be an ONFH-RADS (Reporting and Data System), based on clinical parameters, size, and location of the lesion, and may include, if sufficient evidence becomes available, CRBC at MDCT.

15 References

1. Ahlback S, Bauer GC, Bohne WH. Spontaneous osteonecrosis of the knee. Arthritis Rheum. 1968;11(6):705-33.
2. Vande Berg BC, Malghem JJ, Lecouvet FE, Jamart J, Maldague BE. Idiopathic bone marrow edema lesions of the femoral head: predictive value of MR imaging findings. Radiology. 1999;212(2):527-35.
3. Blum A, Roch D, Loeuille D, Louis M, Batch T, Lecocq S, et al. [Bone marrow edema: definition, diagnostic value and prognostic value]. J Radiol. 2009;90(12):1789-811.
4. Luttke G, Lehner K, Brandstetter K, Heuck A. Bone marrow edema in MR imaging. United States: Radiological Society of North America Inc; 1989.
5. Lin E, Alessio A. What are the basic concepts of temporal, contrast, and spatial resolution in cardiac CT? J Cardiovasc Comput Tomogr. 2009;3(6):403-8.
6. The classic. An essay on necrosis. Section 1. General remarks, and description of appearances. Clin Orthop Relat Res. 1978(130):5-7.
7. Steinberg ME, Steinberg DR. Osteonecrosis: Historical Perspective. In: Koo K-H, Mont MA, Jones LC, editors. Osteonecrosis. Berlin, Heidelberg: Springer Berlin Heidelberg; 2014. p. 3-15.
8. Phemister DB. Treatment of the necrotic head of the femur in adults. J Bone Joint Surg Am. 1949;31A(1):55-66.
9. Phemister DB. Fractures of the neck of femur, dislocations of hip, and obscure vascular disturbances producing aseptic necrosis of head of femur. Surg Gynecol Obstet. 1934;59:415-40.
10. Ficat RP. Idiopathic bone necrosis of the femoral head. Early diagnosis and treatment. J Bone Joint Surg Br. 1985;67(1):3-9.
11. Ficat RP AJ. Ischemia and necrosis of bone. In: DS H, editor. Baltimore: Williams and Wilkins; 1980.
12. Catto M. Ischaemia of bone. J Clin Pathol Suppl (R Coll Pathol). 1977;11:78-93.
13. Catto M. The histological appearances of late segmental collapse of the femoral head after transcervical fracture. J Bone Joint Surg Br. 1965;47(4):777-91.
14. Kenzora JE, Glimcher MJ. Pathogenesis of idiopathic osteonecrosis: the ubiquitous crescent sign. Orthop Clin North Am. 1985;16(4):681-96.
15. Glimcher MJ, Kenzora JE. Nicolas Andry award. The biology of osteonecrosis of the human femoral head and its clinical implications: 1. Tissue biology. Clin Orthop Relat Res. 1979;138(138):284-309.
16. Glimcher MJ, Kenzora JE. The biology of osteonecrosis of the human femoral head and its clinical implications: II. The pathological changes in the femoral head as an organ and in the hip joint. . Clin Orthop Relat Res. 1979(139):283-312.
17. Glimcher MJ, Kenzora JE. The biology of osteonecrosis of the human femoral head and its clinical implications. III. Discussion of the etiology and genesis of the pathological sequelae; commments on treatment. Clin Orthop Relat Res. 1979(140):273-312.
18. Mitchell DG, Rao VM, Dalinka MK, Spritzer CE, Alavi A, Steinberg ME, et al. Femoral head avascular necrosis: correlation of MR imaging, radiographic staging, radionuclide imaging, and clinical findings. Radiology. 1987;162(3):709-15.
19. Mitchell MD, Kundel HL, Steinberg ME, Kressel HY, Alavi A, Axel L. Avascular necrosis of the hip: comparison of MR, CT, and scintigraphy. AJR Am J Roentgenol. 1986;147(1):67-71.
20. Vande Berg BE, Malghem JJ, Labaisse MA, Noel HM, Maldague BE. MR imaging of avascular necrosis and transient marrow edema of the femoral head. Radiographics. 1993;13(3):501-20.
21. Yamamoto T, Schneider R, Bullough P. Insufficiency subchondral fracture of the femoral head. Am J Surg Pathol. 2000;24(3):464-8.
22. Steinberg ME, Hayken GD, Steinberg DR. A quantitative system for staging avascular necrosis. J Bone Joint Surg Br. 1995;77(1):34-41.
23. Steinberg ME HG, Steinberg DR. . A new method for evaluation and staging of avascular necrosis of the femoral head. In: Arlet J FR, Hungerford DS, eds, editor. Bone circulation. Baltimore: Williams and Wilkins; 1980. p. 398–403.
24. Sugano N, Atsumi T, Ohzono K, Kubo T, Hotokebuchi T, Takaoka K. The 2001 revised criteria for diagnosis, classification, and staging of idiopathic osteonecrosis of the femoral head. J Orthop Sci. 2002;7(5):601-5.
25. Ohzono K, Saito M, Sugano N, Takaoka K, Ono K. The fate of nontraumatic avascular necrosis of the femoral head. A radiologic classification to formulate prognosis. Clin Orthop Relat Res. 1992(277):73-8.

26. Sugano N, Takaoka K, Ohzono K, Matsui M, Masuhara K, Ono K. Prognostication of nontraumatic avascular necrosis of the femoral head. Significance of location and size of the necrotic lesion. Clin Orthop Relat Res. 1994(303):155-64.
27. Morse CG, Mican JM, Jones EC, Joe GO, Rick ME, Formentini E, et al. The incidence and natural history of osteonecrosis in HIV-infected adults. Clin Infect Dis. 2007;44(5):739-48.
28. Ito H, Kaneda K, Matsuno T. Osteonecrosis of the femoral head. Simple varus intertrochanteric osteotomy. J Bone Joint Surg Br. 1999;81(6):969-74.
29. Ando W, Sakai T, Fukushima W, Kaneuji A, Ueshima K, Yamasaki T, et al. Japanese Orthopaedic Association 2019 Guidelines for osteonecrosis of the femoral head. J Orthop Sci. 2021;26(1):46-68.
30. Kang JS, Moon KH, Kwon DG, Shin BK, Woo MS. The natural history of asymptomatic osteonecrosis of the femoral head. Int Orthop. 2013;37(3):379-84.
31. Ikeuchi K, Hasegawa Y, Seki T, Takegami Y, Amano T, Ishiguro N. Epidemiology of nontraumatic osteonecrosis of the femoral head in Japan. Mod Rheumatol. 2015;25(2):278-81.
32. Kang JS, Park S, Song JH, Jung YY, Cho MR, Rhyu KH. Prevalence of osteonecrosis of the femoral head: a nationwide epidemiologic analysis in Korea. J Arthroplasty. 2009;24(8):1178-83.
33. Zhao DW, Yu M, Hu K, Wang W, Yang L, Wang BJ, et al. Prevalence of Nontraumatic Osteonecrosis of the Femoral Head and its Associated Risk Factors in the Chinese Population: Results from a Nationally Representative Survey. Chin Med J (Engl). 2015;128(21):2843-50.
34. Chan VW, Chan PK, Chiu KY, Yan CH, Ng FY. Why do Hong Kong patients need total hip arthroplasty? An analysis of 512 hips from 1998 to 2010. Hong Kong Med J. 2016;22(1):11-5.
35. Lai YS, Wei HW, Cheng CK. Incidence of hip replacement among national health insurance enrollees in Taiwan. J Orthop Surg Res. 2008;3:42.
36. Lubega N, Mkandawire NC, Sibande GC, Norrish AR, Harrison WJ. Joint replacement in Malawi: establishment of a National Joint Registry. J Bone Joint Surg Br. 2009;91(3):341-3.
37. Mankin HJ. Nontraumatic necrosis of bone (osteonecrosis). N Engl J Med. 1992;326(22):1473-9.
38. Koo KH, Lee JS, Lee YJ, Kim KJ, Yoo JJ, Kim HJ. Endothelial nitric oxide synthase gene polymorphisms in patients with nontraumatic femoral head osteonecrosis. J Orthop Res. 2006;24(8):1722-8.
39. Kim T, Hong JM, Lee J, Oh B, Park EK, Lee C, et al. Promoter polymorphisms of the vascular endothelial growth factor gene is associated with an osteonecrosis of the femoral head in the Korean population. Osteoarthritis Cartilage. 2008;16(3):287-91.
40. Chang JD, Hur M, Lee SS, Yoo JH, Lee KM. Genetic background of nontraumatic osteonecrosis of the femoral head in the Korean population. Clin Orthop Relat Res. 2008;466(5):1041-6.
41. He W, Li K. Incidence of genetic polymorphisms involved in lipid metabolism among Chinese patients with osteonecrosis of the femoral head. Acta Orthop. 2009;80(3):325-9.
42. Aaron RK, Voisinet A, Racine J, Ali Y, Feller ER. Corticosteroid-associated avascular necrosis: dose relationships and early diagnosis. Ann N Y Acad Sci. 2011;1240:38-46.
43. Nam KW, Kim YL, Yoo JJ, Koo KH, Yoon KS, Kim HJ. Fate of untreated asymptomatic osteonecrosis of the femoral head. J Bone Joint Surg Am. 2008;90(3):477-84.
44. Cultot A, Norberciak L, Coursier R, Putman S, Cortet B, Paccou J, et al. Bone Perfusion and Adiposity Beyond the Necrotic Zone in Femoral Head Osteonecrosis: A Quantitative Mri Study. Eur J Radiol. 2020;131:109206.
45. Chan WP, Liu YJ, Huang GS, Lin MF, Huang S, Chang YC, et al. Relationship of idiopathic osteonecrosis of the femoral head to perfusion changes in the proximal femur by dynamic contrast-enhanced MRI. AJR Am J Roentgenol. 2011;196(3):637-43.
46. Pascart T, Falgayrac G, Migaud H, Quinchon JF, Norberciak L, Budzik JF, et al. Region specific Raman spectroscopy analysis of the femoral head reveals that trabecular bone is unlikely to contribute to non-traumatic osteonecrosis. Sci Rep. 2017;7(1):97.
47. Wang C, Wang Y, Meng H, Gou W, Yuan X, Xu X, et al. Microstructure and Nanomechanical Properties of Single Trabecular Bone in Different Regions of Osteonecrosis of the Femoral Head. J Nanosci Nanotechnol. 2016;16(3):2264-9.
48. Ehlinger M, Moser T, Adam P, Bierry G, Gangi A, de Mathelin M, et al. Early prediction of femoral head avascular necrosis following neck fracture. Orthop Traumatol Surg Res. 2011;97(1):79-88.
49. Swiontkowski MF, Tepic S, Rahn BA, Cordey J, Perren SM. The effect of fracture on femoral head blood flow. Osteonecrosis and revascularization studied in miniature swine. Acta Orthop Scand. 1993;64(2):196-202.

50. Jones JP, Jr. Fat embolism, intravascular coagulation, and osteonecrosis. Clin Orthop Relat Res. 1993(292):294-308.
51. Jones JP, Jr. Fat embolism and osteonecrosis. Orthop Clin North Am. 1985;16(4):595-633.
52. Holmberg S, Dalen N. Intracapsular pressure and caput circulation in nondisplaced femoral neck fractures. Clin Orthop Relat Res. 1987(219):124-6.
53. Crawfurd EJ, Emery RJ, Hansell DM, Phelan M, Andrews BG. Capsular distension and intracapsular pressure in subcapital fractures of the femur. J Bone Joint Surg Br. 1988;70(2):195-8.
54. Bonnaire FA, Weber AT. The influence of haemarthrosis on the development of femoral head necrosis following intracapsular femoral neck fractures. Injury. 2002;33 Suppl 3:C33-40.
55. Stromqvist B, Wingstrand H, Egund N, Carlin NO, Gustafson T, Herrlin K, et al. Traumatic hip joint tamponade. Two cases with femoral head ischaemia. Acta Orthop Scand. 1985;56(1):81-5.
56. Gash A, Walker CR, Carty H. Case report: complete photopenia of the femoral head on radionuclide bone scanning in septic arthritis of the hip. Br J Radiol. 1994;67(800):816-8.
57. Gutierrez Carbonell P, Ruiz Pinana E, Valiente Valero JM. Intracapsular pressure in children with septic arthritis of the hip. J Pediatr Orthop B. 2021;30(1):80-4.
58. Naito M, Schoenecker PL, Owen JH, Sugioka Y. Acute effect of traction, compression, and hip joint tamponade on blood flow of the femoral head: an experimental model. J Orthop Res. 1992;10(6):800-6.
59. Hungerford DS, Lennox DW. The importance of increased intraosseous pressure in the development of osteonecrosis of the femoral head: implications for treatment. Orthop Clin North Am. 1985;16(4):635-54.
60. Gillet C, Dalla Valle A, Gaspard N, Spruyt D, Vertongen P, Lechanteur J, et al. Osteonecrosis of the Femoral Head: Lipotoxicity Exacerbation in MSC and Modifications of the Bone Marrow Fluid. Endocrinology. 2017;158(3):490-502.
61. Motomura G, Yamamoto T, Miyanishi K, Yamashita A, Sueishi K, Iwamoto Y. Bone marrow fat-cell enlargement in early steroid-induced osteonecrosis--a histomorphometric study of autopsy cases. Pathol Res Pract. 2005;200(11-12):807-11.
62. Vande Berg BC, Gilon R, Malghem J, Lecouvet F, Depresseux G, Houssiau FA. Correlation between baseline femoral neck marrow status and the development of femoral head osteonecrosis in corticosteroid-treated patients: a longitudinal study by MR imaging. Eur J Radiol. 2006;58(3):444-9.
63. Murphey MD, Foreman KL, Klassen-Fischer MK, Fox MG, Chung EM, Kransdorf MJ. From the radiologic pathology archives imaging of osteonecrosis: radiologic-pathologic correlation. Radiographics. 2014;34(4):1003-28.
64. Staudenherz A, Hofmann S, Breitenseher M, Schneider W, Engel AE, Imhof H, et al. Diagnostic patterns for bone marrow oedema syndrome and avascular necrosis of the femoral head in dynamic bone scintigraphy. Nucl Med Commun. 1997;18(12):1178-88.
65. Maillefert JF, Toubeau M, Piroth C, Piroth L, Brunotte F, Tavernier C. Bone scintigraphy equipped with a pinhole collimator for diagnosis of avascular necrosis of the femoral head. Clin Rheumatol. 1997;16(4):372-7.
66. Lee MJ, Corrigan J, Stack JP, Ennis JT. A comparison of modern imaging modalities in osteonecrosis of the femoral head. Clin Radiol. 1990;42(6):427-32.
67. Collier BD, Carrera GF, Johnson RP, Isitman AT, Hellman RS, Knobel J, et al. Detection of femoral head avascular necrosis in adults by SPECT. J Nucl Med. 1985;26(9):979-87.
68. Sugano N, Kubo T, Takaoka K, Ohzono K, Hotokebuchi T, Matsumoto T, et al. Diagnostic criteria for non-traumatic osteonecrosis of the femoral head. A multicentre study. J Bone Joint Surg Br. 1999;81(4):590-5.
69. Chee CG, Cho J, Kang Y, Kim Y, Lee E, Lee JW, et al. Diagnostic accuracy of digital radiography for the diagnosis of osteonecrosis of the femoral head, revisited. Acta Radiol. 2019;60(8):969-76.
70. Beltran J, Burk JM, Herman LJ, Clark RN, Zuelzer WA, Freedy MR, et al. Avascular necrosis of the femoral head: early MRI detection and radiological correlation. Magn Reson Imaging. 1987;5(6):431-42.
71. Bassett LW, Gold RH, Reicher M, Bennett LR, Tooke SM. Magnetic resonance imaging in the early diagnosis of ischemic necrosis of the femoral head. Preliminary results. Clin Orthop Relat Res. 1987(214):237-48.
72. Glickstein MF, Burk DL, Jr., Schiebler ML, Cohen EK, Dalinka MK, Steinberg ME, et al. Avascular necrosis versus other diseases of the hip: sensitivity of MR imaging. Radiology. 1988;169(1):213-5.
73. Robinson HJ, Jr., Hartleben PD, Lund G, Schreiman J. Evaluation of magnetic resonance imaging in the diagnosis of osteonecrosis of the femoral head. Accuracy compared with radiographs, core biopsy, and intraosseous pressure measurements. J Bone Joint Surg Am. 1989;71(5):650-63.
74. Ryu JS, Kim JS, Moon DH, Kim SM, Shin MJ, Chang JS, et al. Bone SPECT is more sensitive than MRI in the detection of early osteonecrosis of the femoral head after renal transplantation. J Nucl Med. 2002;43(8):1006-11.

75. Koo KH, Ahn IO, Kim R, Song HR, Jeong ST, Na JB, et al. Bone marrow edema and associated pain in early stage osteonecrosis of the femoral head: prospective study with serial MR images. Radiology. 1999;213(3):715-22.
76. Fordyce MJ, Solomon L. Early detection of avascular necrosis of the femoral head by MRI. J Bone Joint Surg Br. 1993;75(3):365-7.
77. Thickman D, Axel L, Kressel HY, Steinberg M, Chen H, Velchick M, et al. Magnetic resonance imaging of avascular necrosis of the femoral head. Skeletal Radiol. 1986;15(2):133-40.
78. Beltran J, Herman LJ, Burk JM, Zuelzer WA, Clark RN, Lucas JG, et al. Femoral head avascular necrosis: MR imaging with clinical-pathologic and radionuclide correlation. Radiology. 1988;166(1 Pt 1):215-20.
79. Markisz JA, Knowles RJ, Altchek DW, Schneider R, Whalen JP, Cahill PT. Segmental patterns of avascular necrosis of the femoral heads: early detection with MR imaging. Radiology. 1987;162(3):717-20.
80. Zhang YZ, Cao XY, Li XC, Chen J, Zhao YY, Tian Z, et al. Accuracy of MRI diagnosis of early osteonecrosis of the femoral head: a meta-analysis and systematic review. J Orthop Surg Res. 2018;13(1):167.
81. Dihlmann W. CT analysis of the upper end of the femur: the asterisk sign and ischaemic bone necrosis of the femoral head. Skeletal Radiol. 1982;8(4):251-8.
82. Sarikaya I, Sarikaya A, Holder LE. The role of single photon emission computed tomography in bone imaging. Semin Nucl Med. 2001;31(1):3-16.
83. Magid D, Fishman EK, Scott WW, Jr., Brooker AF, Arnold WP, Lennox DW, et al. Femoral head avascular necrosis: CT assessment with multiplanar reconstruction. Radiology. 1985;157(3):751-6.
84. Stoica Z, Dumitrescu D, Popescu M, Gheonea I, Gabor M, Bogdan N. Imaging of avascular necrosis of femoral head: familiar methods and newer trends. Curr Health Sci J. 2009;35(1):23-8.
85. Lee M, Moon D, Na H. Diagnosis of femoral head avascular necrosis by triple head high resolution. J Nucl Med. 1992;33:936.
86. Lucie RS, Fuller S, Burdick DC, Johnston RM. Early prediction of avascular necrosis of the femoral head following femoral neck fractures. Clin Orthop Relat Res. 1981(161):207-14.
87. Dumont M, Danais S, Taillefer R. "Doughnut" sign in avascular necrosis of the bone. Clin Nucl Med. 1984;9(1):44.
88. Dasa V, Adbel-Nabi H, Anders MJ, Mihalko WM. F-18 fluoride positron emission tomography of the hip for osteonecrosis. Clin Orthop Relat Res. 2008;466(5):1081-6.
89. Min BW, Song KS, Cho CH, Lee SM, Lee KJ. Untreated asymptomatic hips in patients with osteonecrosis of the femoral head. Clin Orthop Relat Res. 2008;466(5):1087-92.
90. Zhao FC, Guo KJ, Li ZR. Osteonecrosis of the femoral head in SARS patients: seven years later. Eur J Orthop Surg Traumatol. 2013;23(6):671-7.
91. Lafforgue P, Dahan E, Chagnaud C, Schiano A, Kasbarian M, Acquaviva PC. Early-stage avascular necrosis of the femoral head: MR imaging for prognosis in 31 cases with at least 2 years of follow-up. Radiology. 1993;187(1):199-204.
92. Mont MA, Zywiel MG, Marker DR, McGrath MS, Delanois RE. The natural history of untreated asymptomatic osteonecrosis of the femoral head: a systematic literature review. J Bone Joint Surg Am. 2010;92(12):2165-70.
93. Kubo Y, Motomura G, Utsunomiya T, Fujii M, Ikemura S, Sonoda K, et al. Distribution of Femoral Head Subchondral Fracture Site Relates to Contact Pressures, Age, and Acetabular Structure. AJR Am J Roentgenol. 2020;215(2):448-57.
94. Kubo Y, Motomura G, Ikemura S, Sonoda K, Hatanaka H, Utsunomiya T, et al. The effect of the anterior boundary of necrotic lesion on the occurrence of collapse in osteonecrosis of the femoral head. Int Orthop. 2018;42(7):1449-55.
95. Utsunomiya T, Motomura G, Ikemura S, Kubo Y, Sonoda K, Hatanaka H, et al. Effects of sclerotic changes on stress concentration in early-stage osteonecrosis: A patient-specific, 3D finite element analysis. J Orthop Res. 2018;36(12):3169-77.
96. Yang JW, Koo KH, Lee MC, Yang P, Noh MD, Kim SY, et al. Mechanics of femoral head osteonecrosis using three-dimensional finite element method. Arch Orthop Trauma Surg. 2002;122(2):88-92.
97. Gao F, Han J, He Z, Li Z. Radiological analysis of cystic lesion in osteonecrosis of the femoral head. Int Orthop. 2018;42(7):1615-21.
98. Karasuyama K, Yamamoto T, Motomura G, Sonoda K, Kubo Y, Iwamoto Y. The role of sclerotic changes in the starting mechanisms of collapse: A histomorphometric and FEM study on the femoral head of osteonecrosis. Bone. 2015;81:644-8.

99. Brown TD, Hild GL. Pre-collapse stress redistributions in femoral head osteonecrosis--a three-dimensional finite element analysis. J Biomech Eng. 1983;105(2):171-6.
100. Brown TD, Mutschler TA, Ferguson AB. A non-linear finite element analysis of some early collapse processes in femoral head osteonecrosis. Journal of Biomechanics. 1982;15(9):705-15.
101. Shimizu K, Moriya H, Akita T, Sakamoto M, Suguro T. Prediction of collapse with magnetic resonance imaging of avascular necrosis of the femoral head. J Bone Joint Surg Am. 1994;76(2):215-23.
102. Takatori Y, Kokubo T, Ninomiya S, Nakamura S, Morimoto S, Kusaba I. Avascular necrosis of the femoral head. Natural history and magnetic resonance imaging. J Bone Joint Surg Br. 1993;75(2):217-21.
103. Takashima K, Sakai T, Hamada H, Takao M, Sugano N. Which Classification System Is Most Useful for Classifying Osteonecrosis of the Femoral Head? Clin Orthop Relat Res. 2018;476(6):1240-9.
104. Nakamura J, Kishida S, Harada Y, Iida S, Oinuma K, Yamamoto S, et al. Inter-observer and intra-observer reliabilities of the Japanese Ministry of Health, Labor and Welfare type classification system for osteonecrosis of the femoral head. Mod Rheumatol. 2011;21(5):488-94.
105. Smith SW, Meyer RA, Connor PM, Smith SE, Hanley EN, Jr. Interobserver reliability and intraobserver reproducibility of the modified Ficat classification system of osteonecrosis of the femoral head. J Bone Joint Surg Am. 1996;78(11):1702-6.
106. Schmitt-Sody M, Kirchhoff C, Mayer W, Goebel M, Jansson V. Avascular necrosis of the femoral head: inter- and intraobserver variations of Ficat and ARCO classifications. Int Orthop. 2008;32(3):283-7.
107. Stove J, Riederle F, Kessler S, Puhl W, Gunther KP. [Reproducibility of radiological classification criteria of femur head necrosis]. Z Orthop Ihre Grenzgeb. 2001;139(2):163-7.
108. Kay RM, Lieberman JR, Dorey FJ, Seeger LL. Inter- and intraobserver variation in staging patients with proven avascular necrosis of the hip. Clin Orthop Relat Res. 1994(307):124-9.
109. Yoon BH, Mont MA, Koo KH, Chen CH, Cheng EY, Cui Q, et al. The 2019 Revised Version of Association Research Circulation Osseous Staging System of Osteonecrosis of the Femoral Head. J Arthroplasty. 2020;35(4):933-40.
110. Murphey MD, Roberts CC, Bencardino JT, Appel M, Arnold E, Chang EY, et al. ACR Appropriateness Criteria Osteonecrosis of the Hip. J Am Coll Radiol. 2016;13(2):147-55.
111. Mont MA, Marulanda GA, Jones LC, Saleh KJ, Gordon N, Hungerford DS, et al. Systematic analysis of classification systems for osteonecrosis of the femoral head. J Bone Joint Surg Am. 2006;88 Suppl 3(Suppl 3):16-26.
112. Zhao D, Zhang F, Wang B, Liu B, Li L, Kim SY, et al. Guidelines for clinical diagnosis and treatment of osteonecrosis of the femoral head in adults (2019 version). J Orthop Translat. 2020;21:100-10.
113. Sultan AA, Mohamed N, Samuel LT, Chughtai M, Sodhi N, Krebs VE, et al. Classification systems of hip osteonecrosis: an updated review. Int Orthop. 2019;43(5):1089-95.
114. Microsurgery Department of the Orthopedics Branch of the Chinese Medical Doctor A, Group from the O, Bone Defect Branch of the Chinese Association of R, Reconstructive S, Microsurgery, Reconstructive Surgery Group of the Orthopedics Branch of the Chinese Medical A. Chinese Guideline for the Diagnosis and Treatment of Osteonecrosis of the Femoral Head in Adults. Orthop Surg. 2017;9(1):3-12.
115. Joint Surgery Group of the Orthopaedic Branch of the Chinese Medical A. Guideline for Diagnostic and Treatment of Osteonecrosis of the Femoral Head. Orthop Surg. 2015;7(3):200-7.
116. Zhao DW, Hu YC. Chinese experts' consensus on the diagnosis and treatment of osteonecrosis of the femoral head in adults. Orthop Surg. 2012;4(3):125-30.
117. Roth A, Beckmann J, Bohndorf K, Heiss C, Jager M, Landgraeber S, et al. [Update of the German S3 guideline on atraumatic femoral head necrosis in adults]. Orthopade. 2018;47(9):757-69.
118. Stevens K, Tao C, Lee SU, Salem N, Vandevenne J, Cheng C, et al. Subchondral fractures in osteonecrosis of the femoral head: comparison of radiography, CT, and MR imaging. AJR Am J Roentgenol. 2003;180(2):363-8.
119. Yeh LR, Chen CK, Huang YL, Pan HB, Yang CF. Diagnostic performance of MR imaging in the assessment of subchondral fractures in avascular necrosis of the femoral head. Skeletal Radiol. 2009;38(6):559-64.
120. Mitchell DG, Kressel HY, Arger PH, Dalinka M, Spritzer CE, Steinberg ME. Avascular necrosis of the femoral head: morphologic assessment by MR imaging, with CT correlation. Radiology. 1986;161(3):739-42.
121. Lang P, Genant HK, Jergesen HE, Murray WR. Imaging of the hip joint. Computed tomography versus magnetic resonance imaging. Clin Orthop Relat Res. 1992(274):135-53.
122. Abumis HM, Uetani M, Yamaguchi T. Bone marrow edema and subchondral fracture in osteonecrosis of the femoral head: analysis with MRI and CT. Acta Medica Nagasakiensia. 2013;58(1):13-8.

123. Meier R, Kraus TM, Schaeffeler C, Torka S, Schlitter AM, Specht K, et al. Bone marrow oedema on MR imaging indicates ARCO stage 3 disease in patients with AVN of the femoral head. Eur Radiol. 2014;24(9):2271-8.
124. Shi S, Luo P, Sun L, Xie L, Yu T, Wang Z, et al. Prediction of the progression of femoral head collapse in ARCO stage 2-3A osteonecrosis based on the initial bone resorption lesion. Br J Radiol. 2021;94(1117):20200981.
125. Stalder AK, Ilgenstein B, Chicherova N, Deyhle H, Beckmann F, Müller B, et al. Combined use of micro computed tomography and histology to evaluate the regenerative capacity of bone grafting materials. International Journal of Materials Research. 2014;105:679 - 91.
126. Klodowski K, Kaminski J, Nowicka K, Tarasiuk J, Wronski S, Swietek M, et al. Micro-imaging of implanted scaffolds using combined MRI and micro-CT. Comput Med Imaging Graph. 2014;38(6):458-68.
127. Bissinger O, Probst FA, Wolff KD, Jeschke A, Weitz J, Deppe H, et al. Comparative 3D micro-CT and 2D histomorphometry analysis of dental implant osseointegration in the maxilla of minipigs. J Clin Periodontol. 2017;44(4):418-27.
128. Feldkamp LA DL, Kress JW. Practical cone-beam algorithm. J Opt Soc Am. 1984;1(6):612-9.
129. Yan G, Tian J, Zhu S, Dai Y, Qin C. Fast cone-beam CT image reconstruction using GPU hardware. J X-ray Sci Technol. 2008;16(4):225-34.
130. Muller R, Van Campenhout H, Van Damme B, Van Der Perre G, Dequeker J, Hildebrand T, et al. Morphometric analysis of human bone biopsies: a quantitative structural comparison of histological sections and micro-computed tomography. Bone. 1998;23(1):59-66.
131. Meyer CR, Moffat BA, Kuszpit KK, Bland PL, McKeever PE, Johnson TD, et al. A methodology for registration of a histological slide and in vivo MRI volume based on optimizing mutual information. Mol Imaging. 2006;5(1):16-23.
132. Groen HC, van Walsum T, Rozie S, Klein S, van Gaalen K, Gijsen FJ, et al. Three-dimensional registration of histology of human atherosclerotic carotid plaques to in-vivo imaging. J Biomech. 2010;43(11):2087-92.
133. Park H, Piert MR, Khan A, Shah R, Hussain H, Siddiqui J, et al. Registration methodology for histological sections and in vivo imaging of human prostate. Acad Radiol. 2008;15(8):1027-39.
134. Jacobs MA, Windham JP, Soltanian-Zadeh H, Peck DJ, Knight RA. Registration and warping of magnetic resonance images to histological sections. Med Phys. 1999;26(8):1568-78.
135. Antill AC, Ballard DH, Hollister AM, Rogers EJ, Yang S, Lokitz SJ. Micro-CT evaluation of rheumatoid arthritis mouse model disease progression: Manual tracings versus semi-automated routines. Diagn Interv Imaging. 2016;97(6):651-5.
136. Gignac PM, Kley NJ. Iodine-enhanced micro-CT imaging: methodological refinements for the study of the soft-tissue anatomy of post-embryonic vertebrates. J Exp Zool B Mol Dev Evol. 2014;322(3):166-76.
137. Gorbachova T, Amber I, Beckmann NM, Bennett DL, Chang EY, Davis L, et al. Nomenclature of Subchondral Nonneoplastic Bone Lesions. AJR Am J Roentgenol. 2019;213(5):963-82.
138. Milgram JW. Injury to articular cartilage joint surfaces: II. Displaced fractures of underlying bone. A histopathologic study of human tissue specimens. Clin Orthop Relat Res. 1986;206(206):236-47.
139. Plakseychuk AY, Shah M, Varitimidis SE, Rubash HE, Sotereanos D. Classification of osteonecrosis of the femoral head. Reliability, reproducibility, and prognostic value. Clin Orthop Relat Res. 2001(386):34-41.
140. Hamada H, Takao M, Sakai T, Sugano N. Subchondral fracture begins from the bone resorption area in osteonecrosis of the femoral head: a micro-computerised tomography study. Int Orthop. 2018;42(7):1479-84.
141. Wang C, Wang X, Xu XL, Yuan XL, Gou WL, Wang AY, et al. Bone microstructure and regional distribution of osteoblast and osteoclast activity in the osteonecrotic femoral head. PLoS One. 2014;9(5):e96361.
142. Wang C, Meng H, Wang Y, Zhao B, Zhao C, Sun W, et al. Analysis of early stage osteonecrosis of the human femoral head and the mechanism of femoral head collapse. Int J Biol Sci. 2018;14(2):156-64.
143. Baba S, Motomura G, Ikemura S, Kubo Y, Utsunomiya T, Hatanaka H, et al. Quantitative evaluation of bone-resorptive lesion volume in osteonecrosis of the femoral head using micro-computed tomography. Joint Bone Spine. 2020;87(1):75-80.
144. Gardeniers J. ARCO Committee on Terminology and Staging. Report on the committee meeting at Santiago de Compostella. ARCO Newsl. 1993;5(5):79-82.
145. Mourad C, Laperre K, Halut M, Galant C, Van Cauter M, Vande Berg BC. Fused micro-computed tomography (muCT) and histological images of bone specimens. Diagn Interv Imaging. 2018;99(7-8):501-5.
146. Fondi C, Franchi A. Definition of bone necrosis by the pathologist. Clin Cases Miner Bone Metab. 2007;4(1):21-6.
147. Ilardi CF, Sokoloff L. Secondary osteonecrosis in osteoarthritis of the femoral head. Hum Pathol. 1984;15(1):79-83.

148. Patterson RJ, Bickel WH, Dahlin DC. Idiopathic Avascular Necrosis of the Head of the Femur. A Study of Fifty-Two Cases. J Bone Joint Surg Am. 1964;46:267-82.
149. Resnick D, Niwayama G, Coutts RD. Subchondral cysts (geodes) in arthritic disorders: pathologic and radiographic appearance of the hip joint. AJR Am J Roentgenol. 1977;128(5):799-806.
150. Wong SY, Kariks J, Evans RA, Dunstan CR, Hills E. The effect of age on bone composition and viability in the femoral head. J Bone Joint Surg Am. 1985;67(2):274-83.
151. Altman D. Practical statistics for medical research. London: Chapman and Hall; 1991.
152. Bullough PG, DiCarlo EF. Subchondral avascular necrosis: a common cause of arthritis. Ann Rheum Dis. 1990;49(6):412-20.
153. Broberg KB. Introduction. In: Broberg KB, editor. Cracks and Fracture. San Diego: Academic Press; 1999. p. 1-4.
154. Maldague B M. Le diagnostic radiologique précoce de la nécrose aseptique post-traumatique de a tête fémorale. J Acta orthop belg. 1984;50:324_42.
155. Sissons HA, Nuovo MA, Steiner GC. Pathology of osteonecrosis of the femoral head. A review of experience at the Hospital for Joint Diseases, New York. Skeletal Radiol. 1992;21(4):229-38.
156. Lakin BA, Patel H, Holland C, Freedman JD, Shelofsky JS, Snyder BD, et al. Contrast-enhanced CT using a cationic contrast agent enables non-destructive assessment of the biochemical and biomechanical properties of mouse tibial plateau cartilage. J Orthop Res. 2016;34(7):1130-8.
157. de Bournonville S, Vangrunderbeeck S, Kerckhofs G. Contrast-Enhanced MicroCT for Virtual 3D Anatomical Pathology of Biological Tissues: A Literature Review. Contrast Media Mol Imaging. 2019;2019:8617406.
158. Mourad C, Galant C, Wacheul E, Kirchgesner T, Michoux N, Vande Berg B. Topology of microfractures in osteonecrotic femoral heads at muCT and histology. Bone. 2020;141:115623.
159. DeLong ER, DeLong DM, Clarke-Pearson DL. Comparing the areas under two or more correlated receiver operating characteristic curves: a nonparametric approach. Biometrics. 1988;44(3):837-45.
160. Lanotte SJ, Larbi A, Michoux N, Baron MP, Hamard A, Mourad C, et al. Value of CT to detect radiographically occult injuries of the proximal femur in elderly patients after low-energy trauma: determination of non-inferiority margins of CT in comparison with MRI. Eur Radiol. 2020;30(2):1113-26.
161. Haj-Mirzaian A, Eng J, Khorasani R, Raja AS, Levin AS, Smith SE, et al. Use of Advanced Imaging for Radiographically Occult Hip Fracture in Elderly Patients: A Systematic Review and Meta-Analysis. Radiology. 2020;296(3):521-31.
162. Mandell JC, Weaver MJ, Khurana B. Computed tomography for occult fractures of the proximal femur, pelvis, and sacrum in clinical practice: single institution, dual-site experience. Emerg Radiol. 2018;25(3):265-73.
163. Pumberger M, Issever AS, Diekhoff T, Schwemmer C, Berg S, Palmowski Y, et al. Bone structure determined by HR-MDCT does not correlate with micro-CT of lumbar vertebral biopsies: a prospective cross-sectional human in vivo study. J Orthop Surg Res. 2020;15(1):398.
164. Bissinger O, Kirschke JS, Probst FA, Stauber M, Wolff KD, Haller B, et al. Micro-CT vs. Whole Body Multirow Detector CT for Analysing Bone Regeneration in an Animal Model. PLoS One. 2016;11(11):e0166540.
165. Chen C, Zhang X, Guo J, Jin D, Letuchy EM, Burns TL, et al. Quantitative imaging of peripheral trabecular bone microarchitecture using MDCT. Med Phys. 2018;45(1):236-49.
166. Issever AS, Link TM, Kentenich M, Rogalla P, Burghardt AJ, Kazakia GJ, et al. Assessment of trabecular bone structure using MDCT: comparison of 64- and 320-slice CT using HR-pQCT as the reference standard. Eur Radiol. 2010;20(2):458-68.
167. Mose K. Methods of measuring in Legg-Calve-Perthes disease with special regard to the prognosis. Clin Orthop Relat Res. 1980(150):103-9.
168. Claffey TJ. Avascular necrosis of the femoral head. An anatomical study. J Bone Joint Surg Br. 1960;42-B:802-9.
169. Anders MH, Laubach SE, Scholz CH. Microfractures: A review. Journal of Structural Geology. 2014;69:377-94.
170. Gersing AS, Pfeiffer D, Kopp FK, Schwaiger BJ, Knebel C, Haller B, et al. Evaluation of MR-derived CT-like images and simulated radiographs compared to conventional radiography in patients with benign and malignant bone tumors. Eur Radiol. 2019;29(1):13-21.
171. Schwaiger BJ, Schneider C, Kronthaler S, Gassert FT, Bohm C, Pfeiffer D, et al. CT-like images based on T1 spoiled gradient-echo and ultra-short echo time MRI sequences for the assessment of vertebral fractures and degenerative bone changes of the spine. Eur Radiol. 2021;31(7):4680-9.

172. Armitage PA, Rivers CS, Karaszewski B, Thomas RG, Lymer GK, Morris Z, et al. A grid overlay framework for analysis of medical images and its application to the measurement of stroke lesions. Eur Radiol. 2012;22(3):625-32.
173. Banerjee S, Kapadia BH, Jauregui JJ, Cherian JJ, Mont MA. Natural History of Osteonecrosis. In: Koo K-H, Mont MA, Jones LC, editors. Osteonecrosis. Berlin, Heidelberg: Springer Berlin Heidelberg; 2014. p. 161-4.
174. Ohzono K, Saito M, Takaoka K, Ono K, Saito S, Nishina T, et al. Natural history of nontraumatic avascular necrosis of the femoral head. J Bone Joint Surg Br. 1991;73(1):68-72.
175. Bellamy N. The WOMAC Knee and Hip Osteoarthritis Indices: development, validation, globalization and influence on the development of the AUSCAN Hand Osteoarthritis Indices. Clin Exp Rheumatol. 2005;23(5 Suppl 39):S148-53.
176. Ha YC, Jung WH, Kim JR, Seong NH, Kim SY, Koo KH. Prediction of collapse in femoral head osteonecrosis: a modified Kerboul method with use of magnetic resonance images. J Bone Joint Surg Am. 2006;88 Suppl 3:35-40.
177. Mont MA, Cherian JJ, Sierra RJ, Jones LC, Lieberman JR. Nontraumatic Osteonecrosis of the Femoral Head: Where Do We Stand Today? A Ten-Year Update. J Bone Joint Surg Am. 2015;97(19):1604-27.
178. Stephenson JW, Davis KW. Imaging of traumatic injuries to the hip. Semin Musculoskelet Radiol. 2013;17(3):306-15.
179. Ross AB, Lee KS, Chang EY, Amini B, Bussell JK, Gorbachova T, et al. ACR Appropriateness Criteria((R)) Acute Hip Pain-Suspected Fracture. J Am Coll Radiol. 2019;16(5S):S18-S25.
180. Kazawa N. T2WI MRI and MRI-MDCT correlations of the osteoporotic vertebral compressive fractures. Eur J Radiol. 2012;81(7):1630-6.
181. Chang MY, Lee SH, Ha JW, Park Y, Zhang HY, Lee SH. Predicting Bone Marrow Edema and Fracture Age in Vertebral Fragility Fractures Using MDCT. AJR Am J Roentgenol. 2020;215(4):970-7.
182. Shiri I, Akhavanallaf A, Sanaat A, Salimi Y, Askari D, Mansouri Z, et al. Ultra-low-dose chest CT imaging of COVID-19 patients using a deep residual neural network. Eur Radiol. 2021;31(3):1420-31.
183. Gardeniers J. ARCO committee on terminology and staging (report from the Nijmegen meeting). ARCO News Letter. 1991(3):153-9.
184. Gardeniers JWM G-GA, Rijnen W. The ARCO staging system: generation and evolution since 1991. . In: Koo KH MM, Jones LC,, editor. Osteonecrosis 2nd ed. Heidelberg: Springer; 2014. p. 215-8.
185. Gardeniers J. A new international classification of osteonecrosis of the ARCO Committee on terminology and classification. J JpnOrthop Assoc 1992;66:18-20.
186. Kerboul M, Thomine J, Postel M, Merle d'Aubigne R. The conservative surgical treatment of idiopathic aseptic necrosis of the femoral head. J Bone Joint Surg Br. 1974;56(2):291-6.
187. Koo KH, Kim R. Quantifying the extent of osteonecrosis of the femoral head. A new method using MRI. J Bone Joint Surg Br. 1995;77(6):875-80.
188. Cherian SF, Laorr A, Saleh KJ, Kuskowski MA, Bailey RF, Cheng EY. Quantifying the extent of femoral head involvement in osteonecrosis. J Bone Joint Surg Am. 2003;85(2):309-15.
189. Chen CH, Chang JK, Lai KA, Hou SM, Chang CH, Wang GJ. Alendronate in the prevention of collapse of the femoral head in nontraumatic osteonecrosis: a two-year multicenter, prospective, randomized, double-blind, placebo-controlled study. Arthritis Rheum. 2012;64(5):1572-8.
190. Lee YK, Ha YC, Cho YJ, Suh KT, Kim SY, Won YY, et al. Does Zoledronate Prevent Femoral Head Collapse from Osteonecrosis? A Prospective, Randomized, Open-Label, Multicenter Study. J Bone Joint Surg Am. 2015;97(14):1142-8.
191. Lieberman JR. Core decompression for osteonecrosis of the hip. Clin Orthop Relat Res. 2004(418):29-33.
192. Mont MA, Salem HS, Piuzzi NS, Goodman SB, Jones LC. Nontraumatic Osteonecrosis of the Femoral Head: Where Do We Stand Today?: A 5-Year Update. J Bone Joint Surg Am. 2020;102(12):1084-99.
193. Hernigou P, Poignard A, Zilber S, Rouard H. Cell therapy of hip osteonecrosis with autologous bone marrow grafting. Indian J Orthop. 2009;43(1):40-5.
194. Gangji V, De Maertelaer V, Hauzeur JP. Autologous bone marrow cell implantation in the treatment of non-traumatic osteonecrosis of the femoral head: Five year follow-up of a prospective controlled study. Bone. 2011;49(5):1005-9.
195. Zhao D, Cui D, Wang B, Tian F, Guo L, Yang L, et al. Treatment of early stage osteonecrosis of the femoral head with autologous implantation of bone marrow-derived and cultured mesenchymal stem cells. Bone. 2012;50(1):325-30.

196. Martin JR, Houdek MT, Sierra RJ. Use of concentrated bone marrow aspirate and platelet rich plasma during minimally invasive decompression of the femoral head in the treatment of osteonecrosis. Croat Med J. 2013;54(3):219-24.
197. Lau RL, Perruccio AV, Evans HM, Mahomed SR, Mahomed NN, Gandhi R. Stem cell therapy for the treatment of early stage avascular necrosis of the femoral head: a systematic review. BMC Musculoskelet Disord. 2014;15:156.
198. Gangji V, Toungouz M, Hauzeur JP. Stem cell therapy for osteonecrosis of the femoral head. Expert Opin Biol Ther. 2005;5(4):437-42.
199. Gangji V, Hauzeur JP, Matos C, De Maertelaer V, Toungouz M, Lambermont M. Treatment of osteonecrosis of the femoral head with implantation of autologous bone-marrow cells. A pilot study. J Bone Joint Surg Am. 2004;86(6):1153-60.
200. Lieberman JR, Conduah A, Urist MR. Treatment of osteonecrosis of the femoral head with core decompression and human bone morphogenetic protein. Clin Orthop Relat Res. 2004;429(429):139-45.
201. Papanagiotou M, Malizos KN, Vlychou M, Dailiana ZH. Autologous (non-vascularised) fibular grafting with recombinant bone morphogenetic protein-7 for the treatment of femoral head osteonecrosis: preliminary report. Bone Joint J. 2014;96-B(1):31-5.
202. Kuroda Y, Asada R, So K, Yonezawa A, Nankaku M, Mukai K, et al. A pilot study of regenerative therapy using controlled release of recombinant human fibroblast growth factor for patients with pre-collapse osteonecrosis of the femoral head. Int Orthop. 2016;40(8):1747-54.

16 Appendix

16.1 Appendix 1: Overview of staging systems of ONFH

Although there is no standard unified classification system used by all investigators, the presence of fracture is considered to represent stage III, whatever the classification system. Except for JIC (103, 104), intra-observer reproducibility of these staging systems has been assessed in a limited number of patients and it has been shown to be moderate to fair (105-108).

The importance of an effective and uniformly used classification system has been recognized since the early 90s. In 1991, the Association Research Circulation Osseous (ARCO) developed the first international classification. The original version was composed of 7 stages of disease progression with a subdivision of location and size of the necrotic lesion(183). ARCO tried to simplify the original classification in 1994 to include 5 stages (144). However, this modified version has not been widely used (103, 108, 113). The Nijmegen modification divided stage 3 into early and late substages to improve on the prognostic impact of stage 3 in the 1994 ARCO system (184).

The following tables summarize the commonly used staging systems:

- Ficat and Arlet
- The University of Pennsylvania, also known as Steinberg classification
- The Association Research Circulation Osseous (ARCO) classification and its modifications
- The Japanese Investigation Committee (JIC)

Table E1: Classification system of Ficat and Arlet (10, 113)

Stage	Radiographic signs	Clinical features
0	Inconspicuous/normal findings	0 (silent hip)
I	Inconspicuous findings or minor changes (slight patchy osteoporosis, blurring of trabecular pattern, subtle loss of clarity) *	+
II A	Curvilinear sclerosis is seen around the necrotic portion Diffuse/ focal radiological changes (osteoporosis, sclerosis, cysts)	+
II B (transition)	Subchondral fracture (crescent sign) segmental flattening of the femoral head (out-of-round appearance)	+
III	Broken contour of femoral head, bone sequestrum, joint space normal	++
IV	Flattened contour of the femoral head, decreased joint space collapse of the femoral head, acetabular osteoarthritic changes	+++

* *an increased uptake of tracer on bone scintigraphy or increased bone marrow signal with edema on MRI may exist*

This is the most popular staging system: it is simple, easy to use, correlates staging on CR to the clinical findings. However, it does not incorporate MRI findings, does not quantify the lesion size, assess its location, and does not quantify collapse. Therefore, it has low accuracy in the assessment of disease progression. It has also a low interobserver reproducibility. With the advent of MRI, stage 0 is considered nowadays to be obsolete.

Table E2: University of Pennsylvania (Steinberg) classification (22, 113)

Stage	Criteria
0	Normal radiograph, bone scan, and magnetic resonance images
I	Normal radiograph. Abnormal bone scan and/or magnetic resonance images A: Mild (< 15% of femoral head affected) B: Moderate (15 to 30% of femoral head affected) C: Severe (> 30% of femoral head affected)
II	Cystic and sclerotic changes in femoral head on radiographs A: Mild (< 15% of femoral head affected) B: Moderate (15 to 30% of femoral head affected) C: Severe (> 30% of femoral head affected)
III	Subchondral collapse without flattening (crescent sign) A: Mild (< 15% of articular surface) B: Moderate (15 to 30% of articular surface) C: Severe (> 30% of articular surface)
IV	Flattening of femoral head A: Mild (< 15% of surface and < 2 mm of depression) B: Moderate (15 to 30% of surface and 2 to 4 mm of depression) C: Severe (> 30% of surface and > 4 mm of depression)
V	Joint narrowing or acetabular changes A: Mild / B: Moderate / C: Severe
VI	Advanced degenerative changes

This is the first staging system to include MRI and incorporate size of the lesion and joint involvement. Stages parallel the natural history of ONFH; therefore, it can trace the progression of the disease. It also includes the quantification of fracture and collapse. However, it includes too many stages, some are not relevant for treatment (4 to 6) which contributes to moderate interobserver reliability. It also lacks a detailed description of quantification and does not include clinical signs and symptoms.

Table E3: The Association Research Circulation Osseous (ARCO) classification (144, 185)

Stage	Findings	Techniques	Sub classification	Quantification
0	none	CR, CT, MRI, scintigraphy	No	No
1	CR and CT normal. MRI or scintigraphy positive	MRI, scintigraphy	Location of the lesion: Medial Central Lateral	Area of involvement A: Minimal (< 15%) B: Moderate (15 to 30%) C: Extensive
2	Sclerosis, osteolysis, focal osteoporosis	CR, CT, MRI, scintigraphy		
Early 3	Crescent sign No flattening	CR, CT		Length of crescent A: < 15% B: 15 to 30% C: > 30%
Late 3	Flattening of the articular surface			Surface collapse and dome depression A: < 15% and < 2 mm B: 15 to 30% and 2 to 4 mm C: > 30% and > 4 mm
4	Osteoarthritis, acetabular changes, joint destruction	CR	No	No

This staging system incorporates CR, MRI, CT, and scintigraphy. It includes a quantitative evaluation of lesion size, length of the crescent, and degree of collapse which parallels the natural progression of the disease. However, it lacks a detailed description of quantification. The interobserver reliability is insufficient. There are multiple updated versions with no unanimous consensus.

Table E4: The Japanese Investigation committee (JIC) diagnostic criteria of osteonecrosis(24, 68)

Technique	Diagnostic Criteria
CR	-Collapse of the femoral head without joint-space narrowing or acetabular abnormality on CRs (including crescent sign) - Demarcating sclerosis in the femoral head without joint-space narrowing or acetabular abnormality
Bone scan (Scintigraphy)	"Cold in hot" on bone scans
MRI	Low-intensity band on T1-weighted images (band-like pattern)
Core biopsy	Trabecular and marrow necrosis on histology

* *The Sensitivity is 91% and Specificity is 99% for the diagnosis of osteonecrosis based on any two positive criteria out of the five criteria.*

Table E5: The JIC (Japanese Investigation Committee) classification (24, 26)

Type	Description	Subclassification		Prognosis
1	demarcating sclerosis	A	Lesions occupy the medial one-third or less of the weight-bearing portion	<10% collapse
		B	Lesions occupy the medial two-thirds or less of the weight-bearing portion	40% collapse
		C1	Lesions occupy more than the medial two-thirds of the weight-bearing portion and do not extend laterally	80% collapse
		C2	Lesions occupy more than the medial two-thirds of the weight-bearing portion and extend laterally to the acetabular edge	>90% collapse
2	flattening			100% collapse
3	cystic radiolucency	A	cystic lesion is located far from the weight-bearing Surface	0% collapse
		B	cystic lesion is located at the weight-bearing surface	100% collapse

This is the only classification that assesses the location of the lesion relative to the acetabular weight-bearing region. It has a prognostic value and correlates to the outcome of osteotomies. It has a high degree of interobserver reliability. However, it does not specifically evaluate stages I or IV and does not evaluate femoral head collapse.

Table E6: Common methods to quantify femoral head osteonecrosis

Method	Description
Kerboul(186)	Combined necrotic angle: measure the arc of the articular surface overlying the lesion on AP and lateral radiographs
Koo and Kim(187)	Index of necrotic extent: angular measures made on midcoronal and midsagittal MRI images. (A/180) x (B/180) x 100. Classified into small, medium, large lesions.
Cherian(188)	Modified index of necrotic extent uses images showing maximum lesion size on coronal and sagittal
Ha(176)	Modified Kerboul: sum of arcs measured on midcoronal, and midsagittal sections added together. 4 separate grades.
Nam(43)	Percent area (extent) of a necrotic lesion on sagittal and coronal MR images. % extent = (A x B / R x R') x 100 R = the largest mediolateral diameter of the femoral head R' = the largest anteroposterior diameter of the femoral head A = the longest mediolateral length of the necrotic lesion B = the longest anteroposterior length of the necrotic lesion.

16.2 Appendix 2: Synopsis of treatment options

16.2.1 Conservative Treatment

Pain relief can be obtained in the short term by resting and the use of crutches to unload the femoral head. However, there is no evidence that resting and unloading could prevent the progression of collapse of the femoral head or could suppress the need for surgical treatment in the long term (29). Other therapeutic methods can be applied, including extracorporeal shock waves, electromagnetic field stimulation, and hyperbaric oxygen therapy, which have been shown to alleviate pain related to ONFH but there is no clear evidence that these therapies could prevent progression (29). The administration of bisphosphonates could reduce pain in the short term, but it does not prevent femoral head collapse in the long term (29, 189, 190). Despite the use of a large spectrum of drugs or conservative methods, there is no evidence-based medicine that medical management of symptomatic ONFH is effective in preventing or arresting the disease process (99).

Treatment efficacy of ONFH remains controversial for many reasons: the lack of generally accepted diagnostic gold standard (intraosseous pressure determination, histology, MRI), the difficulties in lesion classification, and the limited knowledge on the natural history of osteonecrosis.

16.2.2 Surgical Treatment

Several surgical procedures have been tried with variable success (29, 112, 114-116, 177, 191). Core decompression of the hip with or without bone graft is the most common procedure currently used to treat the early stages of FHON (29, 112, 192). It appears to be efficient in pain control. However, there is no consensus among investigators regarding either the indication for this procedure or its effect on the fate of the femoral head (99-102). Bone marrow-derived mononuclear and mesenchymal cells are also used in addition to core decompression, in early-stage FHON (193-199). Growth factors have been proposed, but their effectiveness is yet to be determined (200-202)

In the late stages of osteonecrosis that include femoral head deformity and secondary osteoarthritis, total hip arthroplasty is the most appropriate treatment, although several hip-sparing procedures have been tried with variable success. Non-vascularized bone grafting may be performed in addition to core decompression. It involves removal of necrotic bone, and the impaction of bone grafting (autologous bone, allogenic bone, or bone substitution) to provide

structural support and scaffolding, and to allow repair and remodeling of subchondral bone. The rationale for vascularized bone grafting is that it aims to restore a vascular supply for the femoral head. There have been multiple published reports on the use of vascularized bone grafts and their results vary among reports. Good clinical outcomes can be expected in cases when arthritic changes have not appeared (29).

The rationale for osteotomies is to move the segment of necrotic bone away from the weight-bearing region, thereby relieving stress. There are two types of osteotomies: angular intertrochanteric (varus and valgus) and rotational transtrochanteric. Femoral varus osteotomy is useful to relieve symptoms and prevent the progression of ONFH with sufficient intact area at the lateral femoral head whereas transtrochanteric rotational osteotomy is useful in ONFH with a wide necrotic area (29). However, these highly specific procedures need high accuracy in patient selection, preoperative planning, surgical technique, and appropriate post-treatment management. Therefore, the results are variable, with more successful outcomes being in highly specialized centers with more experienced operators. An important note is that total hip replacement performed after an osteotomy are often technically more difficult than those done in patients with ONFH who have never had an osteotomy.

16.3 Appendix 3: Correlation between in vitro and in vivo imaging: preliminary observations

Among the 13 patients from whom resected femoral head specimens were obtained, two patients had MDCT examinations performed prior to the operation. In this section, we will illustrate collapse-related bone changes on clinical MDCT, correlated with MRI, with corresponding in vitro MDCT of the FH specimen.

16.3.1 Low T2 line at MRI corresponding to trabecular impaction at MDCT

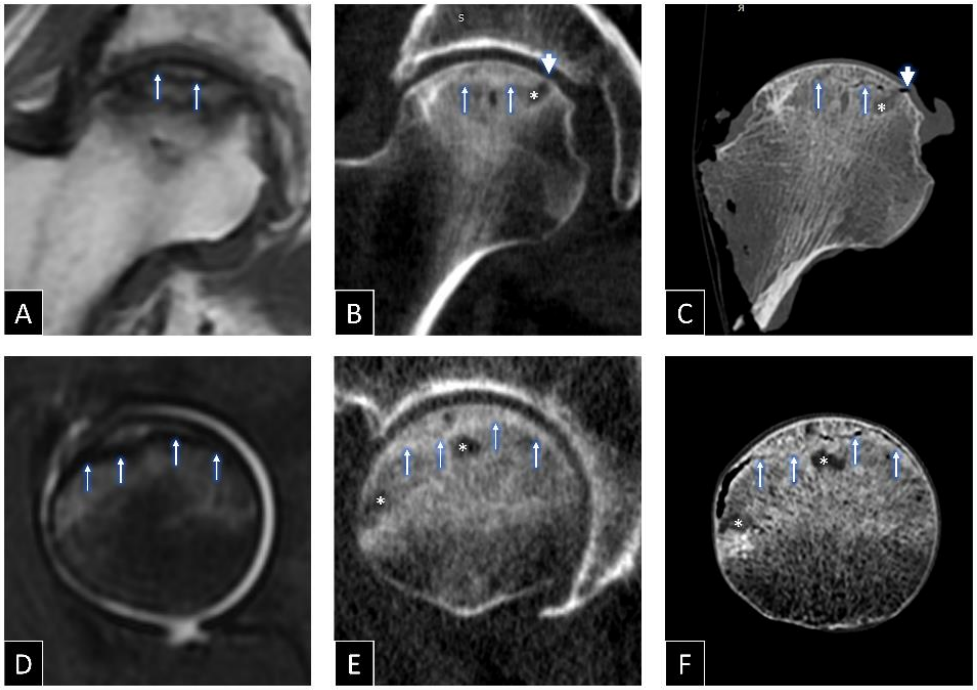

Figure 29: 54 yo man with steroid related ONFH. MRI and MDCT were performed 1 day prior to total hip replacement (A) Coronal T1-weighted MR image and (D) sagittal PD-Fat sat image show a subchondral low signal intensity line (arrows) within the osteonecrotic lesion . (B) Coronal and (E) sagittal MDCT reformats show cortical interruption (arrowheads in B), trabecular impaction (arrows) and bone resorption (asterisks). Corresponding (C) coronal and (F) sagittal MDCT reformats of the resected femoral head specimen show cortical interruption (arrowhead in C), trabecular interruption (arrows) and bone resorption (asterisks).

16.3.2 Temporal evolution of collapse-related bone changes at MDCT

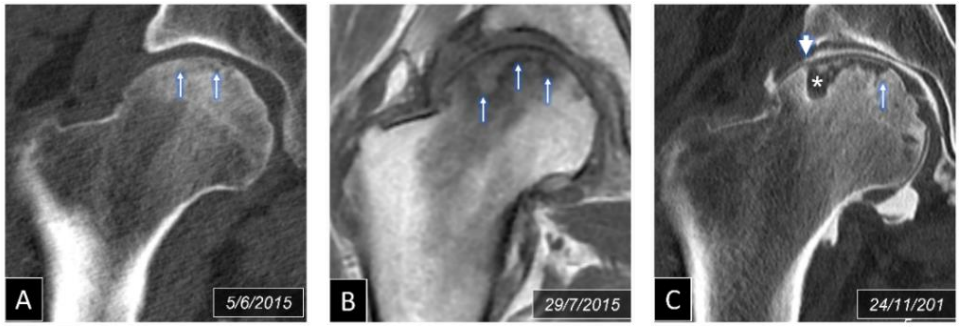

Figure 30: ONFH in a 37 yo man with renal transplant. (A) Coronal MDCT reformat shows trabecular interruption (arrows); also note the heterogeneous density of the femoral head. (B) Coronal T1-weighted MR image shows the osteonecrotic lesion (arrows) without collapse of the articular surface. (C) Coronal reformat of CT arthrogram (5 months later) shows progression of collapse-related bone changes: cortical interruption (arrowhead), trabecular interruption (arrow) and bone resorption (asterisk).

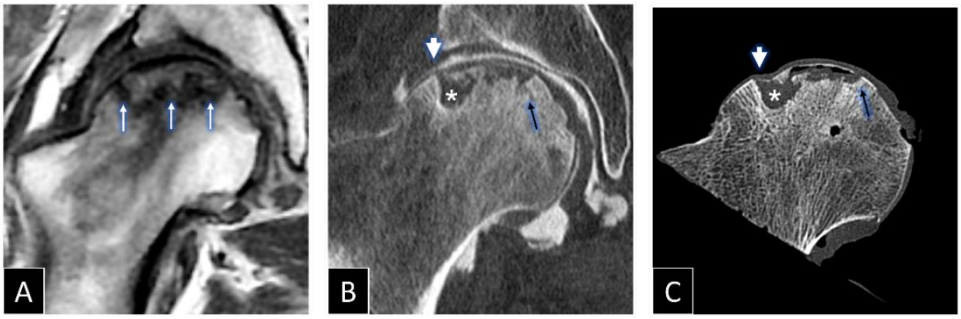

Figure 31: Same patient as figure 31. (A) Coronal T1-weighted MRI shows osteonecrotic lesion (arrows) without collapse of the articular surface. (B) Coronal reformat of a CT arthrogram 4 months later and (C) corresponding coronal MDCT reformat of the resected femoral head specimen (7 months after the MRI) show cortical interruption (arrowheads), trabecular interruption (arrows) and bone resorption (asterisks).